

¹ **MicroBooNE: The Search For The MiniBooNE**
² **Low Energy Excess**

³ **David Kaleko**

⁴ Submitted in partial fulfillment of the
⁵ requirements for the degree
⁶ of Doctor of Philosophy
⁷ in the Graduate School of Arts and Sciences

⁸ **COLUMBIA UNIVERSITY**

⁹ **2017**

10

11

©2017

12

David Kaleko

13

All Rights Reserved

¹⁴ Table of Contents

¹⁵	1	Introduction	1
¹⁶	2	Neutrinos, Neutrino Oscillations, and Sterile Neutrinos	3
¹⁷	2.1	Introduction to Neutrinos	3
¹⁸	2.2	Neutrino Oscillations	4
¹⁹	2.3	Sterile Neutrinos	8
²⁰	3	The MicroBooNE Detector	11
²¹	3.1	Introduction	11
²²	3.2	Time Projection Chamber	13
²³	3.3	Light Collection System	13
²⁴	3.4	Electronics, Readout, and Triggering	15
²⁵	4	The Booster Neutrino Beam	21
²⁶	4.1	The Booster Neutrino Beam	21
²⁷	4.1.1	Primary Proton Beam	21
²⁸	4.1.2	Proton Target and Focusing Horn	23
²⁹	4.2	Monte Carlo Neutrino Flux Prediction	25
³⁰	5	Low Energy Excess: LSND and MiniBooNE	29
³¹	5.1	Introduction	29
³²	5.2	LSND Observation	29
³³	5.3	The MiniBooNE Experiment	30
³⁴	5.3.1	The MiniBooNE Detector and Monte Carlo Simulation	30

35	5.3.2 MiniBooNE Event Selection	31
36	5.3.3 MiniBooNE Results	34
37	5.3.4 Proposed Low Energy Excess Sources	36
38	5.4 Conclusions	38
39	6 Low Energy Excess: MicroBooNE	41
40	6.1 MicroBooNE In The Context of the Low Energy Excess	41
41	6.1.1 Past Sensitivity Studies	42
42	6.2 Monte Carlo Simulation	46
43	6.2.1 Simulated Background Samples	46
44	6.2.2 Reconstruction	46
45	6.3 Event Selection	48
46	6.3.1 Electron/Photon Separation Algorithm	49
47	6.3.2 Signal Selection Algorithm	54
48	6.3.3 Energy Reconstruction	59
49	6.4 Backgrounds	60
50	6.4.1 Background Topologies	60
51	6.4.2 Background Normalization	66
52	6.4.3 Analysis Cuts and Results	67
53	6.5 MiniBooNE Low Energy Excess Signal Modeling In MicroBooNE	69
54	6.5.1 Sensitivity Results	73
55	7 Studies of Kaons Produced at the Proton Target	79
56	7.1 BNB Kaon Production Introduction and Motivation	79
57	7.2 Event Selection	83
58	7.2.1 Track Reconstruction	85
59	7.2.2 Selection Criteria	87
60	7.2.3 Backgrounds	89
61	7.3 Neutrino Energy Reconstruction	90
62	7.4 Results in Simulation	94
63	7.5 Sideband Data and Simulation Comparisons	96

64	7.6 Conclusions	108
65	8 Multiple Coulomb Scattering	111
66	8.1 Introduction and motivation	111
67	8.2 Multiple Coulomb scattering	114
68	8.2.1 Tuning the Highland formula for argon	115
69	8.3 MCS implementation using the maximum likelihood method	117
70	8.3.1 Track segmentation and scattering angle computation	119
71	8.3.2 Maximum likelihood theory	119
72	8.3.3 Maximum likelihood implementation	120
73	8.4 Range-based energy validation from simulation	121
74	8.5 MCS performance on beam neutrino-induced muons in MicroBooNE data .	121
75	8.5.1 Input sample	121
76	8.5.2 Event selection	123
77	8.5.3 Validation of the Highland formula	124
78	8.5.4 MCS momentum validation	124
79	8.5.5 Impact of Highland formula tuning	126
80	8.6 MCS performance on exiting muons in MicroBooNE simulation	128
81	8.7 Conclusions	130
82	8.8 Acknowledgments	133
83	Bibliography	133

⁸⁴ List of Figures

85	2.1	<i>The neutrino mass hierarchy possibilities. The flavor eigenstate fraction for each mass eigenstate is shown by the relative amount of gray, red, or blue in each bar.</i>	5
88	2.2	<i>Results from the KamLAND collaboration measuring the survival probability of $\bar{\nu}_e$ from nuclear reactors. A clear oscillation as a function of L/E as predicted by the two-neutrino model is shown.</i>	7
91	2.3	<i>Mass hierarchy with one heavy sterile neutrino included. The δm^2 from LSND is incorporated.</i>	9
93	3.1	<i>A cartoon schematic of how a LArTPC works. Ionization electrons from particles traversing the detector medium are drifted by an electric field, E_{drift} past multiple planes of sense wires. The signals on those wires create several two-dimensional images of the event, which are combined to create a three-dimensional reconstruction of the event. Note that in a LArTPC, PMTs are used to collect scintillation light, but are not drawn in this diagram.</i>	12
99	3.2	<i>A 3D rendering of the MicroBooNE detector. The rectangular time projection chamber (TPC) fits within the cylindrical cryostat. The feedthroughs along the top allow for the PMT and sense wire signals to be read out to the DAQ. Not shown are the photomultiplier tubes (PMTS) located on the wall behind the sense wire planes.</i>	14
104	3.3	<i>A side-on view of the MicroBooNE detector showing the location of the 32 PMTs (labeled “optical units”) and the four light guide paddles.</i>	16

106	3.4 A picture of one of the 8 inch Hamamatsu R5912-02mod cryogenic photo-	
107	multiplier tubes (PMT) used in the MicroBooNE detector. Note the clear	
108	acrylic plate, which is coated with a wavelength-shifting organic fluor (TPB)	
109	before installation to convert the VUV liquid argon scintillation light into the	
110	visible spectrum, detectable by the PMT.	17
111	3.5 The MicroBooNE readout schematic. On the left are portions of the read-	
112	out operating at argon temperatures. Signals pass through feedthroughs into	
113	warm electronics readout boards, unique for the TPC (sense wire signals)	
114	and the light collection system (PMT signals). These signals are combined	
115	with external timing signals from the accelerator to form triggers that initiate	
116	readout of all systems.	18
117	4.1 Overall layout of the BNB. The primary proton beam, extracted from the	
118	Booster, enters the target hall from the left. Upon exiting the target hall,	
119	particles encounter a 50-meter-long decay region, terminating in the beam	
120	stop on the right.	22
121	4.2 The BNB focusing horn system. The gray outer conductor is drawn trans-	
122	parent for visualization purposes. The beryllium target lies within the central	
123	hollow tube axis. A current flows along the inner conductor, returning along	
124	the outer conductor.	24
125	4.3 A cartoon diagram of the incident 8.89 GeV/c proton beam (from the left)	
126	colliding with the beryllium target within the focusing horn. Shown is the	
127	current configuration for the horn referred to as “neutrino mode” in which	
128	positive charged secondaries are focused into the decay region. The 25 m	
129	absorber drawn is removable, and was not used for the analyses described in	
130	this thesis.	24
131	4.4 Neutrino flux prediction (black dots) with systematic error bars (red envelope)	
132	excluding proton delivery systematics which results in a flat normalization	
133	correction.	28

134	5.1	<i>The MiniBooNE detector enclosure (left) and a cut-away drawing (right) of the detector showing the distribution of PMT's in the signal and veto regions.</i>	31
135			
136	5.2	<i>A schematic of the pattern Cherenkov light from different particles would make projected onto the inner walls of the MiniBooNE detector. Top is a muon track (a filled-in ring), middle is an electron (a fuzzy ring), bottom is a photon that pair-produces and creates two fuzzy rings.</i>	32
137			
138			
139	5.3	<i>Feynman diagrams of the charged-current quasi-elastic (CCQE) interaction channel for ν_e, ν_μ, $\bar{\nu}_\mu$, and $\bar{\nu}_e$ (clockwise from the top left). ν_e CCQE is the signal channel for the MiniBooNE oscillation analysis.</i>	33
140			
141	5.4	<i>The E_ν^{QE} distribution for MiniBooNE data (points with statistical errors) and backgrounds (histogram with systematic errors).</i>	35
142			
143	5.5	<i>The MiniBooNE event excess as a function of E_ν^{QE}. Also shown are the expectations from the best oscillation fit and from neutrino oscillation parameters in the LSND allowed region. The error bars include both statistical and systematic errors.</i>	36
144			
145			
146			
147			
148	6.1	<i>Energy loss per unit length along the first 2.4 cm of simulated single electron showers (red) and single photon showers (black) in terms of minimally ionizing particle (MIP) energy in liquid argon (about 2.1 MeV/cm). Photons in general have twice the dE/dx of electrons at the start of their showers, stemming from pair production.</i>	44
149			
150			
151			
152			
153			
154	6.2	<i>The results of the first analysis to scale the MiniBooNE backgrounds and excess to MicroBooNE both under the assumption that the excess is due to an electron-like event (left) or under a photon-like event (right). Stacked histograms show the expected background. Error bars indicate statistical uncertainty. The number of signal events, scaled from MiniBooNE for neutrino flux and fiducial volume, is the same in both plots (though dedicate electron-specific and photon-specific event selection cuts may show this to be unrealistic). Both plots assume 6.6×10^{20} POT for the MicroBooNE 60 ton fiducial mass.</i>	45
155			
156			
157			
158			
159			
160			
161			
162			

163	6.3 <i>AlgoEMPart training results on perfect reconstructed electron showers and</i>	
164	<i>on perfect reconstructed photon showers as described in Section 6.3.1.1: 1D</i>	
165	<i>landau + Gaussian fit to dE/dx. “Frac” in the legend is the relative nor-</i>	
166	<i>malization between the landau and Gaussian fits; that “Frac” is close to one</i>	
167	<i>means the landau fit dominates.</i>	51
168	6.4 <i>AlgoEMPart: Computed 1D likelihood vs dE/dx: red is photon, blue is elec-</i>	
169	<i>tron. How the likelihood is computed is described in Section 6.3.1.1.</i>	53
170	6.5 <i>AlgoEMPart training results on perfect reconstructed electron and photon</i>	
171	<i>showers as described in Section 6.3.1.1 integrated over all energies: 2D like-</i>	
172	<i>lihood distribution (radiation length vs. dE/dx). Low values of likelihood</i>	
173	<i>(purple) correspond to photon-like, high values (red) correspond to electron-</i>	
174	<i>like.</i>	53
175	6.6 <i>AlgoEMPart training results on perfect reconstructed electron showers as de-</i>	
176	<i>scribed in Section 6.3.1.1: Radiation length fit to single electron showers.</i>	
177	<i>Note the poor quality of the fit as the electron conversion distance for “per-</i>	
178	<i>fect reconstruction” does not follow an exponential distribution; all conversion</i>	
179	<i>distances are below 0.3 centimeters.</i>	54
180	6.7 <i>AlgoEMPart training results on perfect reconstructed photon showers as de-</i>	
181	<i>scribed in Section 6.3.1.1: Radiation length fit to single photon showers. .</i>	55
182	6.8 <i>AlgoEMPart: Computed 1D likelihood vs conversion distance (integrated over</i>	
183	<i>all energies): red is photon, blue is electron. How the likelihood is computed</i>	
184	<i>is described in Section 6.3.1.1.</i>	55
185	6.9 <i>A flowchart depicting decisions the algorithm makes for each primary, non-</i>	
186	<i>cosmic shower. If the algorithm gets to the bottom of the flowchart, that</i>	
187	<i>shower was determined to be from a ν_e^{CC} interaction, and a ν_e particle is</i>	
188	<i>created. For clarification of what some acronyms mean, see Figure 6.10. .</i>	56
189	6.10 <i>Schematic cartoons indicating how the signal selection algorithm makes de-</i>	
190	<i>cisions determining if two reconstructed showers are correlated, and if a re-</i>	
191	<i>constructed shower is correlated with a reconstructed track (as described in</i>	
192	<i>Figure 6.9).</i>	57

193	6.11 Reconstructed neutrino energy as described in Section 6.3.3 versus true neutrino energy. This plot was made from “perfect reconstruction” objects in correctly identified ν_e^{CCQE} events after all final analysis cuts were placed.	61
196	6.12 A neutrino energy resolution and bias plot. This is created by binning Figure 6.11 in true neutrino energy and making a distribution of (Reco Energy - True Energy)/(True Energy). For each bin, the mean (red) and standard deviation (blue) are plotted in the above figure. This plot was made from “perfect reconstruction” objects in correctly identified ν_e^{CCQE} events after all final analysis cuts were placed.	62
202	6.13 A 3D event display showing measured cosmic tracks entering the MicroBooNE detector. The three boxes show the full readout window of the detector which corresponds to 4.8 ms. The red highlighted box shows the physical volume of the TPC. The colored lines are 3D reconstructed cosmic tracks. Data taken in August, 2015.	65
207	6.14 The measured distribution of flash times (requiring flashes greater than 50PE) with respect to the trigger time for BNB-triggered events, shown as a ratio to the expected cosmic rate from off-beam data. The blue band denoting the cosmic rate was centered at one, with a width corresponding to the measured uncertainty in the cosmic rate. A clear excess can be seen due to neutrinos between 3 and 5 μ s after the trigger. This is where the neutrinos were expected based on the RWM signal arrival time. A total of 1.92E6 BNB triggered events (unbiased trigger) were used to produce this plot.	67
215	6.15 The backgrounds to the ν_e^{CCQE} appearance search in MicroBooNE with statistical-only error bars shown. The event selection is described in Section 6.3, the background topologies described in Section 6.4.1, the relative normalization between samples described in Section 6.4.2, and the energy reconstruction described in Section 6.3.3.	70
220	6.16 The computed distribution of u_z (how forward-going the event is) vs. E_{vis} for $N = 1000$ times the MiniBooNE low energy excess (raw) events.	72

222	6.17 The backgrounds to the ν_e^{CCQE} appearance search in MicroBooNE with scaled signal drawn. The event selection is described in Section 6.3, the background topologies described in Section 6.4.1, the relative normalization between samples described in Section 6.4.2, and the energy reconstruction described in Section 6.3.3. The scaled signal is described in Section 6.5.	73
227	6.18 The backgrounds to the ν_e^{CCQE} appearance search in MicroBooNE with scaled signal drawn. The event selection is described in Section 6.3, the background topologies described in Section 6.4.1, the relative normalization between samples described in Section 6.4.2, and the energy reconstruction described in Section 6.3.3. The scaled signal is described in Section 6.5. Here the shower reconstruction efficiency has been decreased from the “perfect reconstruction” value of 100% to 85% to emulate possible realistic shower reconstruction efficiencies.	77
235	7.1 The breakdown of ν_e^{CC} interactions in MicroBooNE from the booster neutrino beam-line by ν_e parentage. ν_e from K^+ decay is the primary contributor to the intrinsic ν_e interaction rate at higher neutrino energies.	80
238	7.2 The Booster Neutrino Beam (BNB) flux at MicroBooNE.	81
239	7.3 The beam ν_μ parentage as a function of true neutrino energy.	82
240	7.4 The fractional error for the BNB ν_μ flux through MicroBooNE, broken up by systematic source. “Other” includes hadronic interactions, horn current uncertainty, skin depth effects, etc. The production uncertainties are divided by neutrino parent. Note the largest uncertainty at higher ν_μ energies still comes from K^+ production, even including the SciBooNE measurement. . .	83
245	7.5 The fractional error for the BNB ν_e flux through MicroBooNE, broken up by systematic source. “Other” includes hadronic interactions, horn current uncertainty, skin depth effects, etc. The production uncertainties are divided by neutrino parent. Note the largest uncertainty for ν_e above about 0.5 GeV neutrino energy still comes from K^+ production, even including the SciBooNE measurement.	84

251	7.6 Muon neutrino charged-current cross section measurements and predictions as a function of neutrino energy. QE stands for quasielastic channels, RES stands for resonant channels, and DIS stands for deep inelastic scattering channels.	85
255	7.7 The fraction of ν_μ energy imparted to the outgoing lepton (μ) in ν_μ^{CC} inter- actions.	91
257	7.8 Reconstructed neutrino energy versus true neutrino energy for a sample of correctly identified BNB ν_μ^{CC} interactions in the MicroBooNE TPC.	93
259	7.9 Distribution of signal (green) and backgrounds normalized for 0.5×10^{20} protons-on-target worth of data, for reconstructed neutrino energy below 2.5 GeV. This comprises the sideband region.	95
261	7.10 Distribution of signal (green) and backgrounds normalized for 0.5×10^{20} protons-on-target worth of data, for reconstructed neutrino energy between 2.5 GeV and 5 GeV. This comprises the signal region, which has an 81% purity of ν_μ^{CC} interactions from K^+ decay in the beam.	96
266	7.11 A two-dimensional plot of energy versus angle for all kaons in the beam pro- ducing ν_μ^{CC} interactions in the detector.	97
267	7.12 A two-dimensional plot of energy versus angle for the subset of kaons in Figure 7.11 which are reconstructed and selected for this analysis (having reconstructed neutrino energy above 2.5 GeV).	98
271	7.13 The kaon production angle distribution for all kaons in the beam producing ν_μ^{CC} interactions in the detector (red), the subset of those which are recon- structed and selected in both the sideband and signal region (blue) and the subset of those in the Kaon enriched signal sample, with reconstructed neu- trino energy above 2.5 GeV (green).	99
276	7.14 The kaon production energy distribution for all kaons in the beam producing ν_μ^{CC} interactions in the detector (red), the subset of those which are recon- structed and selected in both the sideband and signal region (blue) and the subset of those in the Kaon enriched signal sample, with reconstructed neu- trino energy above 2.5 GeV (green).	100

281	<i>7.15 The distribution of length of the longest track associated with the interaction contained within the fiducial volume for simulated backgrounds and signal (solid histograms) overlaid with data measurements (“on-beam” minus “off-beam” drawn in purple) for the sideband region in which reconstructed neutrino energy is less than 2.5 GeV. Statistical error bars are drawn on the data points, taking into account statistics from both the “on-beam” and “off-beam” samples. Below the main figure is a bin-by-bin ratio of data divided by simulation.</i>	102
289	<i>7.16 The distribution of track multiplicity (number of tracks associated with the interaction) for simulated backgrounds and signal (solid histograms) overlaid with data measurements (“on-beam” minus “off-beam” drawn in purple) for the sideband region in which reconstructed neutrino energy is less than 2.5 GeV. Statistical error bars are drawn on the data points, taking into account statistics from both the “on-beam” and “off-beam” samples. Below the main figure is a bin-by-bin ratio of data divided by simulation.</i>	103
296	<i>7.17 The distribution of ϕ angle (measured in radians with respect to the vertical) of the longest track associated with the interaction for simulated backgrounds and signal (solid histograms) overlaid with data measurements (“on-beam” minus “off-beam” drawn in purple) for the sideband region in which reconstructed neutrino energy is less than 2.5 GeV. Statistical error bars are drawn on the data points, taking into account statistics from both the “on-beam” and “off-beam” samples. Below the main figure is a bin-by-bin ratio of data divided by simulation.</i>	104

304	7.18 The distribution of θ angle (measured in radians with respect to the beam direction) of the longest track associated with the interaction for simulated backgrounds and signal (solid histograms) overlaid with data measurements (“on-beam” minus “off-beam” drawn in purple) for the sideband region in which reconstructed neutrino energy is less than 2.5 GeV. Statistical error bars are drawn on the data points, taking into account statistics from both the “on-beam” and “off-beam” samples. Below the main figure is a bin-by-bin ratio of data divided by simulation.	105
312	7.19 The distribution of multiple Coulomb scattering computed energy for the longest track associated with the interaction for simulated backgrounds and signal (solid histograms) overlaid with data measurements (“on-beam” minus “off-beam” drawn in purple) for the sideband region in which reconstructed neutrino energy is less than 2.5 GeV. Statistical error bars are drawn on the data points, taking into account statistics from both the “on-beam” and “off-beam” samples. Below the main figure is a bin-by-bin ratio of data divided by simulation. This plot has fewer entries than previous plots because only tracks longer than 1 meter have an associated MCS momentum as described in Section 7.3.	106
322	7.20 The distribution of reconstructed neutrino energy for simulated backgrounds and signal (solid histograms) overlaid with data measurements (“on-beam” minus “off-beam” drawn in purple) for the sideband region in which reconstructed neutrino energy is less than 2.5 GeV. Statistical error bars are drawn on the data points, taking into account statistics from both the “on-beam” and “off-beam” samples. Below the main figure is a bin-by-bin ratio of data divided by simulation.	107

329	7.21 <i>The distribution of reconstructed neutrino energy for simulated backgrounds</i>	
330	<i>and signal (solid histograms) overlaid with data measurements (“on-beam”</i>	
331	<i>minus “off-beam” drawn in purple) for the higher-energy end of the sideband</i>	
332	<i>region in which reconstructed neutrino energy is between 1.5 and 2.5 GeV.</i>	
333	<i>Statistical error bars are drawn on the data points, taking into account statis-</i>	
334	<i>tics from both the “on-beam” and “off-beam” samples. Below the main figure</i>	
335	<i>is a bin-by-bin ratio of data divided by simulation.</i>	108
346	7.22 <i>The distribution of reconstructed neutrino energy for simulated backgrounds</i>	
347	<i>and signal (solid histograms) overlaid with data measurements (“on-beam”</i>	
348	<i>minus “off-beam” drawn in purple) for the signal region in which recon-</i>	
349	<i>structured neutrino energy is greater than 2.5 GeV. Statistical error bars are</i>	
350	<i>drawn on the data points, taking into account statistics from both the “on-</i>	
351	<i>beam” and “off-beam” samples. Below the main figure is a bin-by-bin ratio</i>	
352	<i>of data divided by simulation.</i>	109
343	8.1 A diagram of the time projection chamber of the MicroBooNE detector.	
344	PMTs (not shown) are located behind the wire planes.	113
345	8.2 The particle’s trajectory is deflected as it traverses the material. The angular	
346	scatter in the labeled x' plane is shown as θ_x	115
347	8.3 Fitted Highland parameter S_2 as a function of true segment momentum for	
348	$\ell = X_0$ simulated muons in the MicroBooNE LArTPC. Blue x- error bars	
349	indicate the true momentum bin width with data points drawn at the center	
350	of each bin. Shown in red is a fit to these data points with functional form	
351	$a \times p^{-2} + c$, with best fit values for parameters a and c shown in the legend.	117
352	8.4 The Highland scattering RMS σ_o^{HL} for 14 cm segment lengths and 0 detector-	
353	inherent angular resolution as a function of true momentum before and after	
354	tuning. In red is shown equation 8.3 (the nominal Highland formula using	
355	$S_2 = 13.6$ MeV) and in blue is the retuned Highland formula (replacing S_2	
356	with $\kappa(p)$).	118

357	8.5 Range-based energy fractional bias (a) and resolution (b) from a sample of simulated fully contained BNB neutrino-induced muons using true starting and stopping positions of the track. The bias is less than 1% and the resolution is below $\approx 4\%$	122
361	8.6 Segment-to-segment measured angular scatters in both the x' and y' directions divided by the width σ_o^{RMS} predicted by the Highland formula (equation 8.1) for the automatically selected beam neutrino-induced fully contained muon sample in MicroBooNE data after hand scanning to remove poorly reconstructed tracks and obvious mis-identification topologies.	125
366	8.7 MCS-computed momentum versus range momentum for the automatically selected beam neutrino-induced fully contained muon sample in MicroBooNE data after hand scanning to remove poorly reconstructed tracks and obvious mis-identification topologies. The color (z) scale indicates number of tracks.	126
370	8.8 Inverse momentum difference (as defined in the text) fractional bias (top) and resolution (bottom) for automatically selected contained ν_μ CC-induced muons from full simulated BNB events with cosmic overlay where the track matches with the true muon track (blue), and automatically selected and hand-scanned (see text) contained ν_μ CC-induced muons from MicroBooNE data (green).	127
376	8.9 Inverse momentum difference (as defined in the text) fractional bias (top) and resolution (bottom) for automatically selected contained ν_μ CC-induced muons from full simulated BNB events with cosmic overlay where the track matches with the true muon track both using the nominal Highland formula (equation 8.2) (red) and the retuned Highland formula (equation 8.5) (blue).	129
381	8.10 MCS-computed momentum versus true momentum for the sample of simulated exiting BNB ν_μ CC muons in MicroBooNE with at least one meter of track contained within the TPC. The color (z) scale indicates number of tracks.	130
384	8.11 Fractional momentum difference for a few representative bins of true momentum for a sample of simulated exiting muon tracks. The y-axis is number of tracks, and the x-axis is $(p_{\text{MCS}}^{-1} - p_{\text{true}}^{-1})/(p_{\text{true}}^{-1})$	131

- ³⁸⁷ 8.12 MCS momentum fractional bias (top) and resolution (bottom) as a function
³⁸⁸ of true momentum from a sample of exiting reconstructed muon tracks. . . 132

³⁸⁹ List of Tables

416

⁴¹⁷ Acknowledgments

418

⁴¹⁹ The acknowledgments go here.

420 Chapter 1

421 Introduction

422 This thesis describes work towards the search for a low energy excess in MicroBooNE. What
423 MicroBooNE is, what the low energy excess is, and how one searches for the latter in the
424 former will be described in detail.

425

426 To begin, Chapter 2 will provide some introductory theoretical background about neutrinos both within and beyond the Standard Model of physics. Following that, Chapter 3 will
427 describe the MicroBooNE detector, located at the Fermi National Accelerator Laboratory
428 in Batavia, IL. This detector employs a liquid argon time projection chamber (LArTPC),
429 a relatively new technology for neutrino detection, especially at the size of MicroBooNE
430 (with order of meters drift distance). Next, Chapter 4 will describe the Booster Neutrino
431 Beam (BNB), the beam of neutrinos produced at Fermilab by colliding primary protons
432 with a beryllium target and focusing the outgoing charged secondaries. The relatively large
433 uncertainties associated with the neutrino flux will be introduced, which are particularly
434 important for the analyses described in this thesis. Chapter 5 goes on to describe in detail
435 the excess of electron-like events seen in primarily ν_μ beams, first by the LSND collaboration
436 and then again by the MiniBooNE collaboration. Ultimately the MiniBooNE collaboration
437 was unable to resolve whether the excess is of electron-like events, or photon-like events
438 due to limitations of the detector technology. For this reason, the MicroBooNE experiment
439 was proposed to measure the same neutrino beam at a similar location to MiniBooNE, but
440 with the different LArTPC detector technology that has photon/electron discrimination
441 with the different LArTPC detector technology that has photon/electron discrimination

442 capabilities.

443

444 Chapter 6 describes a simulation-based analysis done to estimate the sensitivity of the
445 MicroBooNE detector to measure a MiniBooNE-like excess, with some assumptions about
446 that excess. This is an important analysis to identify which sources of backgrounds are
447 most relevant to this search in order to step closer to an eventual search for the excess in
448 MicroBooNE data. As will be described, the dominant background to this search is the
449 intrinsic ν_e contamination in the beam, about half of which come from K^+ production at
450 the BNB proton target. There is a relatively large flux uncertainty associated with with
451 this K^+ production, which is the subject of Chapter 7.

452

453 Chapter 7 presents the first steps toward a K^+ production at the BNB primary pro-
454 ton target measurement in MicroBooNE. This analysis selects and analyses high energy ν_μ
455 interactions in MicroBooNE, which provide a pure sample of ν_μ from K^+ decay. The *in*
456 *situ* measurement of these interactions is used to constrain the aforementioned important
457 intrinsic ν_e from K^+ background for the low energy excess search.

458

459 In order to make the kaon production measurement, calculating the energy of several-
460 GeV muons from ν_μ interactions in MicroBooNE is a necessary step. Given the muon
461 kinematics in liquid argon, these particles travel on average many meters and almost al-
462 ways exit the active detector volume. Chapter 8 presents a publication (whose first author
463 is the author of this thesis) describing in detail the multiple Coulomb scattering based
464 method used to estimate the energy of muons which exit a LArTPC. The publication de-
465 scribes important discovery made about the underlying phenomenological formula which
466 past LArTPC neutrino experiments have neglected: the formula needs to be re-tuned for
467 use specifically in liquid argon.

468

469 The thesis concludes with a summary of the results of the three analyses described,
470 along with the future prospects for those analyses and for the MicroBooNE experiment in
471 general.

⁴⁷² Chapter 2

⁴⁷³ **Neutrinos, Neutrino Oscillations,
⁴⁷⁴ and Sterile Neutrinos**

⁴⁷⁵ **2.1 Introduction to Neutrinos**

⁴⁷⁶ In 1914, James Chadwick measured the energy spectrum of outgoing electrons in beta decay
⁴⁷⁷ and showed that the spectrum was continuous [1], though it was expected to consist of one
⁴⁷⁸ discrete, well defined value due to the presumed two-body nature of the decay. While some
⁴⁷⁹ chose to believe that a lack of energy conservation is the underlying cause of the continuous
⁴⁸⁰ spectrum, in 1930 Pauli proposed (translated from German) [2]:

⁴⁸¹ “...in the nuclei there could exist electrically neutral particles, which I will call
⁴⁸² neutrons, that have spin 1/2 and obey the exclusion principle and that further
⁴⁸³ differ from light quanta in that they do not travel with the velocity of light...
⁴⁸⁴ The continuous beta spectrum would then make sense with the assumption that
⁴⁸⁵ in beta decay, in addition to the electron, a neutron is emitted such that the
⁴⁸⁶ sum of the energies of neutron and electron is constant.”

⁴⁸⁷ Though Pauli named the particle a “neutron” (a name later used for the subatomic particle
⁴⁸⁸ comprised of two down quarks and one up quark), his prediction was otherwise correct.
⁴⁸⁹ Only 26 years later in 1956, the first neutrino was observed.

491 Neutrinos make up three of the six leptons in the Standard Model of particle physics.
492 There are three flavor eigenstates, each of which are paired to one of the other three leptons:
493 electron neutrinos (ν_e), muon neutrinos (ν_μ), and tau neutrinos (ν_τ). Each neutrino has an
494 antiparticle partner, the antineutrino. Neutrinos are particularly elusive because they are
495 electrically neutral and only interact through the weak interaction and gravity. The number
496 of active neutrino flavors is constrained to three (2.984 ± 0.0082) by precision measurements
497 of the Z decay width [3].

498

499 The flavor of a neutrino is determined by measuring the outgoing lepton in charged cur-
500 rent neutrino interactions. In such an interaction, a ν_e produces an electron, a ν_μ produces
501 a muon, and a ν_τ produces a tau.

502

503 2.2 Neutrino Oscillations

504 It was until 1968 that neutrinos were widely believed to be massless. In this year, Ray Davis
505 and collaborators were measuring neutrinos originating from within the sun (“solar neutrini-
506 nos”) by studying charged-current ν_e interactions on chlorine atoms. They measured only
507 one third as many neutrino interactions as expected, a fact which wasn’t fully understood
508 until 2001. By combining results from other experiments (including from the Kamiokande
509 experiment in Japan measuring a deficit of ν_μ from cosmic ray interactions in the atmo-
510 sphere in 1988 [4], and from the Sudbury Neutrino Observatory (SNO) experiment [5]),
511 the idea that neutrinos oscillated from one flavor to another became widely accepted.

512

513 Neutrino oscillations occur when a neutrino produced as one flavor eigenstate changes
514 to another flavor eigenstate after propagating a distance, L . Oscillation is only possible
515 because the three mass eigenstates are non-zero and are different than the three flavor
516 eigenstates. Neutrino propagation happens as a mixture of mass eigenstates with different
517 DeBroglie wavelengths, which constructively and destructively interfere with one another.
518 The mass eigenstates are referred to as ν_1 , ν_2 , and ν_3 with masses m_1 , m_2 , and m_3 respec-

tively. While the absolute masses are yet unknown, the mass-squared splitting between the masses have been measured ($\Delta m_{i,j}^2 = m_j^2 - m_i^2$). This introduces two possible ordering configurations of the neutrino masses: the “normal” hierarchy in which $m_1 < m_2 < m_3$, and the “inverted” hierarchy, in which $m_3 < m_1 < m_2$. The two hierarchy possibilities are depicted in Figure 2.1 [6]. As seen in the figure, the larger of the two mass splittings is referred to as Δm_{atm}^2 and the smaller of the two is referred to Δm_{sol}^2 because they are generally measured with atmospheric neutrinos or solar neutrinos, respectively.

526

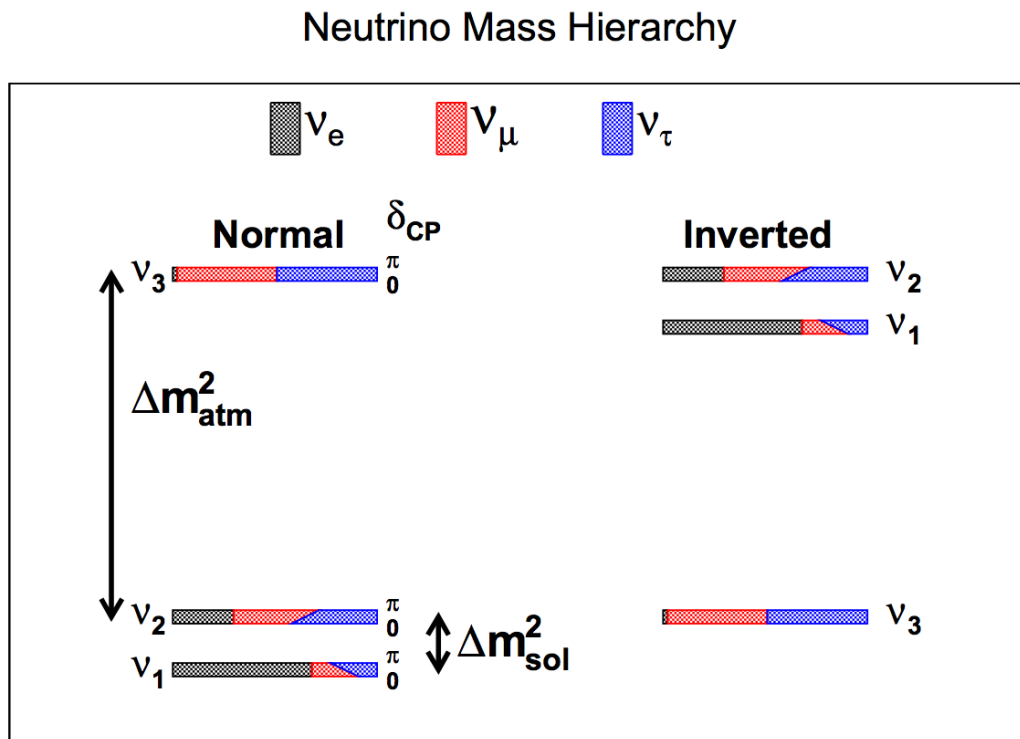


Figure 2.1: The neutrino mass hierarchy possibilities. The flavor eigenstate fraction for each mass eigenstate is shown by the relative amount of gray, red, or blue in each bar.

A neutrino mass eigenstate can be expressed as a quantum superposition of flavor eigenstates by way of the Pontecorvo-Maki-Nakagawa-Sakata (PMNS) 3×3 unitary mixing matrix, U :

$$|\nu_i\rangle = \sum_{\alpha}^3 U_{i,\alpha} |\nu_{\alpha}\rangle \quad (2.1)$$

530 where $|\nu_i\rangle$ represents the i th mass eigenstate ($i = 1, 2, 3$) and $|\nu_\alpha\rangle$ represents the flavor
531 eigenstate ($\alpha = e, \mu, \tau$). Generally the PMNS matrix is factorized into three matrices
532 parameterized by four parameters: three mixing angles θ_{12} , θ_{23} , θ_{13} , and one CP violating
533 phase δ .

$$U = \begin{bmatrix} 1 & 0 & 0 \\ 0 & c(\theta_{23}) & s(\theta_{23}) \\ 0 & -s(\theta_{23}) & c(\theta_{23}) \end{bmatrix} \begin{bmatrix} c(\theta_{13}) & 0 & s(\theta_{13})e^{-i\delta} \\ 0 & 1 & 0 \\ -s(\theta_{13})e^{-i\delta} & 0 & c(\theta_{13}) \end{bmatrix} \begin{bmatrix} c(\theta_{12}) & s(\theta_{12}) & 0 \\ -s(\theta_{12}) & c(\theta_{12}) & 0 \\ 0 & 0 & 1 \end{bmatrix} \quad (2.2)$$

534 where “c” stands for cos and “s” stands for sin.

535

536 In general, an experiment searching for neutrino oscillations has the choice of search-
537 ing for appearance or disappearance. In appearance experiments, a neutrino of one known
538 flavor is produced (flavor α), and one attempts to measure that neutrino as another flavor
539 (flavor β). Appearance searches have the added benefit of potentially shedding light on
540 CP violation, which leads to appearance probabilities $P(\nu_\alpha \rightarrow \nu_\beta) \neq P(\bar{\nu}_\alpha \rightarrow \bar{\nu}_\beta)$. In
541 a disappearance search, neutrinos of known flavor are produced at a known rate, and a
542 decreased rate (deficit) of that same neutrino flavor is measured a distance away. Since
543 $P(\nu_\alpha \rightarrow \nu_\alpha) = P(\bar{\nu}_\alpha \rightarrow \bar{\nu}_\alpha)$, disappearance searches allow for the combination of neutrino
544 and anti-neutrino data for increased oscillation sensitivity.

545

546 A classic graduate-student quantum mechanical qualification exam question is to deter-
547 mine an oscillation probability assuming only two neutrinos. This can be parameterized
548 with one effective mixing angle, θ , and the nominal rotation matrix

$$U = \begin{bmatrix} \cos \theta & \sin \theta \\ -\sin \theta & \cos \theta \end{bmatrix}. \quad (2.3)$$

549 A neutrino of flavor ν_α will propagate as the superposition of the two mass eigenstates, ν_1
550 and ν_2

$$|\nu_\alpha(t)\rangle = \cos(\theta)e^{-iE_1 t} |\nu_1\rangle + \sin(\theta)e^{-iE_2 t} |\nu_2\rangle \quad (2.4)$$

551 Using the relativistic approximation (which is valid for neutrinos of almost any momenta,

552 p , given their small mass, m)

$$E_i = p_i + \frac{m_i^2}{2p_i} \quad (2.5)$$

553 the oscillation probability for a neutrino of flavor α to be detected as flavor β after traveling
554 a distance L at approximately the speed of light is given by

$$P_{\alpha \rightarrow \beta} = |\langle \nu_\alpha | \nu_\beta \rangle|^2 = \sin^2 2\theta \sin^2 \left(1.27 \frac{\Delta m^2 L}{E} \right) \quad (2.6)$$

555 where the 1.27 factor comes from a proper handling of units including \hbar and c . The L/E
556 frequency modulation of oscillations is characteristic of two neutrino measurements, for
557 example as beautifully demonstrated by the KamLAND collaboration measuring Δm^2_{21}
558 and θ_{12} with nuclear reactor anti-neutrinos, as shown in Figure 2.2 [7].

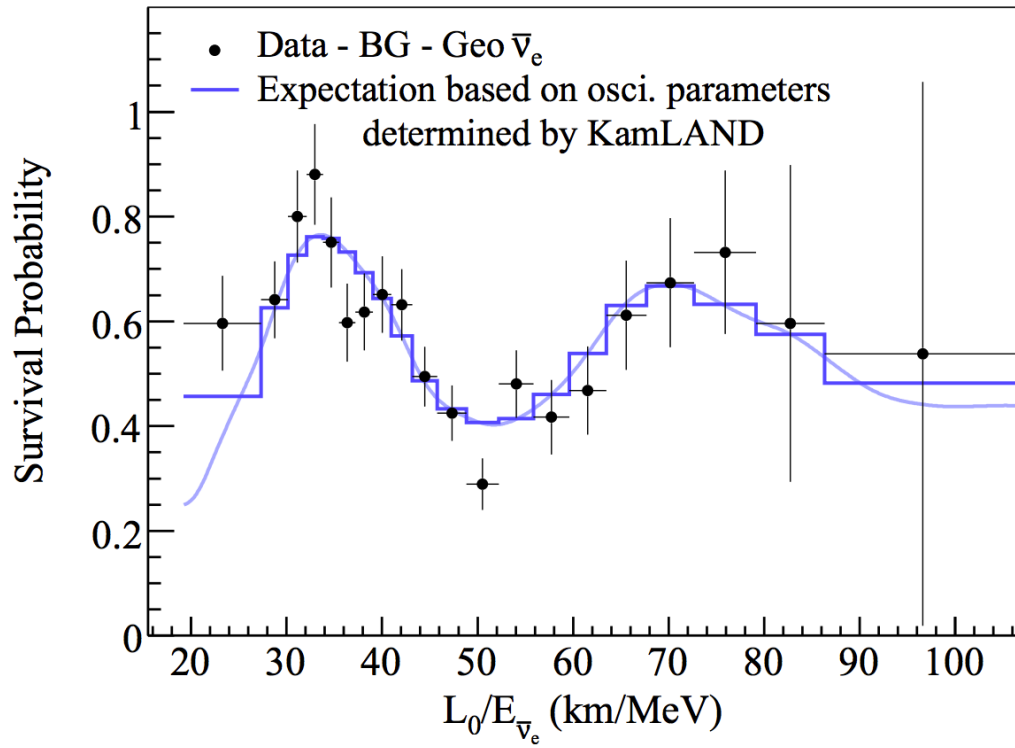


Figure 2.2: Results from the KamLAND collaboration measuring the survival probability of $\bar{\nu}_e$ from nuclear reactors. A clear oscillation as a function of L/E as predicted by the two-neutrino model is shown.

559 2.3 Sterile Neutrinos

560 While it is well known that there are only three active neutrino flavor states from the
561 measured width of the Z decay, it is possible to introduce one or more “sterile” neutrino
562 states which do not couple weakly. Each addition of a sterile neutrino adds a row and
563 column to the PMNS mixing matrix, and a new sterile mass eigenstate is defined as

$$|\nu_s\rangle = \sum_{\alpha}^{3+N} U_{i,\alpha} |\nu_{\alpha}\rangle \quad (2.7)$$

564 where N is the number of additional sterile neutrinos added to the model.

565

566 Proposing the existence of one or more sterile neutrino eigenstates was inspired by the
567 results of the LSND and MiniBooNE experiments, which are discussed in more detail in
568 Chapter 5. LSND observed an excess of $\bar{\nu}_e$ -like interactions in a $\bar{\nu}_{\mu}$ beam [8]. When fit to
569 the three-neutrino oscillation model, the excess strongly disagreed with other measurements
570 of neutrino mixing angles and Δm^2 values. The fit value of Δm^2 was on the order of 1
571 eV^2 , orders of magnitude higher than previously measured values of Δm_{12}^2 and Δm_{23}^2 . The
572 existence of one or more sterile neutrinos could explain this drastically different measured
573 Δm^2 value, since new additional mass eigenstate(s) are included in the propagating su-
574 perposition, therefore changing neutrino oscillation probabilities. Including this measured
575 sterile neutrino mass splitting in the “normal” or “inverted” hierarchy is shown in Figure
576 2.3 [9].

577

578 Following the LSND experiment, the MiniBooNE experiment was proposed to search
579 for oscillations with a similar mass splitting to that measured by LSND. In 2010, Mini-
580 BooNE observed a two anti-neutrino oscillation appearance-only measurement consistent
581 with LSND over the null oscillation hypothesis at the 98% confidence level.

582

583 The following chapter of this thesis provides an introduction to the MicroBooNE de-
584 tector, which was proposed to search for the same MiniBooNE excess but with a different
585 detector technology.

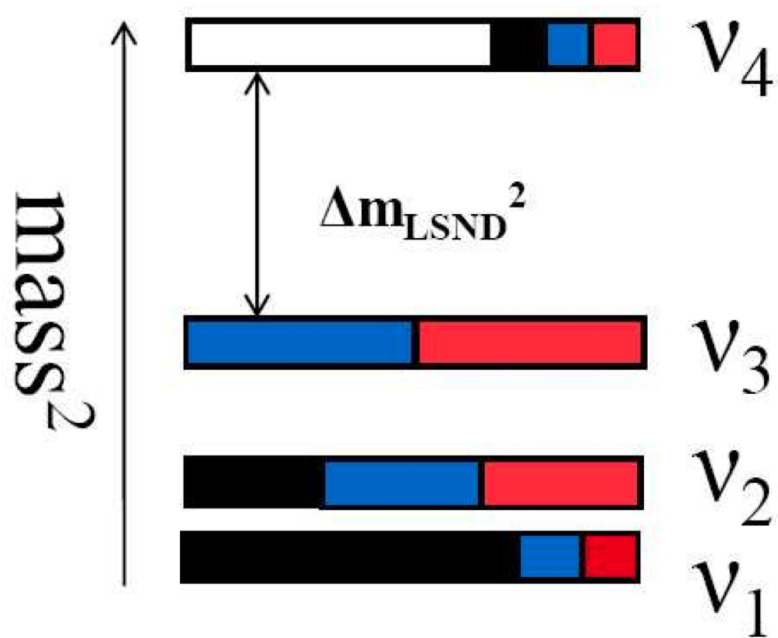


Figure 2.3: *Mass hierarchy with one heavy sterile neutrino included. The δm^2 from LSND is incorporated.*

*CHAPTER 2. NEUTRINOS, NEUTRINO OSCILLATIONS, AND STERILE
NEUTRINOS*

586 **Chapter 3**

587 **The MicroBooNE Detector**

588 The purpose of this chapter is to explain the technical details of the MicroBooNE detector.
589 An understanding of how a liquid argon time projection chamber like MicroBooNE works
590 is crucial for understanding the results of analyses described in later chapters. Using this
591 specific detector technology gives rise to certain backgrounds in measurements which are
592 relevant to MicroBooNE that may not be relevant for other experiments using different
593 detection techniques, like MiniBooNE. Additionally, understanding how the detector works
594 sheds light on what detector-specific uncertainties are present in MicroBooNE analyses.

595 **3.1 Introduction**

596 The MicroBooNE (the Micro Booster Neutrino Experiment) detector [10] is a \sim 60 ton fidu-
597 cial mass (170 ton total mass) liquid argon time projection chamber (LArTPC) contained
598 within a cylindrical cryostat, located on-axis of the Booster Neutrino Beam-line (BNB) 470
599 meters downstream from the neutrino production target at the Fermi National Accelerator
600 Laboratory (FNAL) in Batavia, Illinois. A schematic of how a LArTPC works is shown in
601 Figure 3.1. A LArTPC involves a detector medium in an external electric field. Particles
602 traversing the medium both create scintillation light, which are observed by photomultiplier
603 tubes (PMTs, not shown in Figure 3.1) and leave trails of ionization electrons. These ion-
604 ization electrons are drifted by the electric field past a number of closely spaced wire planes
605 at different pitch angles. The signals generated in each plane as the electrons either pass

606 close to wires or are collected on wires are what are used to create a two-dimensional image
 607 of the event. Combining information from multiple planes along with that from the PMTs
 608 allows for the creation of three-dimensional reconstructions of the event. Additionally, the
 609 relative size of the signals on the wire planes provide calorimetric information, which is used
 610 for particle identification capabilities.

611

612 The main components of the MicroBooNE TPC (the TPC, the light collection system,
 613 and the readout and triggering system) are described in the following sections.

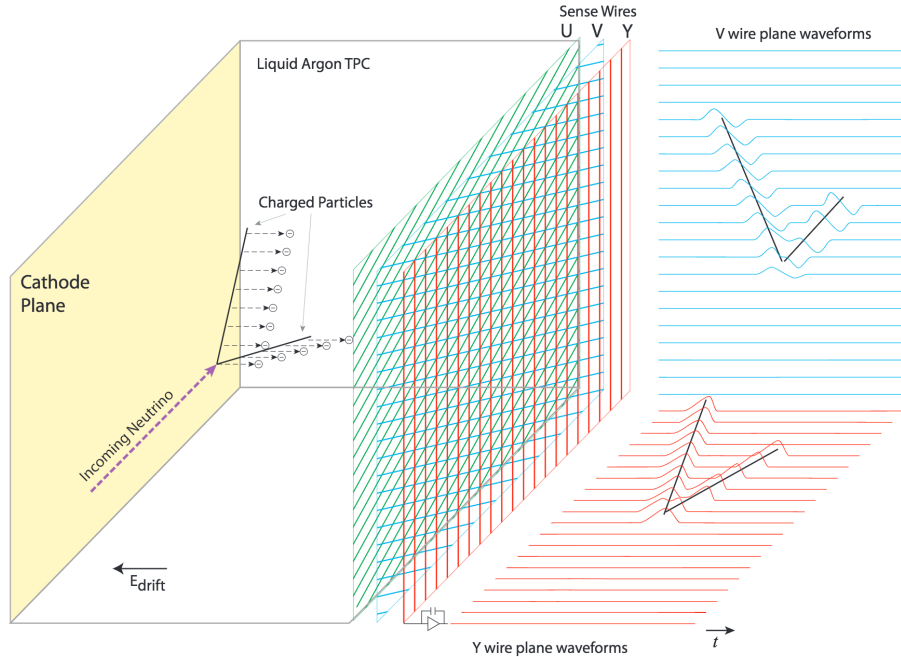


Figure 3.1: A cartoon schematic of how a LArTPC works. Ionization electrons from particles traversing the detector medium are drifted by an electric field, E_{drift} past multiple planes of sense wires. The signals on those wires create several two-dimensional images of the event, which are combined to create a three-dimensional reconstruction of the event. Note that in a LArTPC, PMTs are used to collect scintillation light, but are not drawn in this diagram.

614 3.2 Time Projection Chamber

615 The time projection chamber (TPC) used in the MicroBooNE experiment is a rectangular
616 prism with dimensions 2.3 m vertical \times 2.6 m horizontal \times 10.4 m length (along the beam
617 direction). The 8256 stainless steel sense wires forming the anode planes have a plane-to-
618 plane spacing of 3 mm, and the wires on each plane are separated with a 3 mm wire pitch.
619 The wires are connected to application-specific integrated circuits (ASICs) which operate
620 at liquid argon temperatures. There are three wire planes. The first two planes (from the
621 point of view of drifting electrons) each consist of 2400 wires and are induction planes, at
622 angles ± 60 degrees relative to the vertical. The third wire plane consists of 3456 wires and
623 is a collection plane, with vertically oriented wires. The electric field is created by a series
624 of 64 2.54 cm diameter stainless steel pipes shaped into a rectangular loop held in place
625 by a frame built of G10, forming the field cage. The negatively charged cathode is held
626 at a high voltage (operating voltage is 70kV), and this voltage is incrementally stepped
627 down across the field cage tubes with a voltage divider chain, with an equivalent resistance
628 of $250 \text{ M}\Omega$ between each tube. The distance from center-to-center of adjacent field cage
629 loops is 4 cm. This creates a uniform electric field within the LArTPC. A 3D rendering
630 of the MicroBooNE TPC within the cryostat is shown in Figure 3.2. A summary of the
631 MicroBooNE LArTPC design parameters and nominal operating conditions are described
632 in Table 3.1 [10].

633 3.3 Light Collection System

634 An important ingredient to the ultimate 3D reconstruction of particle interactions within a
635 LArTPC is the light collection system. While the wire signals alone suffice to reconstruct
636 3D interactions, the absolute timing of the event (referred to as t_0) is unknown so there
637 is ambiguity in the drift direction. Since the time scale with which scintillation light is
638 created and propagates (nanoseconds) is orders of magnitude faster than that with which
639 ionization electrons drift (milliseconds), measuring this light allows to clarify this ambiguity
640 to high precision. Additionally, the scintillation light from interactions is relatively local-
641 ized, and therefore combining the measured PMT signals with the physical position of the

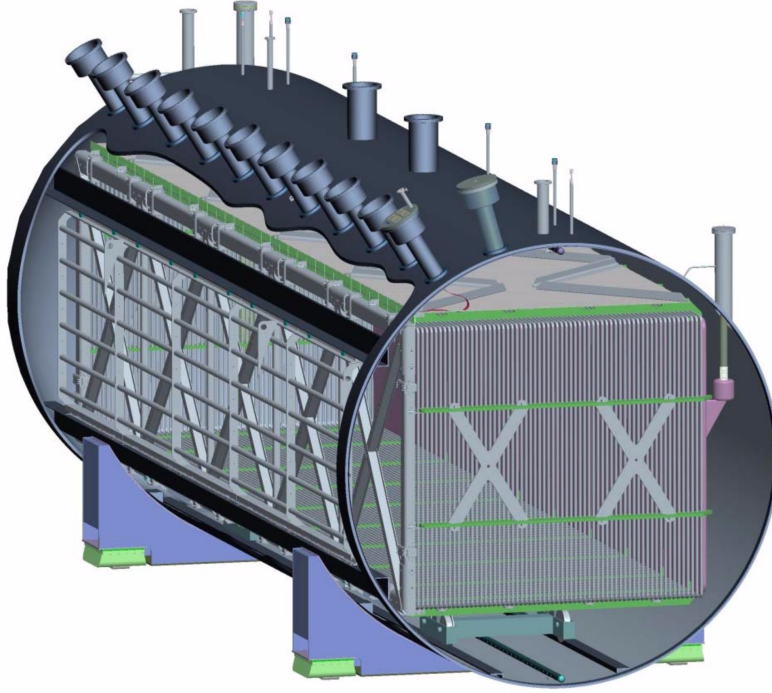


Figure 3.2: A 3D rendering of the MicroBooNE detector. The rectangular time projection chamber (TPC) fits within the cylindrical cryostat. The feedthroughs along the top allow for the PMT and sense wire signals to be read out to the DAQ. Not shown are the photomultiplier tubes (PMTs) located on the wall behind the sense wire planes.

642 signal allows to match individual flashes of light with different interactions, which may have
 643 different t_0 s. This is important to help tag and reject cosmic-induced backgrounds which
 644 may arrive outside of the expected beam neutrino arrival times.

645

646 The light collection system in MicroBooNE consists of 32 8-inch diameter Hamamatsu
 647 R5912-02mod cryogenic PMTs. These PMTs are mounted in a plane behind the three sense
 648 wire planes. The physical location of these PMTs is shown in Figure 3.3. These 32 PMTs
 649 provide 0.85% photocathode coverage. Each PMT has mounted in front of it an acrylic
 650 plate, as shown in Figure 3.4. This plate is coated with TPB, an organic fluor which serves
 651 as a wavelength-shifting material. TPB absorbs the VUV scintillation light photons (128
 652 nm wavelength in liquid argon) and re-emits it at visible wavelengths detectable by the

Table 3.1: MicroBooNE LArTPC design parameters and nominal operating conditions.

Parameter	Value
# Anode planes	3
Anode planes spacing	3 mm
Wire pitch	3 mm
Wire type	SS, diam. 150 μ m
Wire coating	2 μ m Cu, 0.1 μ m Ag
Design Wire tension	6.9N \pm 1.0N
# wires (total)	8256
# Induction plane (U) wires	2400
# Induction plane (V) wires	2400
# Collection plane (Y) wires	3456
Wire orientation (w.r.t. vertical)	+60°,-60°,0° (U,V,Y)
Cathode voltage (nominal)	-128 kV
Bias voltages (U,V,Y)	-200 V, 0 V, +440 V
Drift-field	500 V/cm
Max. Drift Time, Cathode to U (at 500 V/cm)	1.6 ms
# Field-cage steps	64
Ring-to-ring voltage step	2.0 kV

⁶⁵³ PMTs, peaked at 425 nm.

⁶⁵⁴ 3.4 Electronics, Readout, and Triggering

⁶⁵⁵ Both of the two main subsystems of the MicroBooNE LArTPC (the TPC sense-wire planes
⁶⁵⁶ and the optical PMTs) create analog signals which must be read out and digitized for use
⁶⁵⁷ in analyses. This process involves amplification and shaping of the signals, and ultimately
⁶⁵⁸ ends with the data acquisition (DAQ) software writing the digitized data to disk. While
⁶⁵⁹ the readout is designed to have an additional data stream that continually writes to disk
⁶⁶⁰ (designed with the hopes of measuring neutrino interactions from a potential future super-

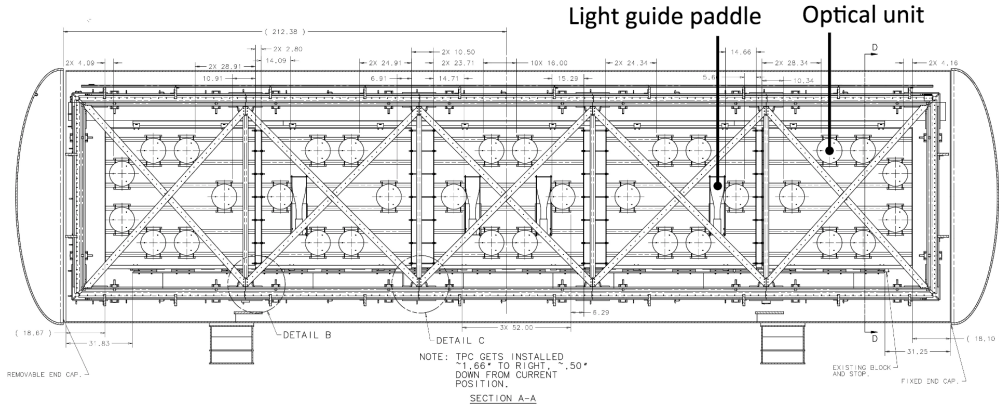


Figure 3.3: A side-on view of the MicroBooNE detector showing the location of the 32 PMTs (labeled “optical units”) and the four light guide paddles.

661 nova explosion), the primary data stream reads out and stores signals only for a brief period
 662 of time when a hardware trigger is issued. The specifics of the readout and triggering for
 663 MicroBooNE are discussed in this section.

664

665 A schematic overview of the TPC and PMT signal processing and readout stages is
 666 shown in Figure 3.5. The analog signals from the 8256 sense wires in the TPC pass through
 667 CMOS analog front end ASICs which operate on cold motherboards at liquid argon tem-
 668 peratures. The signals are then shaped and amplified by cold intermediate amplifiers before
 669 passing through a warm feed-through. The signals are received by custom-designed LArTPC
 670 readout modules distributed over nine readout crates, which digitize the signals and pro-
 671 cess them. The TPC wire signals are digitized at 16 MHz and then down-sampled in the
 672 digitization process to 2 MHz. The TPC system reads out four 1.6 ms frames of wire signal
 673 data associated with one event. This time is chosen based on how long it takes ionization
 674 electrons from the cathode side of the TPC to drift to the anode wires (roughly 1.6 ms
 675 depending on drift field). Reading out one frame before a trigger is issued, along with two
 676 frames after ensures enough data is available to identify both a neutrino interaction, as well
 677 as all cosmic ray signals that arrive soon enough before or after the neutrino which need to
 678 be reconstructed in analyses.

679

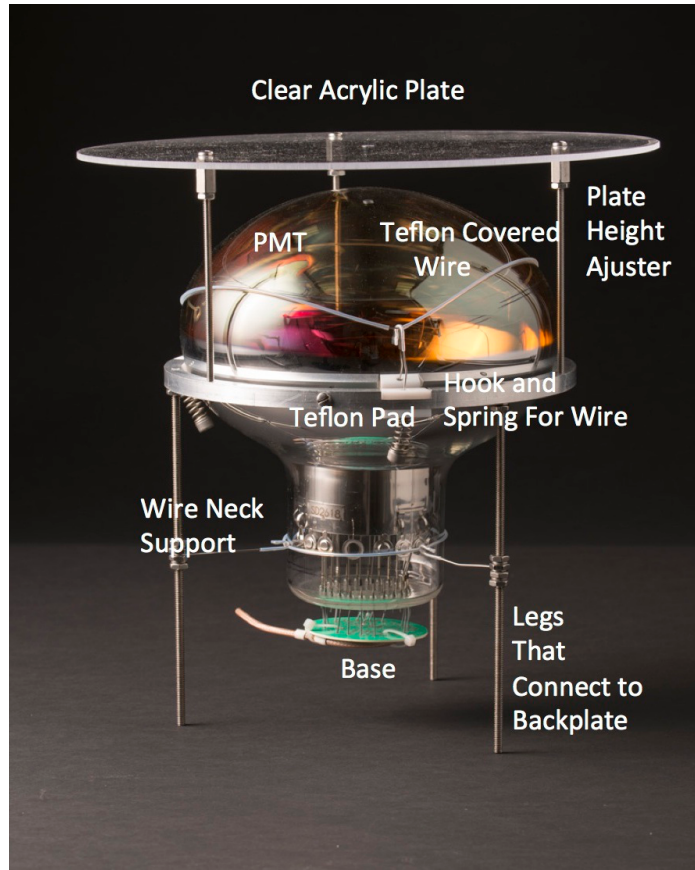


Figure 3.4: *A picture of one of the 8 inch Hamamatsu R5912-02mod cryogenic photomultiplier tubes (PMT) used in the MicroBooNE detector. Note the clear acrylic plate, which is coated with a wavelength-shifting organic fluor (TPB) before installation to convert the VUV liquid argon scintillation light into the visible spectrum, detectable by the PMT.*

680 A similar process occurs for the PMT signals. The PMT signals undergo separate shap-
 681 ing with a 60 ns peaking time to allow for digitization of several samples on the rising edge
 682 of a signal for more precise timing reconstruction abilities. The PMT signals are digitized at
 683 64 MHz , but are not read out continuously during the same $4 \times 1.6\text{ ms}$ TPC readout time;
 684 only shaped PMT signals above a small discriminator threshold are read out and stored
 685 for later reconstruction. The PMT signals are split into high- and low- gain channels, to
 686 extend the dynamic range of the ADC.

687

688 The readout of both TPC and PMT systems are initiated by triggers formed in a separate

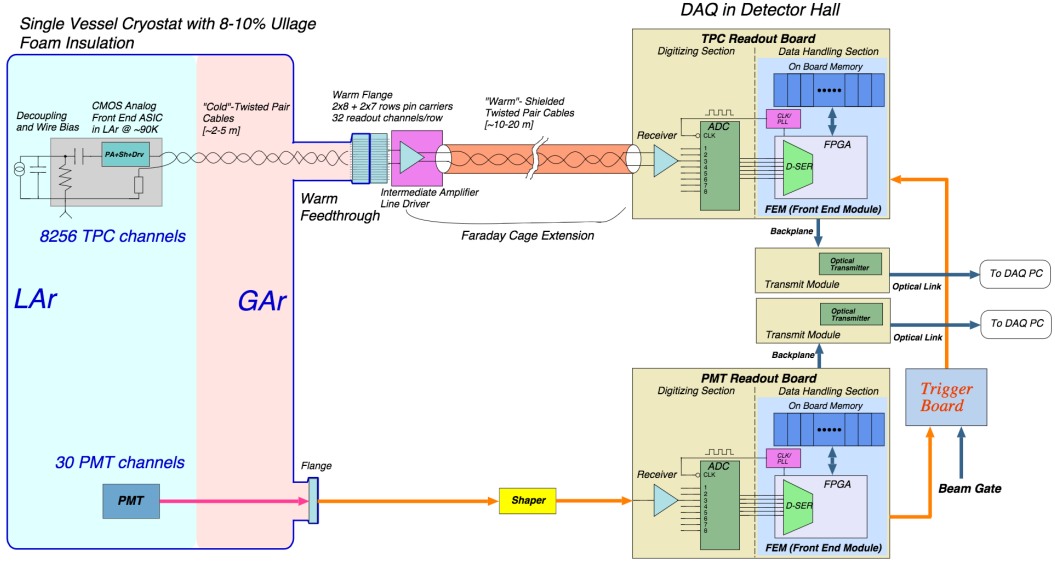


Figure 3.5: *The MicroBooNE readout schematic. On the left are portions of the readout operating at argon temperatures. Signals pass through feedthroughs into warm electronics readout boards, unique for the TPC (sense wire signals) and the light collection system (PMT signals). These signals are combined with external timing signals from the accelerator to form triggers that initiate readout of all systems.*

689 trigger board located in a warm electronics readout crate. While many different triggers are
 690 used by MicroBooNE, the one relevant for this analysis is the BNB trigger. To form this
 691 trigger, a timing signal from the BNB accelerator is shaped and fed into the trigger board.
 692 The FPGA firmware in the PMT front end readout modules generates a PMT trigger when
 693 PMT signal multiplicity is greater than 1 and summed PMT pulse-height is more than 2
 694 photo-electrons summed over all of the high gain PMT channels. If a PMT trigger is issued
 695 by the firmware in coincidence with the $1.6\mu s$ beam gate window from the accelerator, a
 696 BNB trigger is generated by the trigger board. This trigger signal is fanned-out to all
 697 readout crates (TPC and PMT), instructing them to initiate a readout simultaneously.
 698 Once the readout is complete, the data from each readout crate is packaged and shipped
 699 to the DAQ software, which assembles all of the data into one event in memory, which is

700 saved to disk and eventually used in reconstruction and analysis¹.

¹Ultimately, the MicroBooNE collaboration has moved towards using a software-based trigger for its beam-based analyses.

701 **Chapter 4**

702 **The Booster Neutrino Beam**

703 The purpose of this chapter is to describe how neutrinos are produced in the Booster Neu-
704 trino Beam-line (BNB) at the Fermi National Accelerator Laboratory. An understanding of
705 how these neutrinos are produced and their flux through the MicroBooNE detector is neces-
706 sary to properly interpret the results of the low energy excess analysis and kaon production
707 analysis, described in Chapters 5 and 6. In describing the neutrino production techniques,
708 the reader will be introduced to the sources of systematic uncertainties associated with the
709 neutrino production, both in terms of how they arise, and their magnitude.

710 **4.1 The Booster Neutrino Beam**

711 The Booster Neutrino Beam-line (BNB) collides protons at 8.89 GeV/c momentum from the
712 Fermilab Booster synchrotron with a beryllium target to produce a high flux of neutrinos.
713 The layout of the BNB is shown in Figure 4.1 [11], and the relevant steps of the neutrino
714 production process will be described in the following sections.

715 **4.1.1 Primary Proton Beam**

716 The protons originate from H_2 gas molecules converted to H^- ions via a Cockcroft-Walton
717 generator, and are initially accelerated to approximately 1 MeV kinetic energy. These ions
718 are subjected to a linear accelerator using alternating electromagnetic fields to increase
719 their energy to about 400 MeV. Passing through a carbon foil removes electrons, and the

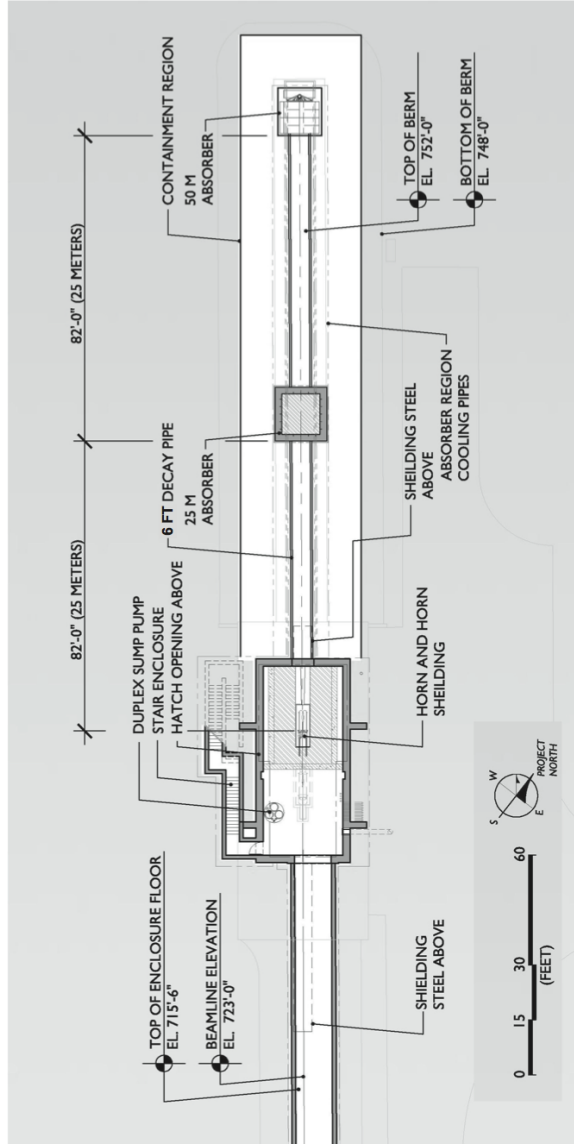


Figure 4.1: *Overall layout of the BNB. The primary proton beam, extracted from the Booster, enters the target hall from the left. Upon exiting the target hall, particles encounter a 50-meter-long decay region, terminating in the beam stop on the right.*

720 bare protons enter the Booster synchrotron where they are accelerated up to 8.89 GeV/c
 721 momentum. The protons are bunched in “beam spills” containing roughly 4×10^{12} protons
 722 spaced throughout a $1.6 \mu\text{s}$ time window per spill. The protons are then directed towards
 723 a thick beryllium target.

724

725 The absolute number of protons directed on target (POT) is measured by two toroids
726 upstream of the target which are part of a larger beam monitoring system. The error on
727 the POT is on the order of 2%. Additional beam characteristics are monitored by beam
728 position monitors (BPMs), a multi-wire chamber, and a resistive wall monitor (RWM) which
729 together measure beam intensity, timing, width, position, and direction.

730 **4.1.2 Proton Target and Focusing Horn**

731 The beryllium target is 71.1 cm long, which corresponds to 1.7 proton interaction lengths,
732 and is 0.51 cm in radius. Beryllium is chosen as the proton target because its relatively
733 low Z (4) minimizes radiative losses from the protons before their p-Be interactions which
734 produce secondary mesons (π^\pm , K^\pm , K_L^0).

735

736 The beryllium target is located within a larger focusing electromagnet, referred to as
737 the horn. A schematic drawing of the horn is shown in Figure 4.2. The horn is an alu-
738 minum alloy pulsed toroidal electromagnet. The pulsed current has a peak at 170 kA and
739 a time-width of 143 μs , coincident with the proton beam arrival time on the target. The
740 current flows along the inner conductor, then returns along the outer conductor. The mag-
741 netic fields created by this current have a maximum field value of 1.5 Tesla and fall off
742 as $1/R$ from the cylindrically symmetric axis of the horn. These fields serve to focus the
743 charged secondaries produced in the p-Be interactions. The direction of the current can be
744 switched to focus the positively charged secondaries, or the negatively charged secondaries,
745 ultimately producing a beam of primarily neutrinos (“neutrino mode”) or of primarily an-
746 tineutrinos (“antineutrino mode”) respectively.

747

748 Downstream of the horn is a concrete collimator (214 cm long, between 30 cm and 35.5
749 cm in radius) which absorbs particles that would not otherwise contribute to the neutrino
750 flux. Following the collimator is a 45 meter long (1 meter radius) air-filled cylindrical decay
751 region, ending in a beam-stop made of steel and concrete which contains an array of gas
752 proportional counters to detect muons penetrating the beam-stop. Also about half way

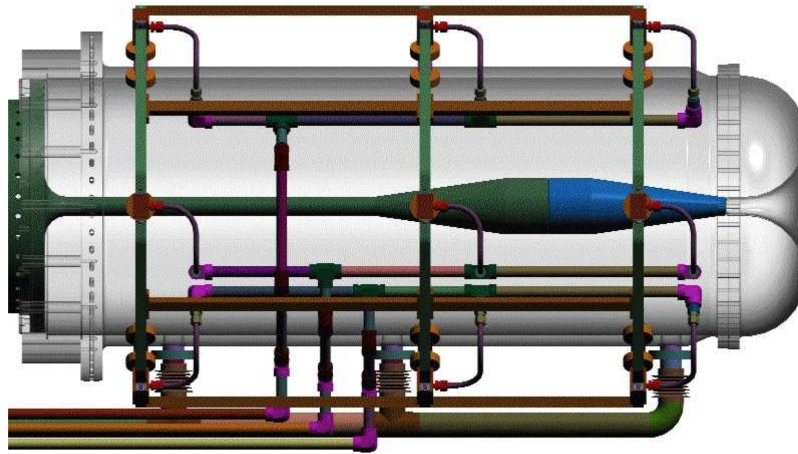


Figure 4.2: *The BNB focusing horn system. The gray outer conductor is drawn transparent for visualization purposes. The beryllium target lies within the central hollow tube axis. A current flows along the inner conductor, returning along the outer conductor.*

753 through the length of the decay region is an absorber consisting of ten removable steel
 754 plates for systematic studies, which were not used in the analyses described in this thesis.
 755 A schematic depicting the proton beam interacting with the beryllium target within the
 756 focusing horn is shown in Figure 4.3.

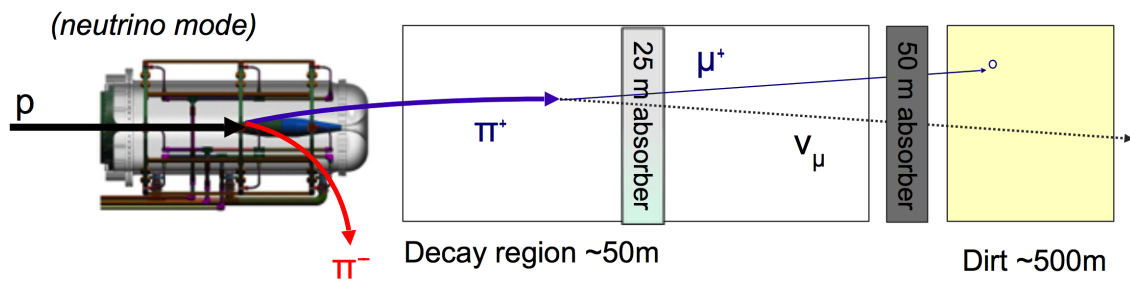


Figure 4.3: *A cartoon diagram of the incident 8.89 GeV/c proton beam (from the left) colliding with the beryllium target within the focusing horn. Shown is the current configuration for the horn referred to as “neutrino mode” in which positive charged secondaries are focused into the decay region. The 25 m absorber drawn is removable, and was not used for the analyses described in this thesis.*

757 4.2 Monte Carlo Neutrino Flux Prediction

758 The neutrino flux through MicroBooNE is determined using a Geant4 [12] Monte Carlo
 759 simulation of the beam-line, focusing horn, and decay region. The beam-line geometry
 760 modeled in Geant4 includes the position and material composition of all components of the
 761 BNB, through which the primary protons and all other particles propagate. The primary
 762 protons are simulated with the expected beam optics properties upstream of the target.
 763 The primary p-BE interactions are simulated using custom tables for the production of
 764 outgoing particles including protons, neutrons, π^\pm , K^\pm , and K^0 created from production
 765 models based on external data. The reason custom tables are used is that the variation in
 766 Geant4 hadron-production models is large.

767

768 The custom physics model using external data to simulate the production of secondary
 769 mesons in the primary p-Be interactions is described in detail in Ref [11] but will be
 770 summarized here. The custom tables describe the double differential cross section for the
 771 production of each secondary species as a function of the proton transverse and longitudinal
 772 momentum components. Existing pion and kaon production data from the HARP [13],
 773 E910 [14], and several other production experiments are used in many of the Sanford and
 774 Wang parameterization fits in the parameter space relevant to MicroBooNE [15]. The
 775 fitting parametrization is described with 9 Sanford-Wang model parameters (c_1 to c_9):

$$\frac{d^2\sigma}{dpd\Omega} = c_1 p^{c_2} \left(1 - \frac{p}{p_B - c_9} \right) \exp \left[-c_3 \frac{p^{c_4}}{p_B^{c_5}} - c_6 \theta(p - c_7 p_B \cos^{c_8} \theta) \right] \quad (4.1)$$

776 where p and θ are the momentum and angle of the outgoing secondary mesons.

777

778 Since no measurements for K^+ production exist at the 8.89 GeV/c BNB primary proton
 779 momentum, the Feynman scaling hypothesis is used to extrapolate from K^+ production
 780 measurements at different primary proton momenta. The Feynman scaling model function
 781 depends only on the transverse proton momentum p_T and the Feynman scaling factor
 782 x_F , which is the ratio of the longitudinal momentum, p_L^{CM} , to the maximum longitudinal
 783 momentum, $p_L^{CM(max)}$,

$$x_F = \frac{p_L^{CM}}{p_L^{CM(max)}}. \quad (4.2)$$

784 According to the Feynman scaling model, the invariant cross section can be written in terms
785 of seven parameters (c_1 to c_7) as

$$E \frac{d^3\sigma}{dp^3} = c_1 \exp[-c_2 p_T - c_3 |x_F|^{c_4} - c_5 p_T^2 - c_7 |p_T \dot{x}_F|^{c_6}] \quad (4.3)$$

786 While this parameterization represents the measurements well, the uncertainties used in
787 analyses by MiniBooNE were initially inflated by a factor of four to account for some in-
788 consistencies within the production data. A more recent measurement by the SciBooNE
789 collaboration indirectly measured the K^+ production in the BNB to drastically reduce this
790 uncertainty [16].

791

792 With the outgoing particle production simulated, these particles are propagated with
793 Geant4 taking into account energy loss and electromagnetic and hadronic processes, includ-
794 ing the impact of the horn magnetic field on the kinematics of those particles. A custom
795 decay model is used outside of the Geant4 framework to simulate the decay processes that
796 result in neutrinos, which includes the latest branching fraction measurements and simu-
797 lates polarization effects and kinematic distributions resulting from decay form factors. A
798 number of techniques to enhance the statistical precision of the flux are employed [11].

799

800 The systematic uncertainties in the neutrino flux production come from several sources,
801 which are summarized in Table 4.1. The dominant uncertainty is that from particle produc-
802 tion. By varying parameters in all of these systematic sources, a systematic error envelope
803 is calculated for the final neutrino flux through the MicroBooNE detector. Figure 4.4 shows
804 the ν_μ , $\bar{\nu}_\mu$, ν_e , and $\bar{\nu}_e$ flux at the MicroBooNE detector. The red bars show the systematic
805 error envelope, which includes all errors except those for proton delivery, which is a flat
806 normalization error. Table 4.2 summarizes the systematic errors for the integrated flux.

MicroBooNE BNB Flux Systematics	
Source	Description
Proton delivery	Counting the number of protons arriving on the beryllium target.
Particle production	Rate and shape of secondary particles produced in p-Be interactions.
Hadronic interactions	The rate of hadronic interactions in target or horn.
Horn magnetic field	Magnetic field to focus the outgoing charged mesons from p-Be interactions.
Beam-line geometry	Possible misalignments or displacements of beam-line components from their expected orientations.
Horn skin depth	Non-uniformity of current in the inner conductor of horn.

Table 4.1: *A summary of the systematic uncertainties included in the MicroBooNE flux prediction. The dominant uncertainty is that from particle production.*

	ν_μ	$\bar{\nu}_\mu$	ν_e	$\bar{\nu}_e$
POT Delivery	2.00%	2.00%	2.00%	2.00%
π^+	5.80%	0.46%	4.62%	2.66%
π^-	0.01%	7.51%	0.28%	3.20%
K^+	0.38%	0.13%	5.19%	2.67%
K^-	0.01%	0.35%	0.28%	3.92%
K_L^0	0.03%	0.27%	2.36%	22.59%
Other	5.78%	6.09%	3.60%	7.61%
Total	8.44%	9.89%	8.43%	24.74%

Table 4.2: *A summary of the systematic errors for the integrated flux, mostly from particle production. “Other” includes hadronic interactions, horn current uncertainty, and skin effect.*

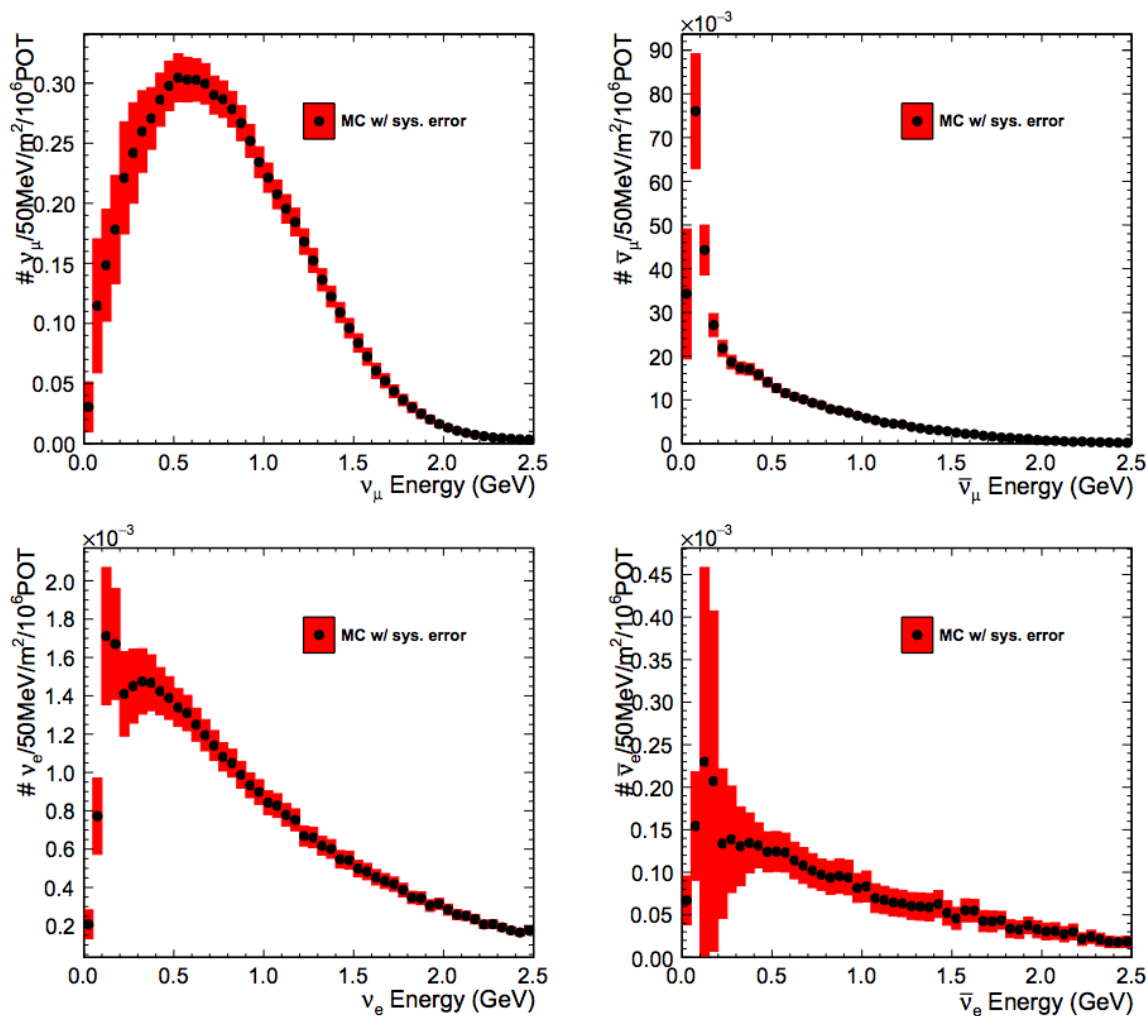


Figure 4.4: Neutrino flux prediction (black dots) with systematic error bars (red envelope) excluding proton delivery systematics which results in a flat normalization correction.

807 **Chapter 5**

808 **Low Energy Excess: LSND and**
809 **MiniBooNE**

810 **5.1 Introduction**

811 This chapter will describe the observed low energy excess reported by the MiniBooNE ex-
812 periment and the electron antineutrino excess seen by the LSND experiment. The LSND
813 experiment first observed an excess of $\bar{\nu}_e$ in a $\bar{\nu}_\mu$ beam in 2001. The MiniBooNE experi-
814 ment then observed an unexplained excess of electron-like events in a primarily ν_μ beam in
815 the neutrino energy region between 200 to 475 MeV in 2009. A description of the LSND
816 observation followed by the MiniBooNE detector and analysis is provided in this chapter.
817 The purpose of this chapter is to provide a historical motivation for the eventual sensitivity
818 studies done for the MicroBooNE experiment, which will be described in Chapter 6.

819

820 **5.2 LSND Observation**

821 In 2001, the Liquid Scintillator Neutrino Detector (LSND) collaboration published an ob-
822 servation of excess events consistent with $\bar{\nu}_e$ interactions above the expected background
823 in a $\bar{\nu}_\mu$ beam at the Los Alamos Neutron Science Center [8]. Given the $\frac{L}{E}$ ($\approx \frac{30m}{40MeV}$) for
824 this measurement, the excess disagreed with previous neutrino oscillation measurements of

the neutrino mixing angles and Δm^2 values in the three neutrino model. The LSND excess corresponded to a Δm^2 of approximately 1 eV^2 , orders of magnitude higher than previously measured values of Δm_{12}^2 and Δm_{23}^2 . One explanation for this drastically different Δm^2 value is the possible existence of potential additional “sterile” neutrino states, which must not interact weakly given that the Z- boson decay width constrains the number of weakly interacting neutrino states to three.

831

To test the LSND result, the MiniBooNE experiment was designed. It would search for ν_e interactions in a primarily ν_μ beam, with a similar $\frac{L}{E}$ ($\approx \frac{500m}{700MeV}$).

834 5.3 The MiniBooNE Experiment

835 5.3.1 The MiniBooNE Detector and Monte Carlo Simulation

The MiniBooNE detector [17] consists of a spherical detector located 541 meters downstream of the BNB neutrino production target. As shown in Figure 5.1, the detector consists of a sphere with a diameter of 12.2 meters filled with 818 tons of mineral oil located underneath more than 3 meters of earth overburden. There exists a signal region instrumented with 1280 8-inch photomultiplier tubes (PMTs), most of which were reused from the LSND experiment, and a 35 cm thick outer veto region separated by an opaque barrier instrumented with 240 PMTs. The efficiency for rejecting cosmic ray muons by using the outer veto region was measured to be 99.99%.

844

The detection method of the MiniBooNE experiment is based primarily on Cherenkov light. The mineral oil within the signal region acts as the neutrino target material. The majority of final state particles exiting neutrino interactions at neutrino energies from the BNB are produced above Cherenkov threshold. These particles produce Cherenkov light which is detected by the PMTs lining the signal region of the detector. Reconstructing the pattern of light projected onto the wall PMTs is used for particle identification.

851

The detector is calibrated with a series of *in situ* measurements, primarily with cosmic

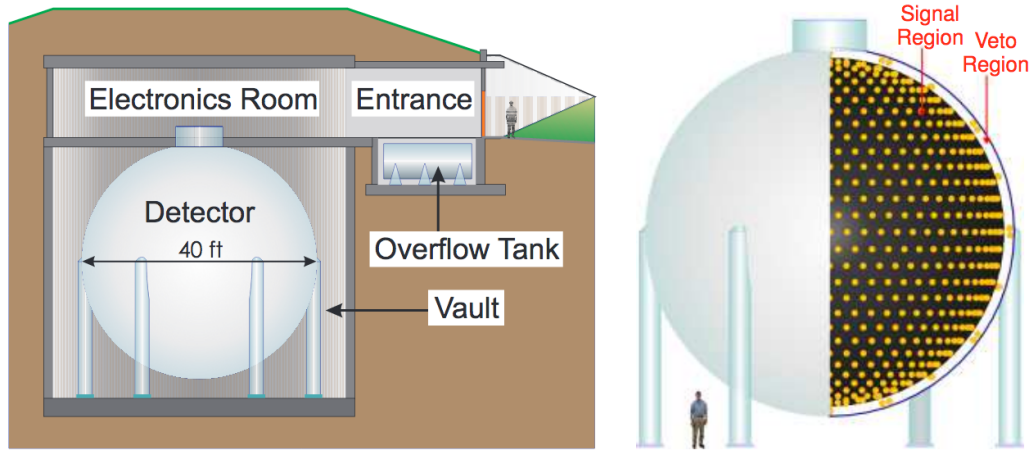


Figure 5.1: *The MiniBooNE detector enclosure (left) and a cut-away drawing (right) of the detector showing the distribution of PMT's in the signal and veto regions.*

853 ray muons. Cosmic ray muons stopping within the detector along with an external muon
 854 hodoscope provide for angular resolution measurements. Additionally, muons which stop
 855 and produce decay electrons that have a known energy endpoint of around 50 MeV provide
 856 an energy calibration source at low energies, while through-going muons provide calibration
 857 information at higher energies. Also, tagged π^0 particles which decay into two photons have
 858 a known mass of around 135 MeV and therefore provide energy calibration information in
 859 that region.

860

861 5.3.2 MiniBooNE Event Selection

862 Different final state particles exiting a neutrino interaction in the MiniBooNE signal volume
 863 create different patterns of Cherenkov light read out by the PMTs. Figure 5.2 [18] shows
 864 how these patterns differ for different common kinds of final state particles (muons, elec-
 865 trons/photons, and neutral pion decays). A muon track produces a crisp, filled-in ring of
 866 Cherenkov light, while an electron or photon produces a more fuzzy, hollow ring. A neutral
 867 pion decay will result in two photons. By reconstructing these patterns in the PMT data
 868 read out from a triggered event in MiniBooNE, the flavor and energy of the interacting
 869 neutrino can be determined up to the energy lost to particles below Cherenkov threshold.

With this kind of detection technique it is important to note that a single photon signal is indistinguishable from that of a single electron signal, a fact leading to the ultimate ambiguity of the observed low energy excess in MiniBooNE.

873

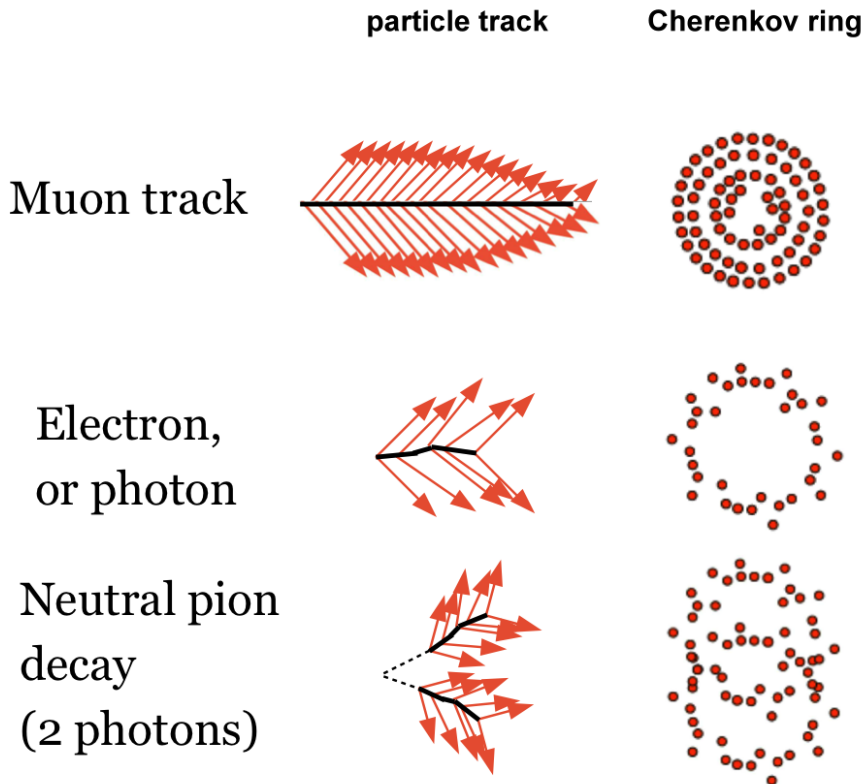


Figure 5.2: A schematic of the pattern Cherenkov light from different particles would make projected onto the inner walls of the MiniBooNE detector. Top is a muon track (a filled-in ring), middle is an electron (a fuzzy ring), bottom is a photon that pair-produces and creates two fuzzy rings.

The topology of interest in the MiniBooNE oscillation search is that of charged-current quasi-elastic (CCQE) interactions, shown in Figure 5.3. This interaction channel is the dominant one in the neutrino energy range of the BNB below 1 GeV E_ν . In a ν_l CCQE interaction (where l is the neutrino flavor), a lepton of flavor l is produced, along with a proton. The single outgoing lepton is the characteristic event signature for which Mini-

879 BooNE searches since the proton is mostly below Cherenkov threshold.

880

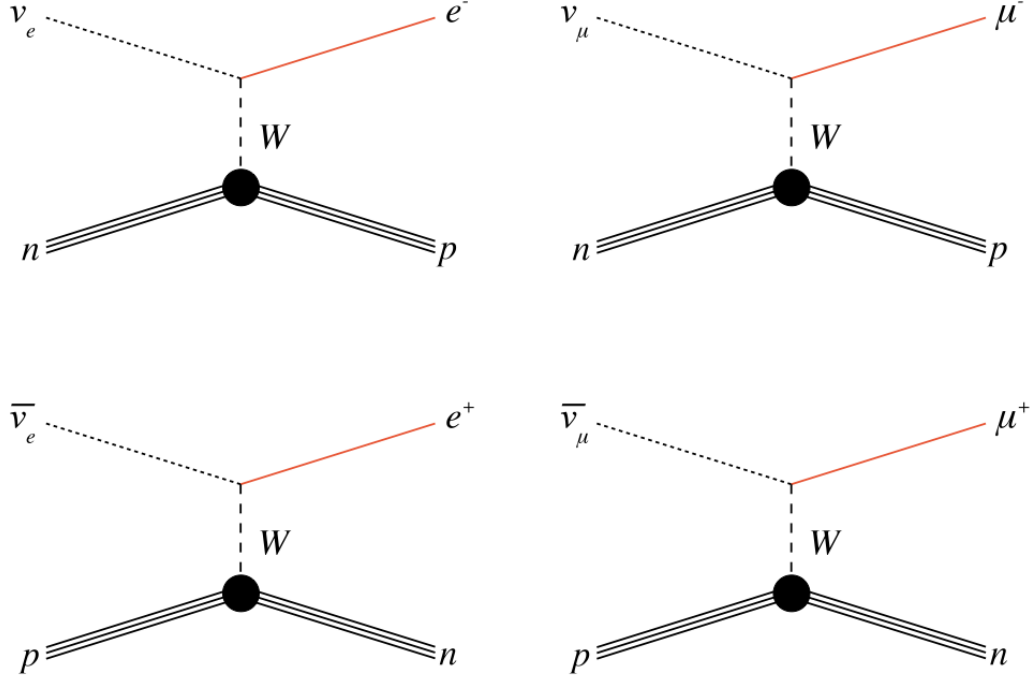


Figure 5.3: Feynman diagrams of the charged-current quasi-elastic (CCQE) interaction channel for ν_e , ν_μ , $\bar{\nu}_\mu$, and $\bar{\nu}_e$ (clockwise from the top left). ν_e CCQE is the signal channel for the MiniBooNE oscillation analysis.

881 In order to select ν_e^{CCQE} events, cuts are placed to mitigate backgrounds. The most
 882 powerful rejection comes from requiring the events occur within the beam timing window.
 883 The beam arrives at the detector at a rate of 5 Hz, and each spill lasts $1.6 \mu s$ and is com-
 884 posed of approximately 80 buckets separated by 19 ns . Given the time scale with which
 885 MiniBooNE measures the light from interactions, cuts on event timing alone reduces non-
 886 beam backgrounds to $\sim 10^{-3}$. Additional cuts require that there is significant activity in
 887 the signal volume and little activity in the outer veto volume, a signature characteristic of
 888 beam related neutrino events. These pre-cuts achieve more than a 99.99% rejection of beam
 889 unrelated backgrounds. The efficiency to select ν_e^{CCQE} events in MiniBooNE depends on
 890 which cuts are applied in the analysis, but varies between 55% (with a purity of 36.8%) and
 891 26.6% (with a purity of 77.0%)[19]. The efficiency to select ν_e^{CCQE} events also depends on

892 which cuts are applied but varies between 55.2% and 30.6%[20].

893

894 In order to reconstruct events, MiniBooNE uses a maximum likelihood fitting algorithm
 895 leveraging properties of charged particle tracks and showers inferred from measured charges
 896 and times on the PMTs. The likelihoods associated with different event hypotheses are used
 897 to classify each event as a signal ν_e CCQE event, or as a background process like ν_μ CCQE
 898 and NC π^0 production. Note that MiniBooNE cannot differentiate between a μ^+ and a μ^- ,
 899 or e^+ and e^- so discrimination between neutrino and antineutrino on an event-by-event
 900 basis is not possible. MiniBooNE also uses the identified ν_μ^{CCQE} events to constrain the
 901 intrinsic ν_e background from muon decay and the measured NC π^0 , two-gamma rate to
 902 constrain the predicted single shower NC π^0 backgrounds.

903

904 Assuming CCQE kinematics, the incident neutrino energy is reconstructed with knowl-
 905 edge of the outgoing lepton energy (E_l) and scattering angle (θ_l). In MiniBooNE specifically,
 906 the struck nucleon is assumed to be at rest, so the incident neutrino energy E_ν^{CCQE} is given
 907 by:

$$E_\nu^{CCQE} = \frac{2m_n E_l + m_p^2 - m_n^2 - m_l^2}{2(m_n - E_l + \cos \theta_l \sqrt{E_l^2 - m_l^2})} \quad (5.1)$$

908 where m_n , m_p , m_l are the masses of the neutron, proton, and lepton respectively, and θ_l
 909 is the scattering angle of the outgoing lepton with respect to the (known) beam neutrino
 910 direction.

911

912 5.3.3 MiniBooNE Results

913 With the described reconstruction methods and energy definition, the MiniBooNE published
 914 results [21] for the ν_e appearance search in neutrino mode running are shown in Figure 5.4.
 915 Note that besides the irreducible intrinsic ν_e backgrounds, the dominant background in the
 916 excess region is π^0 mis-identification (MID) (red). In a π^0 MID event event, a π^0 is created
 917 in the neutrino interaction and its subsequent immediate decay into two photons can mimic
 918 the ν_e^{CCQE} signature if either one of the photons escapes the detector or the Cherenkov

919 rings from the two photons overlap to become one ring. Another important background is
 920 $\Delta \rightarrow N\gamma$ (brown). Recall that both of these backgrounds arise from MiniBooNE's inability
 921 to distinguish electrons from photons, an important ambiguity which will be discussed in
 922 more detail in the following sections.

923

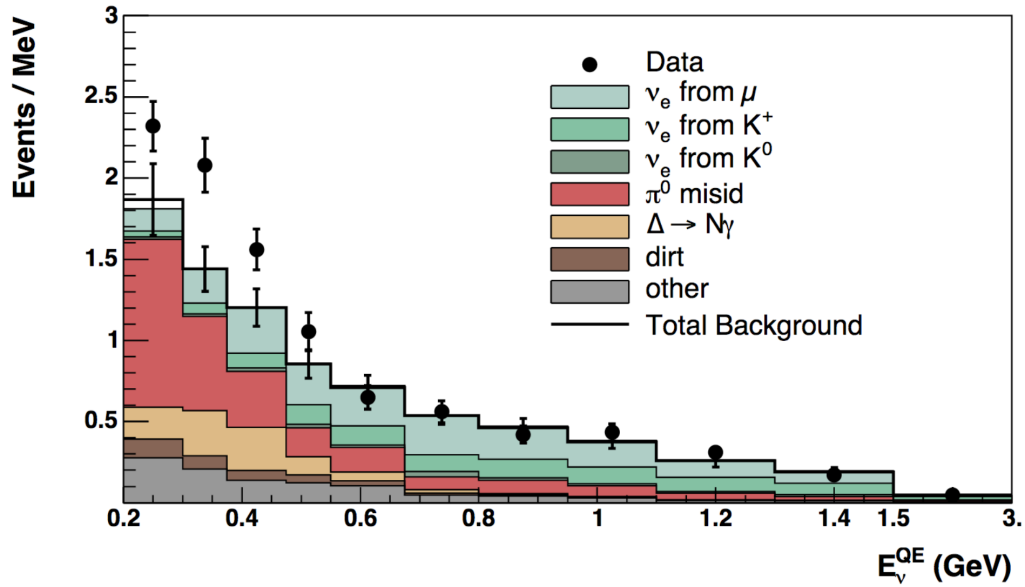


Figure 5.4: The E_{ν}^{QE} distribution for MiniBooNE data (points with statistical errors) and and backgrounds (histogram with systematic errors).

924 As shown in Figure 5.4, in the energy region $E_{\nu}^{QE} > 475$ MeV there is good agreement
 925 between data and background prediction, making a two neutrino oscillation fit inconsistent
 926 with the LSND results at the 98% confidence level assuming CP conservation. Meanwhile,
 927 below E_{ν}^{CCQE} of 475 MeV there is a statistically significant (6σ , reduced to 3σ after sys-
 928 tematics) excess. The excess of 129 ± 43 events (stat+syst) is consistent in magnitude with
 929 the LSND oscillation excess.

930

931 In a later separate antineutrino run (in which the BNB horn current is switched to pro-
 932 duce a primarily $\bar{\nu}_{\mu}$ beam), an excess was observed in the energy region $E_{\nu}^{QE} > 475$ MeV
 933 that was consistent with an LSND-type two neutrino oscillation over the null oscillation

hypothesis at the 91% confidence level. In the lower energy region $E_\nu^{QE} < 475$ MeV, an excess of 38.6 ± 18.5 events was observed. In a fit to the full energy range $E_\nu^{QE} > 200$ MeV, the excess was consistent with an LSND-type two neutrino oscillation over the null oscillation hypothesis at the 98% confidence level.

938

939 5.3.4 Proposed Low Energy Excess Sources

940 Shown in Figure 5.5 is the MiniBooNE neutrino mode excess (data - expected background)
 941 with oscillation fits with parameters constrained to be in the LSND allowed region. The
 942 parameters in the LSND allowed region are ruled out at the 95% confidence level if the data
 943 are fit with $E_\nu^{CCQE} > 475$ MeV.

944

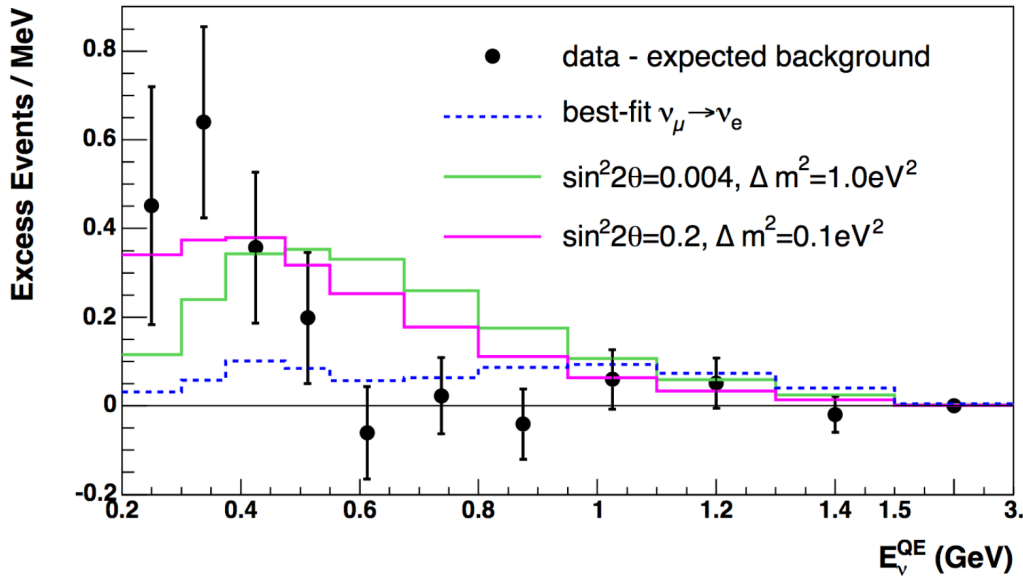


Figure 5.5: The MiniBooNE event excess as a function of E_ν^{QE} . Also shown are the expectations from the best oscillation fit and from neutrino oscillation parameters in the LSND allowed region. The error bars include both statistical and systematic errors.

945 Given MiniBooNE's inability to distinguish electrons from photons, the origin of this
 946 excess is either a mis-estimation of one of the backgrounds, or some sort of new physics.

947 The former is unlikely the case because MiniBooNE makes many *in situ* measurements that
 948 allow for the constraining of these backgrounds. The neutral current induced backgrounds
 949 (NC π^0 , $\Delta \rightarrow N\gamma$, and dirt) are constrained by such measurements. Measurements con-
 950 straining these backgrounds are described in more detail in the following paragraphs.

951

952 The NC π^0 rate in MiniBooNE is measured by selecting events with reconstructed mass
 953 near the π^0 mass. This obtains a $> 90\%$ pure sample of NC π^0 interactions which is
 954 compared to simulation to obtain a correction function in order to bring the simulated dis-
 955 tribution in agreement with data. This same correction function is applied to NC π^0 events
 956 that are backgrounds in the ν_e appearance analysis. This correction function increases the
 957 NC π^0 background by less than 13% for $E_\nu^{CCQE} < 400$ MeV and decreases the background
 958 by as much as 20% above this neutrino energy region. Including this correction factor, the
 959 uncertainty on the overall NC π^0 backgrounds is 7%. Note that a correction factor of 2.0
 960 would be required to explain the origin of the excess as originating from a mis-estimated
 961 NC π^0 background [18].

962

963 The excess is unlikely caused by a mis-estimation of the $\Delta \rightarrow N\gamma$ backgrounds because
 964 they are additionally constrained by the NC π^0 measurement through the relative rate of
 965 resonant production times a branching fraction of $(0.56 \pm 0.04)\%$. With this measurement,
 966 the uncertainty on the $\Delta \rightarrow N\gamma$ backgrounds is 12%. Note that a (very large) correction
 967 factor of 2.7 would be required to explain the origin of the excess as originating from a
 968 mis-estimated $\Delta \rightarrow N\gamma$ background.

969

970 The excess is unlikely caused by a mis-estimation of the dirt backgrounds because a di-
 971 rect measurement is made by selecting a separate event sample which are likely dirt events
 972 and comparing data to simulation. These events are reconstructed close to the detector
 973 boundaries with direction pointed generally inwards since this is a background from events
 974 produced outside of the detector. In neutrino mode, a dirt background normalization cor-
 975 rection factor was computed to be 0.7 ± 0.1 (with simulation over-predicting the dirt rate
 976 normalization). Given the power of the event selection cuts designed to mitigate dirt back-

977 grounds, the relevance of this relatively large correction factor is minimal.

978

979 The charged current induced backgrounds (intrinsic ν_e^{CCQE}) are reduced with *in situ*
 980 measurements of ν_μ CCQE interactions. A data to simulation comparison of measured
 981 ν_μ CCQE interactions allows for the retuning of underlying flux and cross section parame-
 982 ters in order to bring simulated distributions in agreement with data. These parameters are
 983 the same as those used to predict the ν_e^{CCQE} rate and shape. In addition, a measurement
 984 of the highest energy ν_μ CCQE interactions allows for the further constraint of ν_e^{CCQE} from
 985 kaon decay backgrounds, which is discussed in more detail in a later section of this thesis.

986

987 Given the likelihood that the excess is not caused by misidentified backgrounds, several
 988 new-physics interpretations have been proposed in attempt to explain the excess, including
 989 sterile neutrino oscillations (with one, two, or more sterile neutrinos), and new interactions
 990 both within and outside of the standard model (CPT violation, quantum decoherence, sterile
 991 neutrino decay, etc). A summary of these interpretations can be found in [22]. A commonal-
 992 ity between all interpretations is that their interactions pass the MiniBooNE event selection
 993 cuts; that is, they have one electron or one photon exiting the interaction vertex.

994

995 5.4 Conclusions

996 This chapter has presented the historical background of the “low energy excess” observed
 997 by the MiniBooNE experiment published in 2009 that was in response to the oscillation
 998 signal reported by the LSND experiment in 2001. Possible sources for this excess have
 999 been discussed, such as mis-estimated backgrounds and sterile neutrinos. Ultimately the
 1000 excess as seen by MiniBooNE can be attributed to an excess of either electron-like events
 1001 or photon-like events. Determining which it is is beyond the capabilities of MiniBooNE due
 1002 to limitations of its detector technology (a Cherenkov ring imaging detector). Because of
 1003 this limitation, the MicroBooNE experiment was proposed in 2007 [23]. MicroBooNE was
 1004 proposed to use the same neutrino beam in a similar location as MiniBooNE, but using

1005 a different detector technology with electron/photon separation powers (liquid argon time
1006 projection chambers) to search for and clarify the ambiguity in the low-energy excess. The
1007 detailed analysis aimed to quantify the sensitivity to a specifically electron-like MiniBoone
1008 excess in the MicroBooNE detector is the subject of the next chapter of this thesis.

1009 **Chapter 6**

1010 **Low Energy Excess: MicroBooNE**

1011 This chapter will describe the MicroBooNE sensitivity study to observe the same excess
1012 as observed by MiniBooNE, in the same neutrino beam-line but with a different detector
1013 technology. The description of the analysis covers the signal modeling based on the Mini-
1014 BooNE published data releases, the event selection, and background mitigation techniques
1015 employed. Ultimately, the expected sensitivity to measure such a signal is calculated.

1016 **6.1 MicroBooNE In The Context of the Low Energy Excess**

1017 Given that the proposed explanations for the origin of the measured MiniBooNE low energy
1018 excess in neutrino mode all predict either a single electron or single photon produced at
1019 the neutrino interaction vertex, and that MiniBooNE cannot discriminate between single
1020 electrons or photons, the MicroBooNE experiment was proposed in 2007. This detector
1021 (described in detail in Chapter 3) is a liquid argon time projection chamber, a relatively
1022 new detector technology which allows for the discrimination between single electrons and
1023 photons. MicroBooNE runs in the same beam line (BNB) in neutrino mode and is physi-
1024 cally located close to MiniBooNE; the MicroBooNE detector is located 470 m from the BNB
1025 production target, while the center of the MiniBooNE detector is 541 m from the BNB pro-
1026 duction target. Therefore, MicroBooNE should be able to elucidate the MiniBooNE low
1027 energy excess ambiguity, first by seeing if an excess exists and then by determining if the
1028 excess is related to an excess of photon events or electron events.

1029

1030 The electron/photon discrimination power of a LArTPC is based on the energy deposi-
 1031 tion at the start of electron and photon showers; photons will pair produce and in general
 1032 have twice the ionization as a single electron. Shown in Figure 6.1 is the energy loss per unit
 1033 length along the first 2.4 cm of simulated single electron showers (red) and single photon
 1034 showers (black) in terms of minimally ionizing particle (MIP) energy in liquid argon (about
 1035 2.1 MeV/cm). Leveraging the dE/dx difference between electrons and photons, and addi-
 1036 tionally the presence of a several centimeter (on average) gap between a photon's creation
 1037 point at the neutrino event vertex and its pair production, MicroBooNE has very powerful
 1038 electron/photon separation power whereas MiniBooNE has none.

1039

1040 There are other important differences between the MiniBooNE detector and that of
 1041 MicroBooNE which need to be considered when broaching the subject of estimating a sen-
 1042 sitivity of a signal seen in MiniBooNE as it might be seen in MicroBooNE. These differences
 1043 are summarized in Table 6.1. From the table it is clear that the event selection efficiency
 1044 in MicroBooNE (not yet completely determined, but discussed in Section 6.4.3) will have
 1045 to be much higher than that of MiniBooNE for the two experiments to have comparable
 1046 statistical significances, since MicroBooNE is ten times smaller than MiniBooNE.

1047 6.1.1 Past Sensitivity Studies

1048 The initial attempt to scale the MiniBooNE backgrounds and excess to MicroBooNE is
 1049 shown in Figure 6.2, both under the assumption that the excess is due to an electron-like
 1050 event (left) or due to a photon-like event (right) [24]. Performing such a scaling analysis is
 1051 a subtle and difficult task because of the drastic differences between the MiniBooNE and
 1052 MicroBooNE detectors, as described in the previous section.

1053

1054 This scaling assumes the electron/photon misidentification rate in MicroBooNE is 6%
 1055 (whereas it is 100% for MiniBooNE). Also, event selection efficiencies in MicroBooNE are
 1056 assumed to be exactly twice that of MiniBooNE because of the detector technology. This
 1057 scaling procedure ignores other potentially important differences between MicroBooNE and

MiniBooNE Compared to MicroBooNE		
	MiniBooNE	MicroBooNE
Detector Technology	Cherenkov	LArTPC
Nominal POT	6.46×10^{20}	6.6×10^{20}
Active Volume Mass	818 Tons	89 Tons
Signal Selection Efficiency	25%	N/A
Readout Time Scale	nanoseconds	milliseconds
Distance from Neutrino Production Target	541 m	470 m
Target Material	CH_2	Argon
e \rightarrow γ Separation Power	None	High
Sensitive to Vertex Activity	No	Yes

Table 6.1: *A comparison of some of the important similarities and differences between the MiniBooNE detector and the MicroBooNE detector, which make the signal modeling in this sensitivity study difficult.*

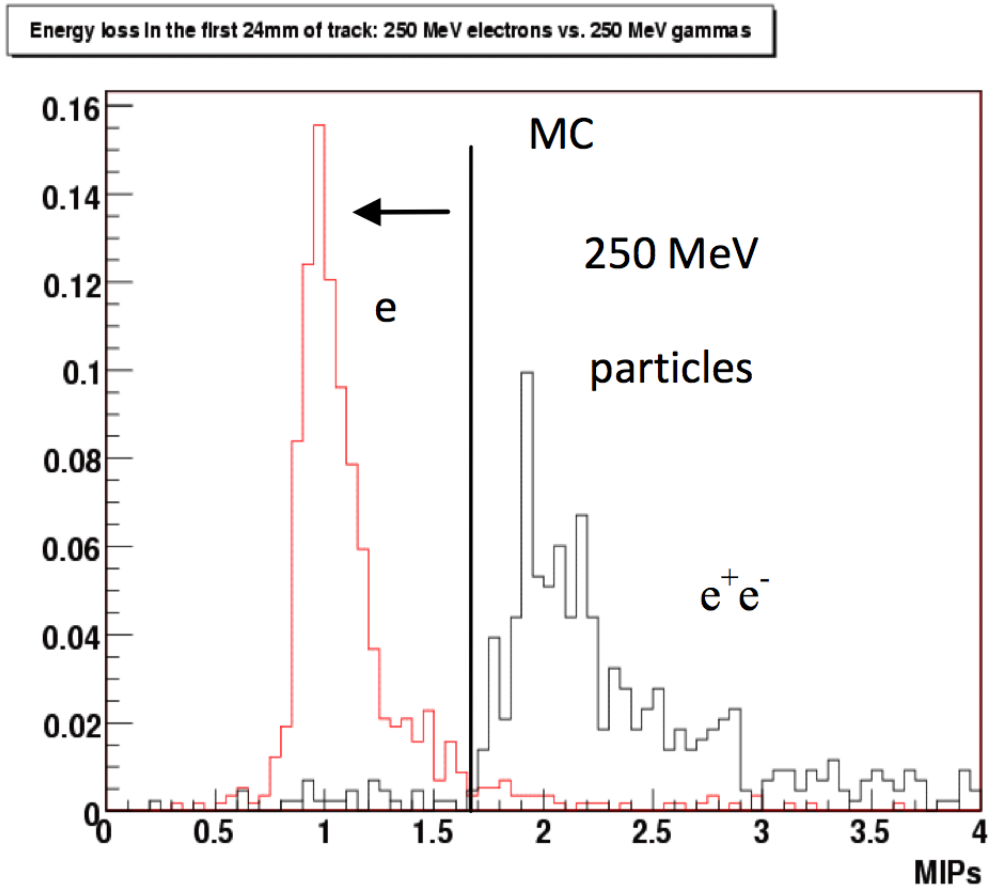


Figure 6.1: *Energy loss per unit length along the first 2.4 cm of simulated single electron showers (red) and single photon showers (black) in terms of minimally ionizing particle (MIP) energy in liquid argon (about 2.1 MeV/cm). Photons in general have twice the dE/dx of electrons at the start of their showers, stemming from pair production.*

1058 MiniBooNE including differences in detector geometry (important for π^0 mis-identifications
 1059 in which one photon escapes), flux differences (the relative rates are roughly 25% different
 1060 because of the baseline differences of the two detectors), event topology selection differ-
 1061 ences (MicroBooNE can see much more vertex activity than can MiniBooNE, especially
 1062 when additional final state particles are below Cherenkov threshold), the differing cosmic
 1063 rejection background efficiencies (MiniBooNE can reject cosmics more efficiently than Mi-
 1064 croBooNE because of their outer veto and because of the differing detection timescales

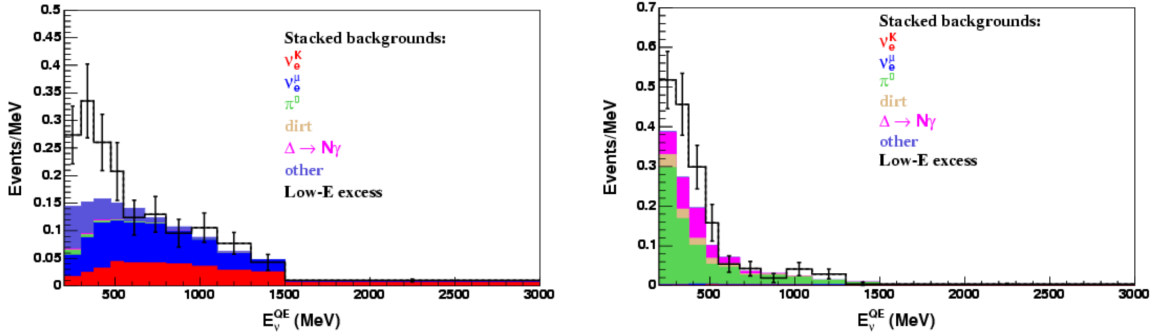


Figure 6.2: The results of the first analysis to scale the MiniBooNE backgrounds and excess to MicroBoone both under the assumption that the excess is due to an electron-like event (left) or under a photon-like event (right). Stacked histograms show the expected background. Error bars indicate statistical uncertainty. The number of signal events, scaled from MiniBooNE for neutrino flux and fiducial volume, is the same in both plots (though dedicate electron-specific and photon-specific event selection cuts may show this to be unrealistic). Both plots assume 6.6×10^{20} POT for the MicroBoone 60 ton fiducial mass.

of Cherenkov technology, ns , compared to that of LArTPCs, ms), cross section differences between argon and CH_2 arising from differing proton to neutron ratios, among other things.

1067

1068 The resulting statistical significance from the aforementioned scaling (previous Ref. [24])
 1069 after the nominal amount of data is taken in MicroBoone (6.6×10^{20} POT) is computed
 1070 to be 5.7σ under the single-electron excess hypothesis and 4.1σ under the single-photon
 1071 hypothesis.

1072

1073 The described scaling analysis is a very valuable tool, but is fraught with many question-
 1074 able assumptions. The next sections in this thesis describe a more rigorous analysis with
 1075 the ultimate goal of computing MicroBoone's sensitivity to the MiniBoone low energy
 1076 excess assuming specifically the single-electron hypothesis. In this analysis, actual signal
 1077 and background events will be simulated in the MicroBoone detector and event selection
 1078 cuts and algorithms will be used to select them.

1079 **6.2 Monte Carlo Simulation**

1080 **6.2.1 Simulated Background Samples**

1081 In this thesis analysis, both beam induced backgrounds and beam external backgrounds
1082 are simulated in the MicroBooNE cryostat. For beam-induced samples, the same flux
1083 predictions are used as were used in the MiniBooNE simulations (accounting for baseline
1084 and acceptance differences). The beam-induced samples come from full simulated BNB
1085 interactions with cross sections provided by GENIE [25]¹. Non-beam samples (cosmics)
1086 come from simulated CORSIKA generated [27] cosmic rays that pass through the cryostat.
1087 Cosmic rays passing through other portions of the detector hall but not the cryostat result
1088 in negligible backgrounds in this ν_e search. The passage of all particles through the detector
1089 volume is simulated by the GEANT4 package [12].

1090 **6.2.2 Reconstruction**

1091 In general, the output of an automated reconstruction chain in a LArTPC consists of recon-
1092 structed optical hits which come from the PMT signals, and reconstructed wire hits which
1093 come from drift electron ionization signals on the induction and collection plane wires. Re-
1094 construction algorithms cluster the electron ionization hits on each wire plane into those
1095 corresponding to individual particles, then match clusters from different wire planes to form
1096 3D reconstructed objects. The wire planes provide two of the three dimensions, and match-
1097 ing clusters to the timing of optical hits on the PMTs provide the third (drift) dimension.
1098 These reconstructed objects are either thin, straight tracks (which come from particles like
1099 muons, charged pions, and protons) or more fuzzy cone-shaped showers, which come from
1100 higher energy electrons or photons. Ideally this analysis would be done using these recon-
1101 structed objects. In this way, the same event selection methods could be used on data as
1102 are used in simulation. While automatic track reconstruction can currently be performed

¹Note that while MicroBooNE uses GENIE to simulate BNB interactions, MiniBooNE used NUANCE [26]. Given the approach to determine the absolute normalization of the MiniBooNE excess as seen in MicroBooNE based on intrinsic ν_e rates (see Section 6.5), differences between these two generators can be ignored.

1103 at an adequate level, the difficulties involved in shower reconstruction (which is particularly
1104 important to tag and study ν_e^{CC} events) have yet to be overcome by MicroBooNE and
1105 the LArTPC community. Currently, the MicroBooNE collaboration is moving to use the
1106 methods and algorithms of the analysis presented here to do a sensitivity estimate using
1107 reconstructed objects.

1108

1109 For these reasons, this simulation-only study is done with objects that are not auto-
1110 matically reconstructed from wire and PMT signals, but instead from truth-based energy
1111 depositions in the detector. In general, these objects represent what would be reconstructed
1112 from wire and PMT signals if the reconstruction algorithms performed perfectly. Therefore,
1113 this is referred to as “perfect reconstruction” and the details of these objects are discussed
1114 in the next section.

1115 6.2.2.1 “Perfect Reconstruction”

1116 While a simulation-only study using real automated reconstruction would be ideal, such
1117 a study using “perfect reconstruction” is incredibly valuable as an initial estimate of the
1118 MicroBooNE sensitivity; it is a step forward from the aforementioned scaling study (Section
1119 6.1.1), and the event selection cuts and algorithms designed in this study can be used out-of-
1120 the-box on automated reconstructed objects once they become available. Additionally, the
1121 “perfect reconstruction” can be tuned to more realistically represent what automated recon-
1122 struction might be capable of, for example by smearing the energy of objects or emulating
1123 realistic reconstruction efficiencies. This provides the important estimate of uncertainties
1124 arising from the imperfect automated reconstruction.

1125

1126 As mentioned earlier, the final 3D reconstructed objects formed from wire plane signals
1127 and PMT signals are referred to as tracks or showers. Tracks are close to straight lines in
1128 three dimensions, while showers are fuzzier and generally cone-shaped in three dimensions.
1129 The “perfect reconstruction” analogs to tracks and showers are referred to as MCTRACKS
1130 and MCSHOWERS. They are created from simulated GEANT4 3D energy depositions in
1131 the detector volume. GEANT4 outputs 3D energy depositions in the detector, along with

truth information about which parent particles deposited this energy. MCSHOWERS and MCTRACKS are 3D objects which are formed by grouping energy depositions based on parent particles. Whether a particle in GEANT4 becomes an MCSHOWER or an MCTRACK is based on truth particle identity. For example, electrons always form MCSHOWERS² and muons always form MCTRACKS. All of the energy deposited by particles *within the TPC* is used to form these “perfect reconstructed” objects, which is in line with them representing actual reconstructible quantities (no ionization outside of the TPC is reconstructible).

1139

MCTRACKS consist of a series of ordered 3D trajectory points, each corresponding to an energy deposition in the detector. MCSHOWERS have the following attributes: 3D start point where the first energy from the parent particle is deposited, 3D direction which is computed by fitting a line in 3D to all of the deposited energy from the parent particle, and dE/dx computed from the energy depositions along the first few centimeters of the shower. These “perfectly reconstructed” tracks and showers (MCTRACKS and MCSHOWERS) serve as the input to the event selection algorithms, just as automated reconstructed tracks and showers (with the same attributes) would in real data.

1148

6.3 Event Selection

This section describes the algorithms and cuts used to identify ν_e^{CC} interactions, given as input the “perfect reconstructed” MCTRACKS and MCSHOWERS from simulated triggered events in MicroBooNE³. Note that while the initial event selection algorithms are designed to identify ν_e^{CC} inclusive interactions (which may involve pions in the final state, for example), ultimately only the ν_e^{CCQE} events (with only one electron and protons in the final state) are used in the final sensitivity estimates.

²Despite the fact that electrons behave more like tracks below the critical energy, which is on the order of 40 MeV in liquid argon.

³Note that these cuts and algorithms could use automatically reconstructed tracks and showers, and therefore could be run both on simulation and data, if the quality of track and shower reconstruction was high enough.

1156

1157 To select ν_e^{CC} interactions in MicroBooNE, a series of nine algorithms are run, each with
 1158 a specific goal in mind; they either identify background topologies in order to remove them,
 1159 or they identify the signal ν_e^{CC} topology. For example, one algorithm identifies MCSHOW-
 1160 ERS which are likely delta rays originating from tracks. Once identified, these MCSHOWERS
 1161 are no longer candidate ν_e^{CCQE} electrons. Another algorithm identifies pairs of showers that
 1162 are likely from π^0 decays (by using the dE/dx of those showers to identify them as photons,
 1163 and requiring they back-project to a common origin) in order to remove them from the
 1164 pool of candidate ν_e^{CC} electrons. Another algorithm tags through-going tracks as cosmic in
 1165 origin, ensuring they will not be associated with a beam neutrino interaction.

1166

1167 The two most important event selection algorithms for this analysis are named “Algo-
 1168 EMPart” (which handles the electron/photon discrimination) and “AlgoSingleE” (which
 1169 is the algorithm responsible for locating the ν_e^{CC} topology and associating all tracks and
 1170 showers together for eventual energy reconstruction and analysis). These two algorithms are
 1171 discussed in detail in the following two subsections. At the end of the chain of event selection
 1172 algorithms, a sample of candidate ν_e^{CC} events is obtained. These events are the subject to
 1173 further cuts both to mitigate some backgrounds that the event selection algorithms missed,
 1174 and more importantly to pick specifically ν_e^{CCQE} events. This down-sampling is necessary
 1175 to make the eventual comparison to the MiniBooNE excess, since MiniBooNE searched
 1176 exclusively for ν_e^{CCQE} events, not ν_e^{CC} inclusive.

1177 6.3.1 Electron/Photon Separation Algorithm

1178 Electron/photon separation based on dE/dx at the start of showers is done through an
 1179 algorithm called “AlgoEMPart”. This algorithm uses trained likelihood distributions which
 1180 input dE/dx and return the likelihood that the shower is electron-like, or photon-like. If a
 1181 conversion distance (the distance between the reconstructed neutrino event vertex and the
 1182 first energy deposition of the shower) is known, it will incorporate that into its likelihood as
 1183 well. This additional handle is powerful because in general an electron shower will have a
 1184 near-zero conversion distance, while a photon shower will often have a conversion distance

of several centimeters. The algorithm’s likelihood is configured with parameters output by a RooFit [28] minimization routine. The RooFit routine is trained on simulated single electron and single photon MCSHOWERS. In general, this algorithm computes both the likelihood that an MCSHOWER is an electron and that it is a photon, and determines the identity of the particle to be the one with the larger likelihood.

1190

There are two likelihood functions that may be used. If a shower can independently be associated with a neutrino interaction vertex, the algorithm will use a 2D likelihood function that includes both dE/dx and conversion length information. If an algorithm cannot associate a vertex with a shower, there is a 1D likelihood function that can be used with only dE/dx information. The 1D likelihood function is composed of a Gaussian plus a landau distribution for dE/dx , which are combined to better parameterize the dE/dx distribution, and the 2D likelihood function also includes an exponential function for conversion length. Any potential energy dependence on dE/dx or conversion distance is not included in these likelihoods. The twelve trained input parameters include mean and sigma values for the Gaussian distributions, the most probable value (MPV) and sigma values for the landau distributions, the fractional area difference between the Gaussian and landau distributions (“frac”), and the conversion length parameter (six parameters for electrons, six parameters for photons). When training, input parameters for each sample (electron, photon) are the MCSHOWER computed dE/dx as well as the truth-level creation vertex of the particle. The training results on “perfect reconstruction” electron and photon showers are shown in Figure 6.3.

6.3.1.1 Performance

The performance of this algorithm on “perfect reconstruction” is computed by using samples of single electron showers and single photon showers generated isotropically between 0.05 and 2 GeV, and selecting those events where greater than 90% of the shower’s energy is contained within the TPC. The algorithm’s likelihood is trained using this sample (integrated over the full energy range of the showers). The efficiency to tag electrons and photons both with the 1D and the 2D likelihood are enumerated below. Note that there are

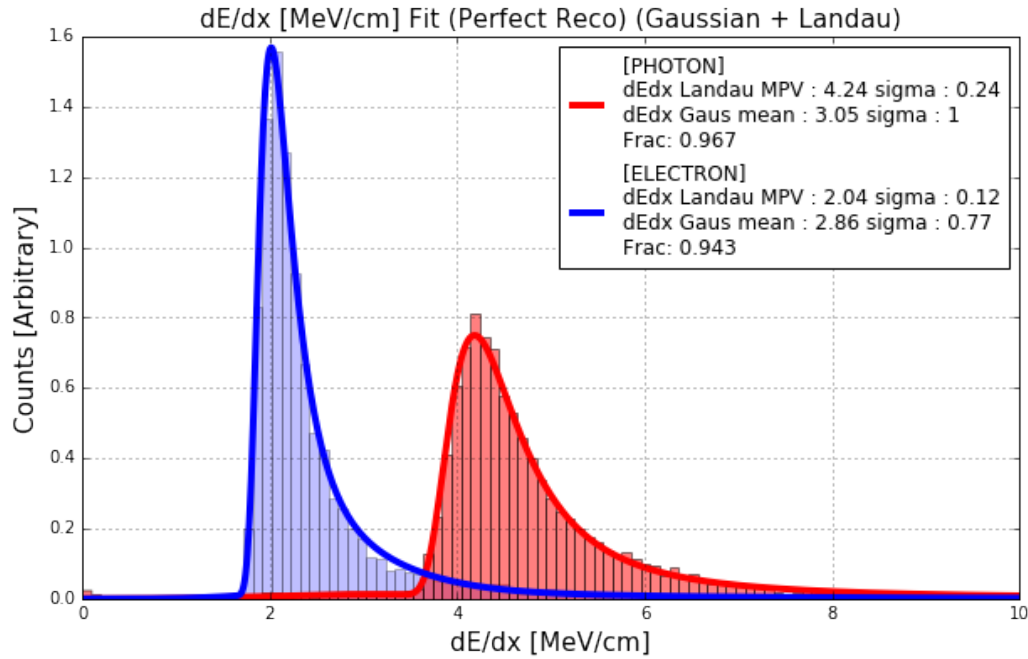


Figure 6.3: *AlgoEMPart* training results on perfect reconstructed electron showers and on perfect reconstructed photon showers as described in Section 6.3.1.1: 1D landau + Gaussian fit to dE/dx . “Frac” in the legend is the relative normalization between the landau and Gaussian fits; that “Frac” is close to one means the landau fit dominates.

1214 additional handles to identify photons which are part of a π^0 decay which are not included
 1215 in the efficiencies below (which are for single electrons or single photons only).

- 1216 1. Using *only* dE/dx information, the efficiency (over all energies) to select a single
 1217 electron is 93%, while the MID efficiency to tag the electron as a photon is 7%.
- 1218 2. Using *only* dE/dx information, the efficiency to select a single photon is 97.3%, while
 1219 the MID efficiency to tag the photon as an electron is 2.7%.
- 1220 3. Using *both* dE/dx and radiation length information (using the true creation point of
 1221 photons), the efficiency to select a single electron is 99.7%, while the MID efficiency
 1222 to tag the electron as a photon is 0.3%.
- 1223 4. Using *both* dE/dx and radiation length information (using the true creation point of
 1224 photons), the efficiency to select a single photon is 98.1%, while the MID efficiency to

1225 tag the photon as an electron is 1.9%.

1226 The 1D likelihood to determine if a shower is electron-like or photon-like is shown in
 1227 Figure 6.4. The likelihood that a shower with a given dE/dx is electron-like is computed
 1228 by the ratio of the 1D electron-like probability distribution function (PDF) value for that
 1229 dE/dx (shown non-normalized in Figure 6.3) to the sum of the electron-like PDF value for
 1230 that dE/dx and the photon-like PDF value for that dE/dx (shown non-normalized in Figure
 1231 6.3 as well),

$$L_e = \frac{e_{dE/dx}^{PDF}(\frac{dE}{dx})}{e_{dE/dx}^{PDF}(\frac{dE}{dx}) + g_{dE/dx}^{PDF}(\frac{dE}{dx})} \quad (6.1)$$

1232 where $e_{dE/dx}^{PDF}(\frac{dE}{dx})$ represents the electron dE/dx PDF function (shown non-normalized in
 1233 Figure 6.3) evaluated at a dE/dx value $\frac{dE}{dx}$ and $g_{dE/dx}^{PDF}(\frac{dE}{dx})$ represents the photon dE/dx
 1234 PDF function (also shown non-normalized in Figure 6.3) evaluated at a dE/dx value $\frac{dE}{dx}$.
 1235 The likelihood that a shower with a given dE/dx is photon-like is similarly computed but
 1236 with the photon-like PDF value for that dE/dx in the numerator.

1237

1238 The 2D likelihood including both dE/dx and conversion distance is shown in Figure 6.5.
 1239 The likelihood that a shower with a given dE/dx value, $\frac{dE}{dx}$ and a given conversion distance
 1240 value, d is electron-like is computed as follows:

$$L_e = \frac{e_{dE/dx}^{PDF}(\frac{dE}{dx}) * e_{conv}^{PDF}(d)}{g_{dE/dx}^{PDF}(\frac{dE}{dx}) * g_{conv}^{PDF}(d)} \quad (6.2)$$

1241 where $e_{dE/dx}^{PDF}(\frac{dE}{dx})$ represents the electron dE/dx PDF function (shown non-normalized in
 1242 Figure 6.3) evaluated at a dE/dx value, $\frac{dE}{dx}$, $e_{conv}^{PDF}(d)$ represents the electron conversion
 1243 distance PDF function (shown non-normalized in Figure 6.6, noting that the electron con-
 1244 version distance is effectively zero so the exponential fits the distribution relatively poorly)
 1245 evaluated at a conversion distance value, d , $g_{dE/dx}^{PDF}(\frac{dE}{dx})$ represents the photon dE/dx PDF
 1246 function (shown non-normalized in Figure 6.3) evaluated at a dE/dx value, $\frac{dE}{dx}$, $g_{conv}^{PDF}(d)$
 1247 represents the photon conversion distance PDF function (shown non-normalized in Figure
 1248 6.7) evaluated at a conversion distance value, d . The likelihood that the same shower is

¹²⁴⁹ photon-like is simply the inverse of Equation 6.2.

¹²⁵⁰

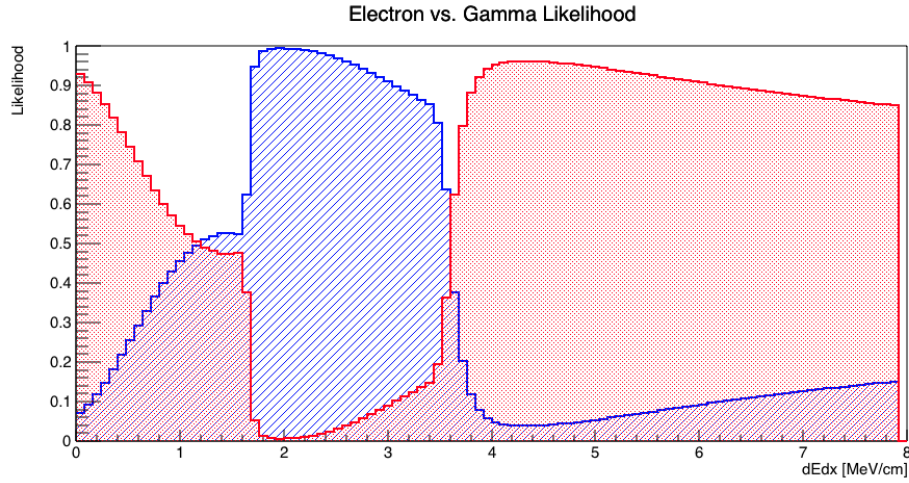


Figure 6.4: *AlgoEMPart*: Computed 1D likelihood vs dE/dx : red is photon, blue is electron.

How the likelihood is computed is described in Section 6.3.1.1.

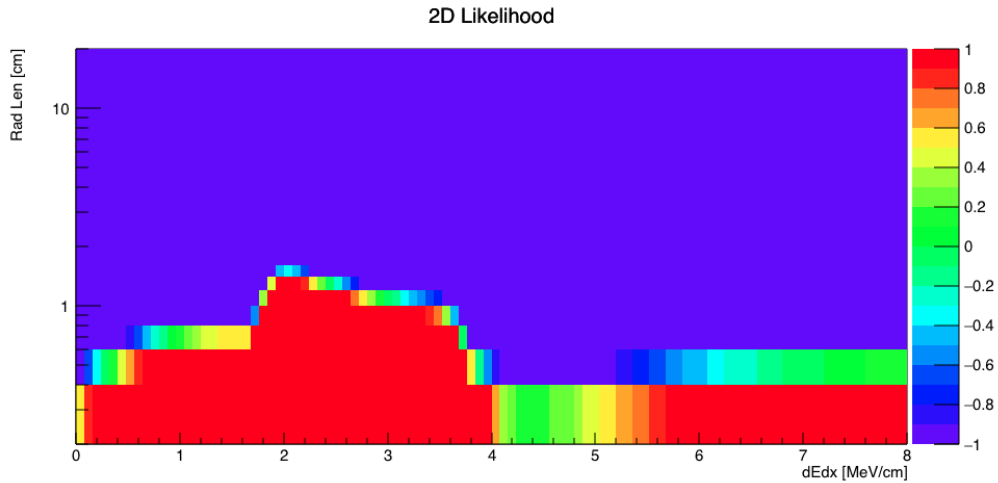


Figure 6.5: *AlgoEMPart* training results on perfect reconstructed electron and photon showers as described in Section 6.3.1.1 integrated over all energies: 2D likelihood distribution (radiation length vs. dE/dx). Low values of likelihood (purple) correspond to photon-like, high values (red) correspond to electron-like.

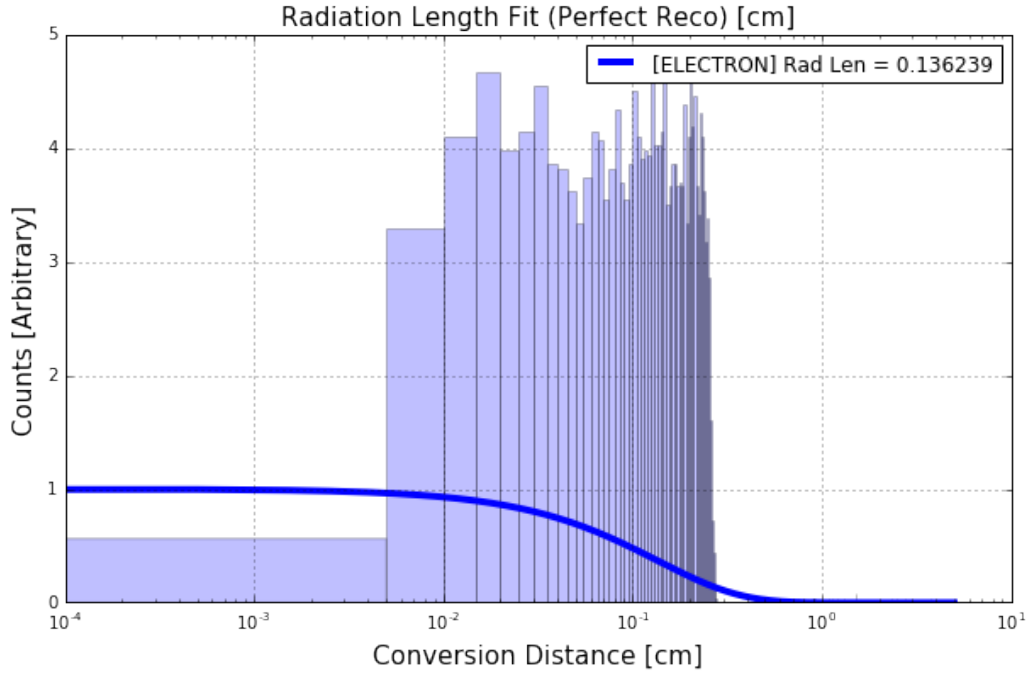


Figure 6.6: *AlgoEMPart training results on perfect reconstructed electron showers as described in Section 6.3.1.1: Radiation length fit to single electron showers. Note the poor quality of the fit as the electron conversion distance for “perfect reconstruction” does not follow an exponential distribution; all conversion distances are below 0.3 centimeters.*

1251 6.3.2 Signal Selection Algorithm

1252 The purpose of this algorithm is to select events with ν_e^{CC} inclusive type topologies. These
1253 topologies involve a single electron at a neutrino interaction vertex, with any number of
1254 protons, charged or neutral pions, or anything else additionally exiting the vertex. Later
1255 on, the sample of selected events will be subjected to further cuts to select only ν_e^{CCQE}
1256 topologies by rejecting events with pions in the final state. This algorithm uses likelihoods
1257 provided by the previously described “AlgoEMPart” (Section 6.3.1) to determine if a shower
1258 is an electron or a photon. This algorithm begins by looping over all candidate ν_e^{CC} elec-
1259 tron showers in the event that have not been removed by upstream cosmic and π^0 tagging
1260 algorithms. Figure 6.9 is a flowchart depicting the decision tree this algorithm uses for each
1261 candidate ν_e^{CC} electron shower. If the algorithm reaches the bottom of the flowchart, that
1262 shower is determined to be from a ν_e^{CC} interaction and the event is saved to be included in

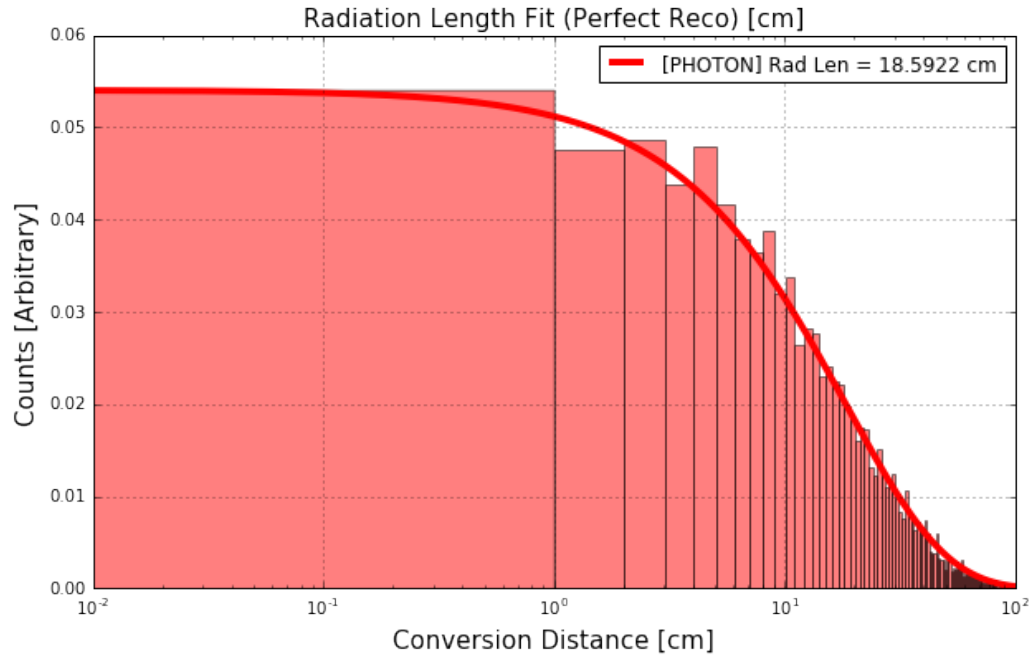


Figure 6.7: *AlgoEMPart training results on perfect reconstructed photon showers as described in Section 6.3.1.1: Radiation length fit to single photon showers.*

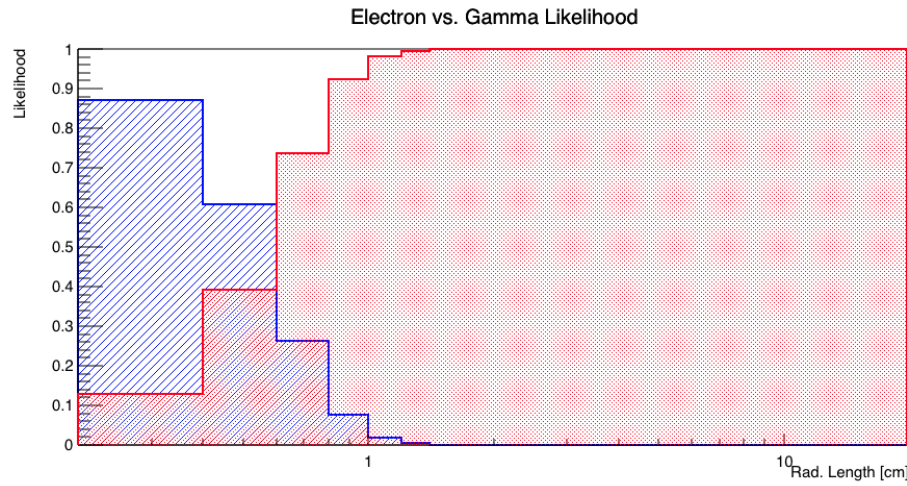


Figure 6.8: *AlgoEMPart: Computed 1D likelihood vs conversion distance (integrated over all energies): red is photon, blue is electron. How the likelihood is computed is described in Section 6.3.1.1.*

1263 analysis. The flowchart refers to determining if two showers are correlated and determining
 1264 if a shower is correlated with the start of a track. A schematic which diagrams how these
 1265 determinations are made is shown in Figure 6.10. A list of configurable parameters and
 1266 their chosen cut values is shown in Table 6.2. A more detailed description of Figure 6.9 is
 1267 given in the following paragraphs.

1268

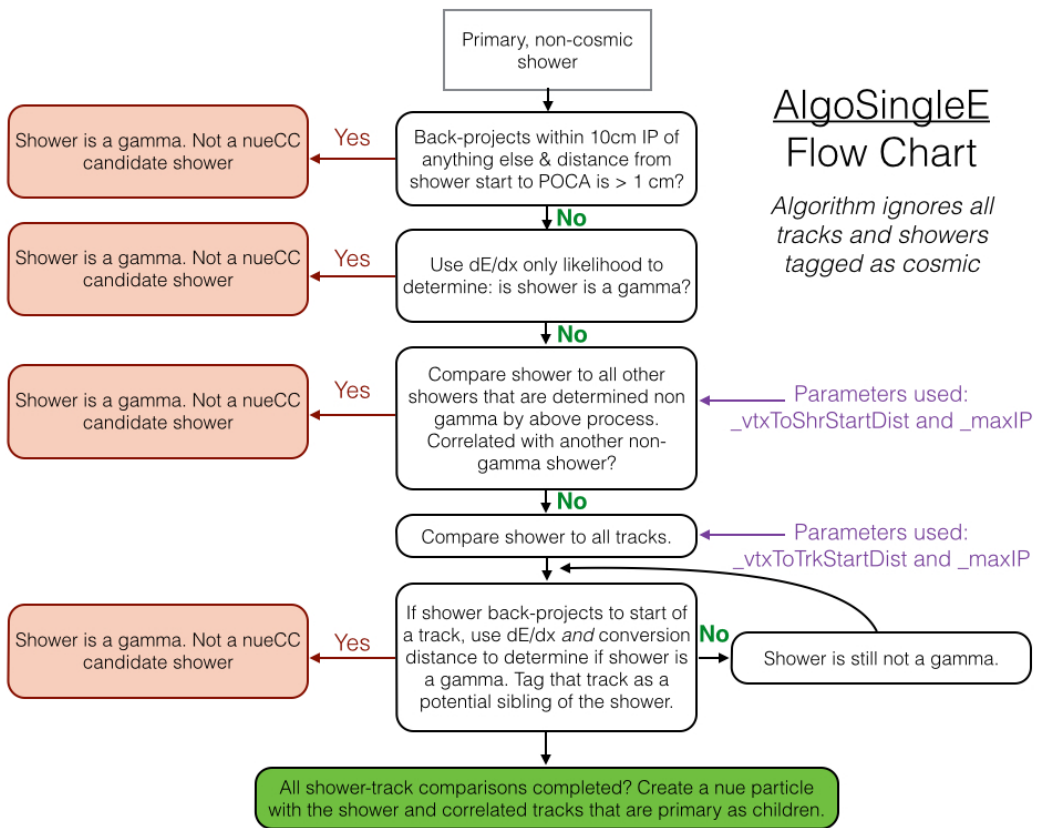


Figure 6.9: A flowchart depicting decisions the algorithm makes for each primary, non-cosmic shower. If the algorithm gets to the bottom of the flowchart, that shower was determined to be from a ν_e^{CC} interaction, and a ν_e particle is created. For clarification of what some acronyms mean, see Figure 6.10.

1269 To begin, the algorithm attempts to reject any showers which are highly likely to be
 1270 photons. For each primary, non-cosmic shower (“shower A” in Figure 6.10), this algorithm
 1271 computes a point of closest approach (POCA) and impact parameter (IP) between the

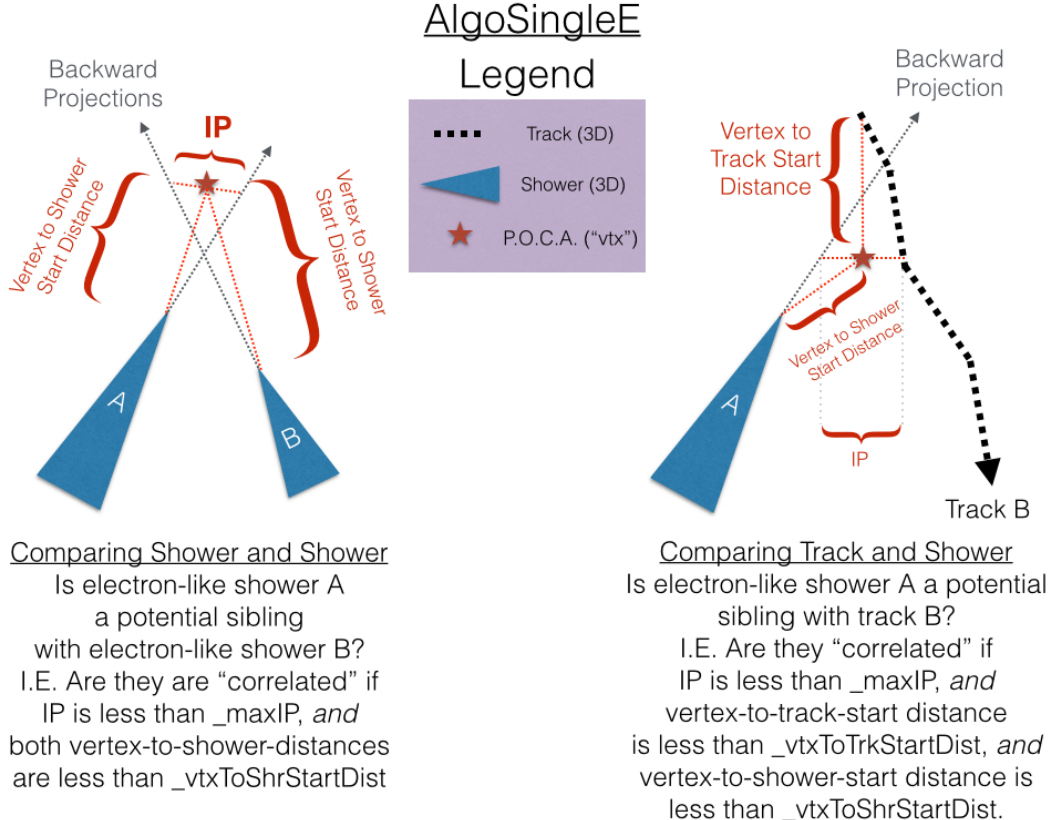


Figure 6.10: *Schematic cartoons indicating how the signal selection algorithm makes decisions determining if two reconstructed showers are correlated, and if a reconstructed shower is correlated with a reconstructed track (as described in Figure 6.9).*

1272 shower’s back-projection and each other track. Additionally, the POCA and IP are com-
 1273 puted between the shower’s back-projection and each other shower axis back-projections.
 1274 If the smallest impact parameter is less than 10 centimeters and the distance between the
 1275 shower’s start point and the point of closest approach is greater than 1 centimeter, the
 1276 algorithm assumes this shower is a photon and it rejects the shower as a potential ν_e^{CC}
 1277 shower, without any dE/dx considerations. The value of 10 centimeters is chosen because
 1278 such a displacement from the vertex would not occur for electron showers, even including
 1279 reconstruction resolution effects⁴. Otherwise, the algorithm continues by using AlgoEM-

⁴Note that for ν_e^{CC} interactions and “perfect reconstruction”, these impact parameters and points of closest approach between the ν_e^{CC} electron shower and other tracks in the event are incredibly small (sub

1280 Part's trained likelihood function to determine based on dE/dx alone whether this shower
1281 is gamma-like and should therefore be ignored.

1282

1283 Assuming this potential ν_e^{CC} shower has so far been found to be electron-like, the algo-
1284 rithm then compares the shower to all other showers in the event that are not marked as
1285 cosmic, and are not already reconstructed to be the descendant of another particle⁵. The
1286 purpose of this portion of the code is to enforce that the topology of interest includes a *sin-*
1287 *gle electron* exiting the neutrino interaction. If any other electron-like showers are nearby
1288 that could be potentially correlated, the shower is rejected as a candidate ν_e^{CC} electron.

1289

1290 The candidate shower is then compared to every track in the event that has not been
1291 tagged as cosmic to look for correlations between the potential ν_e^{CC} electron and tracks
1292 (Figure 6.10). The topology of interest allows for the electron to point back to the *start* of
1293 a track, but *not* to the middle or end of a track (as these showers are likely delta rays or
1294 muon decay Michel electrons). At this point, the code again uses a likelihood from AlgoEM-
1295 Part to determine if the shower is still electron-like, this time using both the shower's dE/dx
1296 and the distance between the shower start and the computed POCA as a radiation length.
1297 This is a more powerful discrimination to determine if the shower remains electron-like. If
1298 the shower remains electron-like and is found to be correlated with the start of a track, the
1299 track is stored as associated with another final state particle of the ν_e^{CC} interaction. The
1300 energy of this track will later be included in the reconstructed neutrino energy.

1301

1302 At this point, a ν_e^{CC} event has been found, and the shower and any associated tracks
1303 are stored to be included in the sensitivity analysis.

centimeter). The cut values are chosen to be much larger to simulate estimated automatic track and shower reconstruction resolutions.

⁵Cosmic tagging and descendant determination are done by upstream event reconstruction algorithms not described in this thesis for readability reasons.

AlgoSingleE: Parameters	
Parameter Name	Cut Value
Use Radiation Length	True
Max Vertex-to-Track-Start Distance	1 cm
Min Vertex-to-Shower-Start Distance	50 cm
Maximum IP	1 cm

Table 6.2: *The list of configurable parameters and their values used in the AlgoSingleE ν_e^{CC} signal selection algorithm. Note that for ν_e^{CC} interactions and “perfect reconstruction”, these actual values the distance-based parameters represent are incredibly small (sub centimeter). The cut values are chosen to be much larger to simulate estimated automatic track and shower reconstruction resolutions.*

1304 6.3.2.1 Configurable Parameters

1305 The configurable parameters for this algorithm are summarized in the Table 6.2. Note that
 1306 with “perfect reconstructed” showers, these distances are always very small (less than 0.1
 1307 centimeters), so these values were chosen to introduce some realism into the algorithm by
 1308 estimating detector resolutions.

1309

1310

1311 6.3.3 Energy Reconstruction

1312 With the candidate ν_e^{CC} interactions identified, the neutrino energy is reconstructed in two
 1313 ways. First, the angle and energy of the selected ν_e^{CC} electron is used to compute an energy,
 1314 E_ν^{CCQE} from the CCQE formula, Equation 5.1. This is the same energy definition that is
 1315 used in the MiniBooNE oscillation analysis. Note that this energy is only valid for truly
 1316 ν_e^{CCQE} interactions, which are a subset of the selected ν_e^{CC} sample. In addition, E_ν^{CCQE} can
 1317 be significantly effected by nuclear effects such as Fermi motion of nucleons in the target
 1318 nucleus.

1319

1320 An additional, more accurate energy estimation, E_{calo} is calculated by looping over all
 1321 particles tagged as descendants of the reconstructed ν_e and adding up their deposited ener-
 1322 gies. For ν_e^{CC} events, this amounts to adding the deposited energy of the electron shower,
 1323 along with the deposited energies from all protons exiting the interaction vertex, and ener-
 1324 gies from charged and neutral pions exiting the vertex (adding the pion masses in the case of
 1325 charged pions). Additionally the electron mass is added, though this changes the calculated
 1326 energy negligibly. Plots describing the neutrino reconstruction performance for correctly
 1327 identified ν_e^{CCQE} interactions can be seen in Figures 6.11 and 6.12. The energy resolution
 1328 for true neutrino energies below 500 MeV is on the order of 15%, and the bias indicates that
 1329 the energy reconstruction method tends to underestimate true neutrino energy by about
 1330 25%. Note that this bias is computed as the mean reconstructed energy of all events in a
 1331 specific true energy bin rather than the center of a Gaussian fit to the central distribution of
 1332 events, so the bias is skewed down by outliers. In addition, the neutrino energy is generally
 1333 underestimated both because energy lost to neutrons or showering particles is not included
 1334 in the energy definition, and because neutrino-induced tracks are not associated with the
 1335 interaction with perfect efficiency.

1336 6.4 Backgrounds

1337 6.4.1 Background Topologies

1338 6.4.1.1 Intrinsic ν_e

1339 The intrinsic ν_e^{CCQE} background comes from electron neutrinos originating from the portion
 1340 of the Booster Neutrino Beam-line (BNB) flux from muon and kaon decays in the decay
 1341 pipe. The topology of these events involve one electron in the final state, with any number of
 1342 protons exiting the interaction vertex, but no pions or muons exiting the interaction vertex.
 1343 Neutral particles included in hadronic activity are also ignored as they are invisible from the
 1344 point of view of a LArTPC. This background is irreducible for a ν_e^{CCQE} appearance search,
 1345 and is the dominant background in this analysis. These intrinsic ν_e events in the relevant
 1346 low energy region are mostly from muon decay in the beam-line. The flux uncertainty

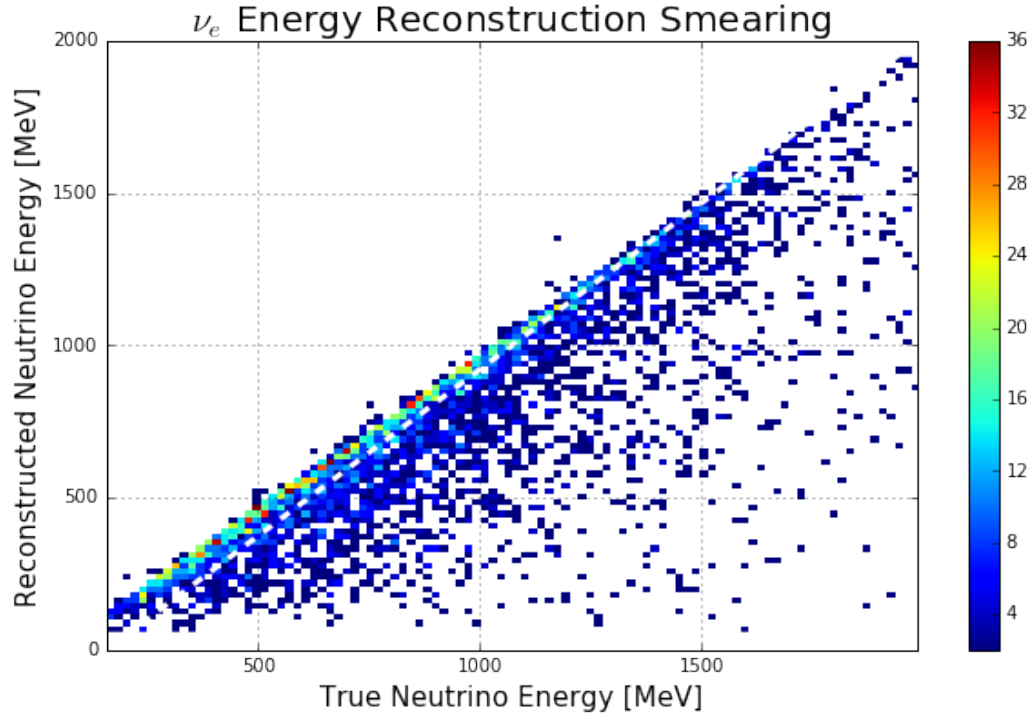


Figure 6.11: *Reconstructed neutrino energy as described in Section 6.3.3 versus true neutrino energy. This plot was made from “perfect reconstruction” objects in correctly identified ν_e^{CCQE} events after all final analysis cuts were placed.*

1347 can be constrained by a parallel ν_μ analysis, as was done in MiniBooNE. The intrinsic ν_e
 1348 events at higher energies mostly come from K^+ decay in the beam-line, although K^+ decay
 1349 neutrinos also make significant contributions to electron neutrinos at lower energy. While
 1350 constraining ν_e from muon decay will be done with a parallel ν_μ analysis, constraining ν_e
 1351 from kaon decay in the beam line is discussed in the next chapter of this thesis.

1352 **6.4.1.2 Intrinsic ν_μ**

1353 The intrinsic ν_μ background comes from ν_μ^{CC} interactions from BNB muon neutrinos. De-
 1354 spite the enormous ratio of ν_μ^{CC} events to ν_e^{CC} events, this is a sub-dominant background in
 1355 this analysis. Potential sources of mis-identifications (MIDs) must always involve at least
 1356 one shower, and there should not be a track recognized as a muon exiting the interaction
 1357 vertex. For this reason, most ν_μ^{CC} MIDs are from either:

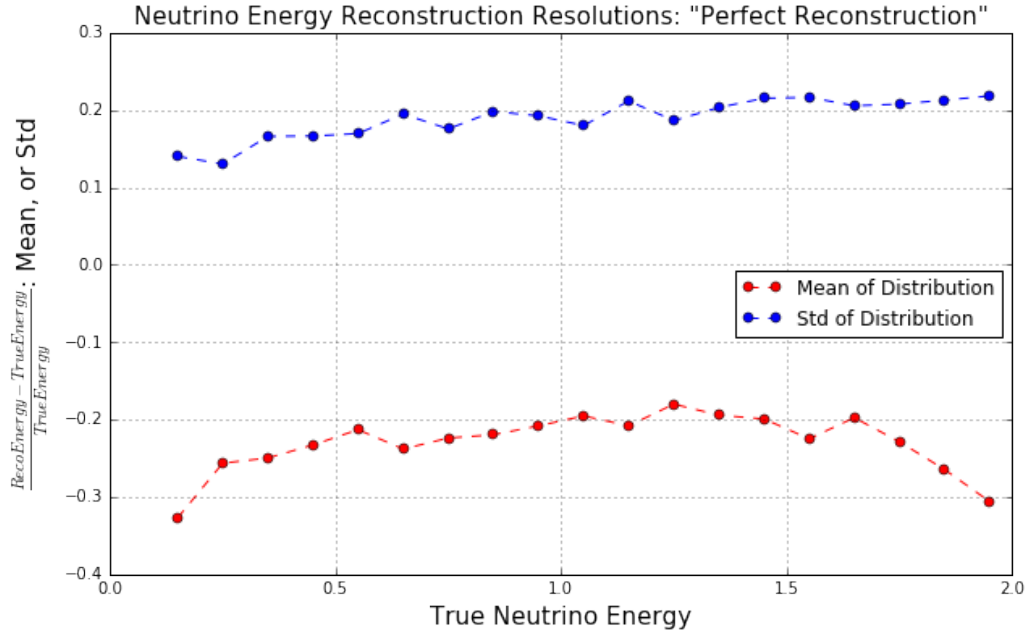


Figure 6.12: A neutrino energy resolution and bias plot. This is created by binning Figure 6.11 in true neutrino energy and making a distribution of $(\text{Reco Energy} - \text{True Energy}) / (\text{True Energy})$. For each bin, the mean (red) and standard deviation (blue) are plotted in the above figure. This plot was made from “perfect reconstruction” objects in correctly identified ν_e^{CCQE} events after all final analysis cuts were placed.

- 1358 1. μ decay electrons (either in flight, or at rest when the energy of the electron is in the
- 1359 very high end of the Michel spectrum, despite their energies being on the order of 50
- 1360 MeV), or
- 1361 2. ν_μ^{CC} events with a neutral pion in the final state.
- 1362 The first MID source is suppressed because the electron points back to the end of the muon
- 1363 track and therefore is generally tagged by event selection algorithms. Additionally, these
- 1364 events are removed if the outgoing track is correctly identified as a muon. However, this
- 1365 background may be more prominent if the muon reconstructed track direction gets flipped
- 1366 (after which, correct identification of the muon track becomes more difficult, and the elec-
- 1367 tron would point back to the *start* of the track). The effect of flipping this track is not
- 1368 included in this analysis, but the impact is expected to be small because there are several

1369 handles on track directionality in LArTPCs including from multiple Coulomb scattering,
 1370 delta rays, and calorimetric information (the presence of a Bragg peak). Also, one can dif-
 1371 ferentiate between such an electron-muon background event from an electron-proton signal
 1372 event by leveraging the differing dE/dx for the muon as compared to the proton.

1373

1374 The second MID source occurs when one of the photons of the neutral pion decay from
 1375 a $\nu_\mu^{CC}\pi^0$ interaction is misidentified as an electron. This background is greatly suppressed
 1376 because the dE/dx of the shower should be photon-like, and the shower points back towards
 1377 the muon start point. The fact that the shower is displaced from the muon start point allows
 1378 for a photon-like likelihood calculation using both the shower dE/dx and the radiation
 1379 length, which is a more powerful discrimination tool to tag the shower as being from a
 1380 photon (as described in Section 6.3.1). Additionally, if the second photon converts inside of
 1381 the detector, this provides another handle that the shower is from a neutral pion. Lastly,
 1382 if the muon is correctly identified as such (from dE/dx or other considerations) then this
 1383 background gets further reduced.

1384 6.4.1.3 Intrinsic Neutral Current (NC)

1385 The intrinsic NC background comes from neutral current interactions by any neutrino type
 1386 from the beam. In these interactions, the neutrino interacts with the exchange of a neutral
 1387 Z boson, and the neutrino carries off some energy and momentum as it exits the detec-
 1388 tor. The predominant NC background for the low energy excess analysis are ν_x (mostly
 1389 ν_μ) interactions with a neutral pion in the final state. This was by far the most dominant
 1390 background in the MiniBooNE ν_e appearance analysis (see Figure 5.4). In this topology,
 1391 one of the photons from the neutral pion decay is mis-identified as an electron coming from
 1392 a ν_e^{CC} interaction. This background is significantly mitigated when both photons convert
 1393 inside of the detector. In that case, the presence of two showers pointing back to a common
 1394 origin allows for the event to be rejected.

1395

1396 An additional NC background topology is NC $\Delta \rightarrow N\gamma$, though this background is sub-
 1397 dominant to the aforementioned neutral pion decays (with a relative rate of about 0.5% as

¹³⁹⁸ compared to neutral pion decays).

¹³⁹⁹ **6.4.1.4 Beam-Induced, TPC External (“B.I.T.E.”)**

¹⁴⁰⁰ This background comes from beam neutrino interactions that occur outside of the TPC
¹⁴⁰¹ sensitive volume, but inside of the cryostat volume (including the cryostat walls). By
¹⁴⁰² volume (and mass), this region is roughly half of the volume of the entire cryostat. The
¹⁴⁰³ predominant topology for this background are neutrino interactions involving a neutral
¹⁴⁰⁴ pion in the final state where only one photon from the pion decay converts inside of the
¹⁴⁰⁵ active volume. Since this photon may not point back to any other reconstructed objects in
¹⁴⁰⁶ the TPC, only its dE/dx can be used in the electron/photon separation likelihood which
¹⁴⁰⁷ provides less discrimination power than if a radiation length could be used as well. Note
¹⁴⁰⁸ that this analysis does not explicitly ask for a visible hadronic vertex, otherwise many of
¹⁴⁰⁹ these backgrounds would be mitigated (though much of the signal would be mitigated as
¹⁴¹⁰ well). In this analysis, this background can be mitigated, as was done in MiniBooNE, with
¹⁴¹¹ cuts like backward-projected distance to a TPC wall, since they are all coming from outside
¹⁴¹² of the TPC.

¹⁴¹³ **6.4.1.5 Cosmic**

¹⁴¹⁴ This background comes from cosmic rays that pass through the detector. The relatively
¹⁴¹⁵ high cosmic rate inside of the detector hall makes for on the order of tens of cosmic rays
¹⁴¹⁶ passing through the detector during the full readout window. Since the readout window
¹⁴¹⁷ is several milliseconds (since this is the time scale with which ionizations drift across the
¹⁴¹⁸ width of the TPC) and the cosmic rate through the detector is on the order of 5 kHz,
¹⁴¹⁹ roughly 20 cosmics arrive during each readout window. Measured reconstructed cosmics for
¹⁴²⁰ an example full readout window of 4.8 ms are shown in Figure 6.13.

¹⁴²¹

¹⁴²² Cosmic MID topologies include but are not limited to showers that radiate off of cosmic
¹⁴²³ ray muons, and showers born from cosmic neutron scatters. The vast majority of MIDs
¹⁴²⁴ from cosmics can be removed by requiring the reconstructed neutrino interaction is matched
¹⁴²⁵ to a flash inside of the beam gate window. Given the ratio of beam gate window size to

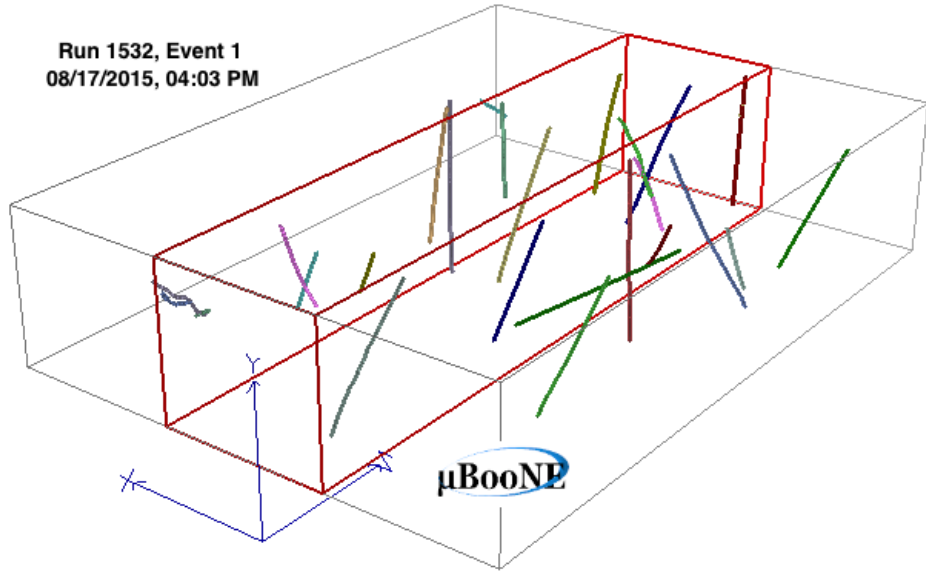


Figure 6.13: A 3D event display showing measured cosmic tracks entering the MicroBooNE detector. The three boxes show the full readout window of the detector which corresponds to 4.8 ms. The red highlighted box shows the physical volume of the TPC. The colored lines are 3D reconstructed cosmic tracks. Data taken in August, 2015.

1426 readout window size ($\frac{1.6\mu s}{4.8ms} = 0.0003$), this requirement mitigates a large fraction of the
 1427 cosmic backgrounds. However, the majority of triggered beam events are not triggered by a
 1428 neutrino interaction in them but are instead triggered by a cosmic ray that arrived during
 1429 the beam gate window. These events are referred to as “in-time” cosmics. Given the num-
 1430 ber of readouts triggered by cosmics inside of the beam gate window rather than neutrinos
 1431 arriving inside of the beam gate window, the cosmics background can be sizable, especially

in the relevant low energy region. The measured relative rate of bright reconstructed flash times inside the $1.6 \mu\text{s}$ beam spill window with respect to the constant cosmic background in MicroBooNE is shown in Figure 6.14. The ratio of cosmic-triggered events to neutrino triggered events from that plot is 1 : 0.45, and only about half of those neutrino interactions are inside of the active volume (and are reconstructible), making the ratio closer to 5 triggered cosmic readouts for every neutrino triggered readout in which the neutrino is reconstructible⁶.

1439

In addition to these “in-time” cosmics (those that triggered a readout and arrived during the beam gate window), an additional cosmic background comes from events in which a neutrino interacts inside of the beam gate window, triggering a readout, but an out-of-time cosmic MID topology gets incorrectly matched to the neutrino flash. These cosmic MIDs are appropriately referred to as “out-of-time” cosmics. The “out-of-time” cosmic background is not included in this analysis, but its size relative to the “in-time” cosmics is small.

1446

1447 6.4.2 Background Normalization

As described in Section 6.2.1, the simulated background samples used in this analysis can be classified either as beam-induced, or cosmic. Each beam-induced background has an associated simulated protons-on-target (POT) generated, and they are each normalized to 6.6×10^{20} POT, the nominal amount of beam scheduled to be delivered to MicroBooNE over the course of three years of running. The cosmic simulated sample does not have an associated POT, but instead has an associated total exposure time. The normalization of this sample must involve disregarding the event selection cut in which a reconstructed optical flash occurs within the timing of the beam gate window (described in Section 6.4.3).

⁶While this calculation assumes the optical flashes are bright (flashes greater than 50 photoelectrons), the triggering threshold is lower than that so this ratio estimate is conservative; in reality the ratio is larger than 5:1.

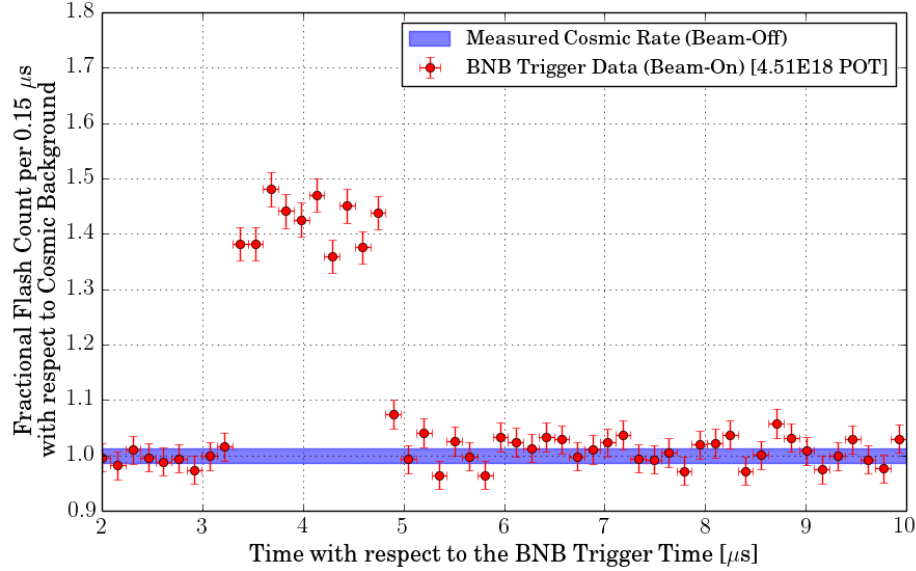


Figure 6.14: *The measured distribution of flash times (requiring flashes greater than 50PE) with respect to the trigger time for BNB-triggered events, shown as a ratio to the expected cosmic rate from off-beam data. The blue band denoting the cosmic rate was centered at one, with a width corresponding to the measured uncertainty in the cosmic rate. A clear excess can be seen due to neutrinos between 3 and 5 μs after the trigger. This is where the neutrinos were expected based on the RWM signal arrival time. A total of 1.92E6 BNB triggered events (unbiased trigger) were used to produce this plot.*

1456 The total beam-gate-open exposure time corresponding to 6.6×10^{20} POT is 211 seconds:

$$\frac{6.6 \times 10^{20} \text{ POT}}{5 \times 10^{12} \frac{\text{POT}}{\text{spill}}} \times 1.6 \frac{\mu\text{s}}{\text{spill}} = 211 \text{ seconds} \quad (6.3)$$

1457 Therefore, a simple cosmic background scale factor is computed based on the simulated
1458 cosmic exposure time corresponding to 211 seconds.

1459 6.4.3 Analysis Cuts and Results

1460 A number of additional analysis cuts are placed on the selected candidate ν_e^{CC} events. The
1461 purpose of these cuts is to first down-sample the selected ν_e^{CC} selected events into a sample
1462 of ν_e^{CCQE} events by removing those reconstructed as having pions in the final state. An

1463 additional reason to place these cuts is to mitigate backgrounds that the event selection
1464 algorithms were unable to remove themselves. The analysis cuts used are described here.

1465

1466 The analysis cuts placed are:

1467 1. The reconstructed ν_e interaction is matched to a flash inside of the beam gate win-
1468 dow (this cut is not placed on the cosmic background simulated sample for reasons
1469 described in Section 6.4.2).

1470 2. If the reconstructed ν_e interaction has additional particles reconstructed to be in the
1471 final state, those particles are limited to protons only (using assumed perfect efficiency
1472 to tag a track as a proton). This down-samples the ν_e^{CC} selected sample to specifically
1473 ν_e^{CCQE} .

1474 3. Minimum primary ν_e^{CC} reconstructed electron energy deposited of 60 MeV.

1475 4. A fiducial volume of 10 cm from all sides of the detector is placed on the neutrino
1476 interaction vertex.

1477 5. A projected-backwards-distance-to-wall cut of 40 cm is placed on the primary ν_e^{CC}
1478 reconstructed electron. The projected-backwards-distance-to-wall cut is computed by
1479 back-projecting the reconstructed ν_e^{CC} electron along its shower axis until it intersects
1480 with the TPC boundaries. The distance between the electron start point and the wall
1481 intersection point is the distance on which the cut is placed. This cut removes photons
1482 that are coming into the detector from outside and, thus, will point back to the TPC
1483 boundaries.

1484 The efficiency of the event selection algorithms with “perfect reconstruction” inputs
1485 to select signal events and to select background events (“MID efficiency”) is summarized
1486 in Table 6.3. The numerator of this efficiency is the number of events tagged as ν_e^{CCQE}
1487 candidate interactions and the denominator is the true number of events with the speci-
1488 fied interaction type. The second column in the table does not include the additional final
1489 analysis selection cuts which are placed on the reconstructed interactions in the efficiency
1490 numerator, and the third column does. The background categories are described in more

Event Selection Efficiencies			
True Event Type	Efficiency	Efficiency Including Analysis Cuts	Final Number of Events
ν_e^{CCQE}	82.09%	61.42%	425.4
ν_μ^{CC}	0.68%	0.02%	21.3
ν_x^{NC}	0.86%	0.13%	50.6
B.I.T.E.	1.07%	0.05%	92.5
Cosmic	5.88%	0.12%	23.1

Table 6.3: *Event selection efficiencies on “perfect reconstruction”. The right-most column indicates the final number of selected events including analysis cuts, normalized to the nominal MicroBooNE running period of 6.6×10^{20} protons on target.*

1491 detail in Section 6.4.1. In the case of the cosmic background category, the denominator is
 1492 the true number of events triggered by a cosmic arriving within the beam gate window that
 1493 do not include a neutrino interaction. Note that efficiency to select ν_e^{CCQE} events including
 1494 all analysis cuts is 61% and albeit with “perfect reconstruction”, it is still more than twice
 1495 the MiniBooNE efficiency as was planned.

1496

1497 The backgrounds to the ν_e^{CCQE} appearance search in MicroBooNE are shown in Figure
 1498 6.15, normalized to the nominal MicroBooNE expected POT, with statistical-only error
 1499 bars shown. The event selection is described in Section 6.3, the background topologies
 1500 described in Section 6.4.1, the relative normalization between samples described in Section
 1501 6.4.2, and the energy reconstruction described in Section 6.3.3.

1502 **6.5 MiniBooNE Low Energy Excess Signal Modeling In Mi-**
 1503 **croBooNE**

1504 This section describes how the signal sample is generated for this sensitivity study, along
 1505 with the necessary assumptions made in the process. First, the signal is assumed to orig-
 1506 inate from beam-induced ν_e^{CCQE} interactions (this is the electron-like hypothesis for the

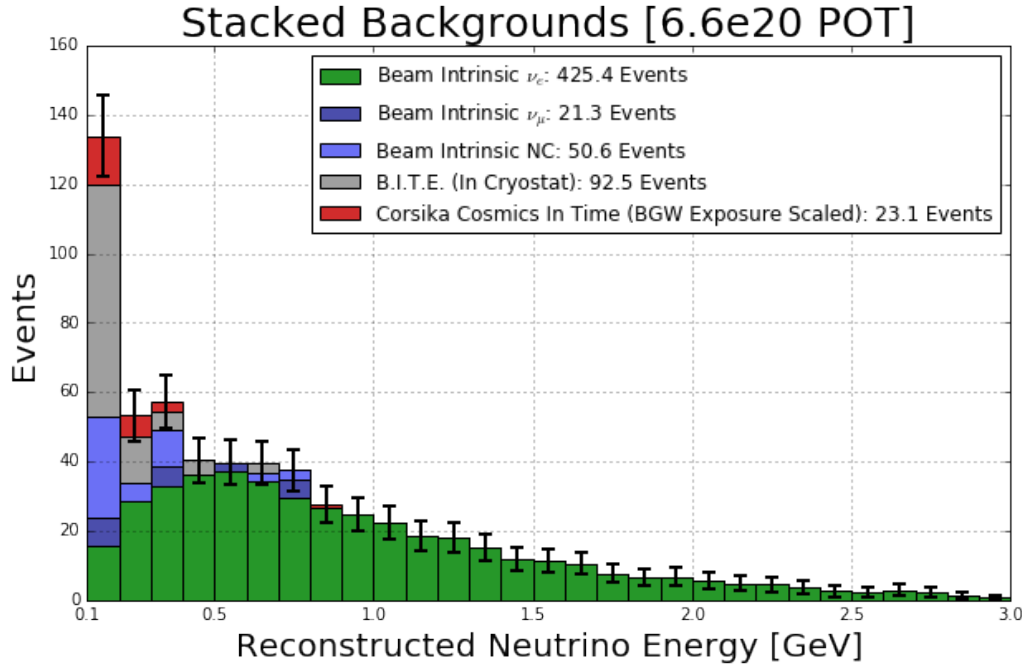


Figure 6.15: The backgrounds to the ν_e^{CCQE} appearance search in MicroBooNE with statistical-only error bars shown. The event selection is described in Section 6.3, the background topologies described in Section 6.4.1, the relative normalization between samples described in Section 6.4.2, and the energy reconstruction described in Section 6.3.3.

excess). No study for a photon-like excess is described in this thesis. In this electron-like excess sensitivity estimate, the signal sample consists of simulated intrinsic ν_e^{CCQE} interactions from the BNB generated uniformly throughout the MicroBooNE TPC. The energy and angle of these events are re-weighted to match the published energy and angle distributions of the excess as observed by MiniBooNE.

1512

1513 The MiniBooNE public data set [29] provides one dimensional distributions of u_z , E_{vis} ,
 1514 and E_ν^{CCQE} for the excess events, where u_z is the z-direction cosine (the z- component
 1515 of the unit momentum) of the observed particle in the low energy excess sample, E_{vis} is
 1516 the visible energy associated with the event, and E_ν^{CCQE} is the calculated neutrino energy
 1517 assuming the interaction was charged current quasi-elastic (see Equation 5.1).

1518

1519 Given these three one-dimensional distributions, a two-dimensional distribution of u_z
 1520 vs. E_{vis} is built by using the CCQE formula⁷. By comparing the MicroBooNE signal sam-
 1521 ple two-dimensional histogram of ν_e^{CCQE} electron u_z vs. E_{vis} to this MiniBooNE excess
 1522 distribution, re-weighting factors are computed to reshape the MicroBooNE signal sample
 1523 to match the MiniBooNE excess in this parameter space.

1524

1525 The strategy to generate the MiniBooNE excess two dimensional distribution is as fol-
 1526 lows:

- 1527 1. Draw independently from each of the the two one-dimensional histograms: u_z and
 1528 E_{vis} .
- 1529 2. For every drawn pair, calculate the corresponding E_ν^{CCQE} with Equation 5.1 and
 1530 decide whether to accept it according to the published MiniBooNE excess E_ν^{CCQE}
 1531 one-dimensional distribution.
 - 1532 • The probability of accepting a calculated E_ν^{CCQE} that falls within the bin's
 1533 boundaries is equal to the height of the unit-normalized E_ν^{CCQE} distribution
 1534 in any given bin.
- 1535 3. Repeat this process until the number of accepted pairs = $N \times$ Integrated number of
 1536 excess events in the u_z distribution (choosing N to be large: E.G. $N = 1000$). This
 1537 two dimensional distribution represents the observed excess as seen from MiniBooNE.
- 1538 4. Divide this distribution by the MiniBooNE published efficiency for single electrons
 1539 (given as a function of E_{vis}) to uncover the shape of the true excess event distribution
 1540 in MiniBooNE⁸.
- 1541 5. Smooth the resulting two-dimensional distribution with a default ROOT TH2::Smooth()
 1542 function.

⁷The CCQE energy formula should use lepton energy, E_e , but here E_{vis} is used instead. This is assuming that the lepton energy is approximately the same as the visible energy.

⁸No efficiency as a function of any other variable (E.G. u_z) has been published by MiniBooNE.

1543 The resulting two-dimensional distribution of u_z vs. E_{vis} for the true MiniBooNE excess
1544 events is shown in Figure 6.16.

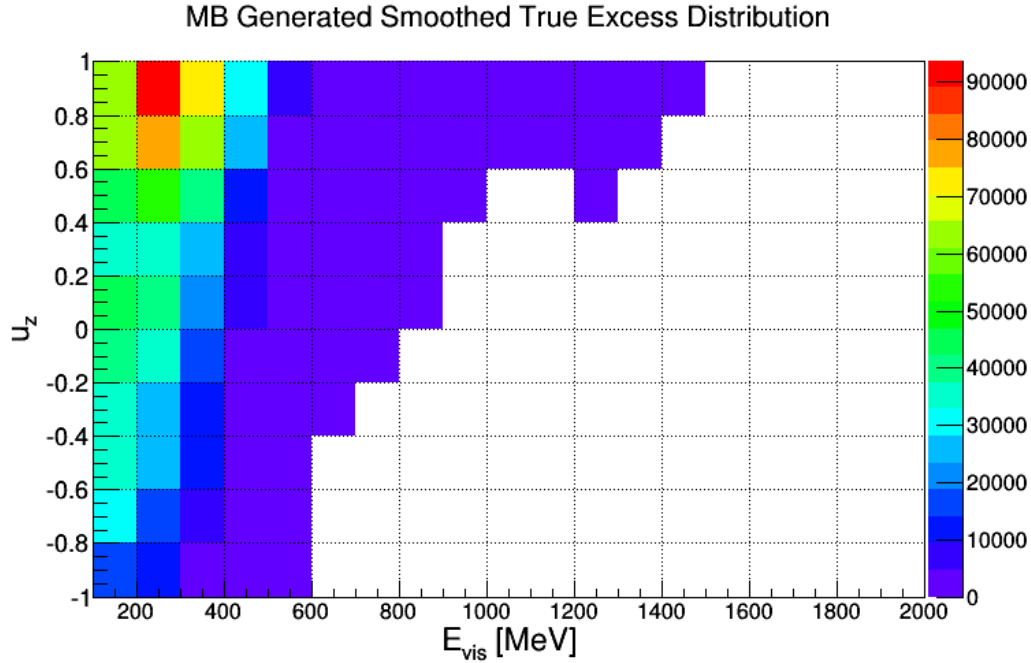


Figure 6.16: *The computed distribution of u_z (how forward-going the event is) vs. E_{vis} for $N = 1000$ times the MiniBooNE low energy excess (raw) events.*

1545 While the shape of the simulated MicroBooNE signal events is determined by the above
1546 process, the absolute normalization of this sample is computed by comparing the relative
1547 size of the signal with respect to the intrinsic ν_e backgrounds as observed by MiniBooNE.
1548 This is appropriate to do only because of the assumption that the origin of the low energy
1549 excess is intrinsic BNB ν_e . From MiniBooNE data and MC, there are 187.7 excess signal
1550 events and 148.4 intrinsic ν_e events in the E_ν^{CCQE} energy range from 100 to 600 MeV. In
1551 this analysis, the number of intrinsic ν_e events in that E_ν^{CCQE} energy range in MicroBooNE
1552 is computed to be 159.8, and therefore the simulated signal sample is normalized to have
1553 $159.8 * (187.7 / 148.4) = 201.3$ events in that E_ν^{CCQE} energy range.

1554

1555 **6.5.1 Sensitivity Results**

1556 Shown in Figure 6.17 is the previously shown stacked backgrounds, now with the scaled
 1557 MiniBooNe low energy excess signal included. Also labeled on the plot is the computed
 1558 significance of 11.57σ , including only statistical errors. The details on the computation of
 1559 the significance is described in the next section.

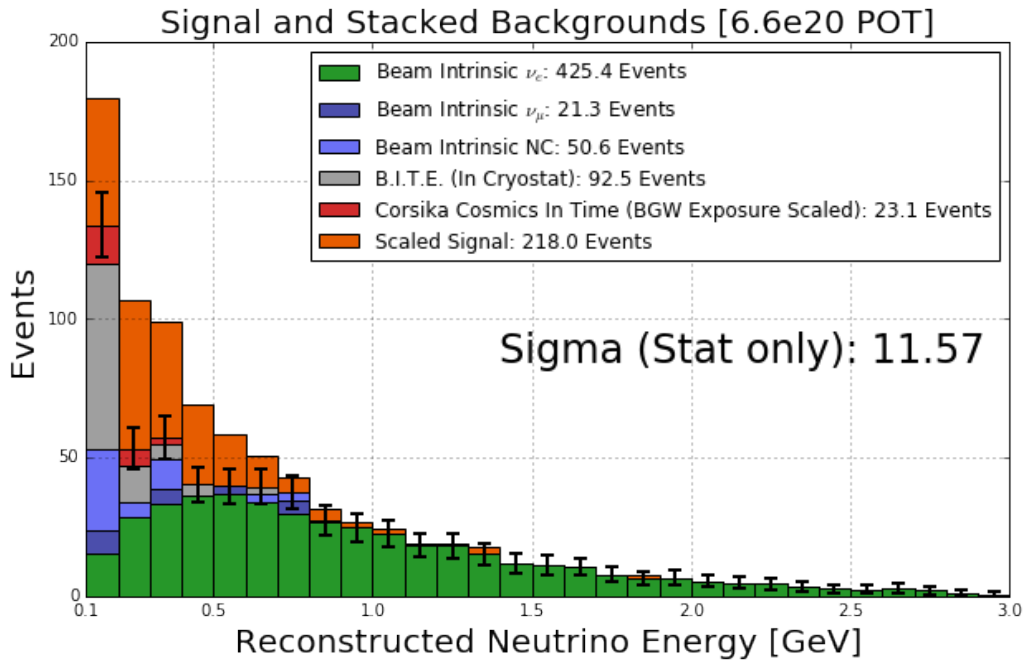


Figure 6.17: The backgrounds to the ν_e^{CCQE} appearance search in MicroBooNE with scaled signal drawn. The event selection is described in Section 6.3, the background topologies described in Section 6.4.1, the relative normalization between samples described in Section 6.4.2, and the energy reconstruction described in Section 6.3.3. The scaled signal is described in Section 6.5.

1560 **6.5.1.1 Significance Calculation**

1561 For a given stacked background plot with a scaled signal on top, the statistical-only signif-
 1562 icance is can be computed with a chi-square test statistic as:

$$\sigma = \sqrt{\Delta\chi^2} = \sqrt{\vec{S}^T E^{-1} \vec{S}} \quad (6.4)$$

1563 where \vec{S} is a vector containing the size of the signal, with length equal to the number of
 1564 bins in the histogram, n , and E is the $n \times n$ statistical-only covariance matrix (diagonal
 1565 matrix with entries equal to the summed number of background events per bin).

1566 **6.5.1.2 Systematic Error Estimates**

1567 In order to compute a realistic significance to the low energy excess in this analysis, a treat-
 1568 ment of systematic uncertainties is necessary. While this is a detailed and important study,
 1569 a conservative simplified estimation of these uncertainties is described here.

1570

1571 Previous studies described in the proposal for the Short Baseline Neutrino experiment
 1572 (which includes MicroBooNE as one of three detectors) [30] quote the integrated ν_e and ν_μ
 1573 flux uncertainties to be on the order of 10 to 15%. This number comes from systematic
 1574 uncertainty estimates related to primary production of π^+ , π^- , K^+ , K^- , and K_L^0 in $p + Be$
 1575 collisions at 8 GeV in the BNB, secondary interactions of p , n , π^\pm in the beryllium target
 1576 and aluminum horn, and beam focusing with the magnetic horn.

1577

1578 The SBN studies also quote the cross section uncertainties to be on the order of 20%.
 1579 This number comes from varying model parameters in the GENIE neutrino interaction
 1580 generator to determine 1σ uncertainties. Parameters varied include axial mass for CCQE
 1581 events, axial mass for CC resonant neutrino production, axial mass for NC resonant pro-
 1582 duction, neutral current normalization, and switching of deep inelastic scattering nuclear
 1583 models. A full list of parameters varied and their 1σ uncertainties can be found in the
 1584 GENIE manual, Section 8.1 [25].

1585

1586 While many of these uncertainties are strongly correlated across energy bins, a very
 1587 conservative approach is to simply include a flat, uncorrelated flux uncertainty of 15% and
 1588 a similarly flat, uncorrelated cross section uncertainty of 20%. These uncertainties are ap-
 1589 plied to all beam-induced backgrounds in this analysis. The systematic uncertainties on
 1590 the cosmic-induced backgrounds are not known, but given the relatively small size of these
 1591 backgrounds in this analysis, even a systematic of 50% would have small impact on the

1592 final computed significance, so this systematic is neglected. Additional uncertainties from
 1593 sources including detector systematics are expected to be sub-dominant to the relatively
 1594 large flux and cross-section systematics, and are therefore similarly neglected. It is impor-
 1595 tant to note that these conservative estimates are ignoring many *in situ* measurements that
 1596 can be done in MicroBooNE to constrain the uncertainties, as MiniBooNE did. Doing a
 1597 combined ν_e plus ν_μ analysis highly constrains the flux and cross-section systematics and
 1598 reduces them considerably. Such a constraint is done with a combined error matrix which
 1599 has off-diagonal elements relating the ν_e and ν_μ event numbers. The ν_e cross-section un-
 1600 certainties are constrained by the observed ν_μ events since ν_e and ν_μ cross-sections are the
 1601 same except at very low neutrino energies where mass effects become relevant, but these
 1602 are theoretically well understood. Also, NC π^0 measurements help constrain cross section
 1603 \times flux uncertainties for that process, but this background should be small in any case for
 1604 the MicroBooNE measurement.

1605

1606 In order to include the flux and cross-section systematics in the significance calculation,
 1607 Equation 6.4 is modified. As quoted, E is the $n \times n$ diagonal covariance matrix with
 1608 entries equal to the summed number of background events per bin. To include the flux and
 1609 cross-section systematics, E is modified as

$$E = E_{\text{stat}} + E_{\text{flux}} + E_{\text{xsec}} \quad (6.5)$$

1610 where E_{stat} is the previous statistical-only covariance matrix, while E_{flux} represents the
 1611 assumed uncorrelated flux systematic and E_{xsec} the assumed uncorrelated cross section
 1612 systematic. E_{flux} is diagonal with entries equal to the number of beam-induced (non-cosmic)
 1613 background events in that bin times the fractional uncertainty, squared:

$$E_{\text{flux}}^{i,i} = (N_{\text{beam-induced}}^i * 0.15)^2 \quad (6.6)$$

1614 and E_{xsec} is similarly diagonal:

$$E_{\text{xsec}}^{i,i} = (N_{\text{beam-induced}}^i * 0.20)^2 \quad (6.7)$$

¹⁶¹⁵ **6.5.1.3 Realistic Shower Reconstruction Efficiency**

¹⁶¹⁶ So far in this analysis, the shower reconstruction efficiency has been 100% because the
¹⁶¹⁷ input objects are “perfect reconstruction”. In order to emulate a more realistic potential
¹⁶¹⁸ shower reconstruction efficiency, an additional study has been done in which the shower
¹⁶¹⁹ reconstruction efficiency is modeled in an energy dependent way, though the efficiency is
¹⁶²⁰ effectively constant at 85% for showers with energy included in this analysis (above 60
¹⁶²¹ MeV deposited). The value of 85% was chosen because this is approximately the maximum
¹⁶²² shower efficiency for electromagnetic showers with energy between 50 MeV and 5 GeV
¹⁶²³ published by the ICARUS collaboration [31]. The resulting stacked background histogram
¹⁶²⁴ with modeled signal is shown in Figure 6.18. The computed (statistical only) significance
¹⁶²⁵ when realistic shower reconstruction efficiencies are included in the analysis is 10.10σ .

¹⁶²⁶ Note that in comparing Figure 6.17 to Figure 6.18, not all sample sizes are simply
¹⁶²⁷ reduced by 15%. For example, the intrinsic NC backgrounds actually increase when the
¹⁶²⁸ shower reconstruction efficiency is decreased. This is because these backgrounds arise pri-
¹⁶²⁹ marily from π^0 decays, and they are mitigated by event selection algorithms that locate
¹⁶³⁰ both subsequent photon showers pointing back to a common origin and correlate them to-
¹⁶³¹ gether. With reduced shower reconstruction efficiency, sometimes only one of the π^0 decay
¹⁶³² showers gets reconstructed and subsequently gets misidentified as a candidate ν_e^{CC} electron.

¹⁶³³ **6.5.1.4 Final Results**

¹⁶³⁴ A complete summary of MicroBooNE’s computed significance to the MiniBooNE low en-
¹⁶³⁵ ergy excess assuming an electron-like signal hypothesis for “perfect reconstructed” objects,
¹⁶³⁶ “perfect reconstructed objects” with simulated realistic shower reconstruction efficiency,
¹⁶³⁷ with and without conservative systematic uncertainties is shown in Table 6.4.

¹⁶³⁸ **6.5.1.5 Next Steps**

¹⁶³⁹ The described “perfect reconstruction” sensitivity study to an electron-like excess is an
¹⁶⁴⁰ important tool for MicroBooNE. The event selection algorithms have been developed with
¹⁶⁴¹ these objects, and are ready to be used out-of-the-box when automated track and shower
¹⁶⁴² reconstruction efforts become more fruitful in the future. Already the algorithms I have

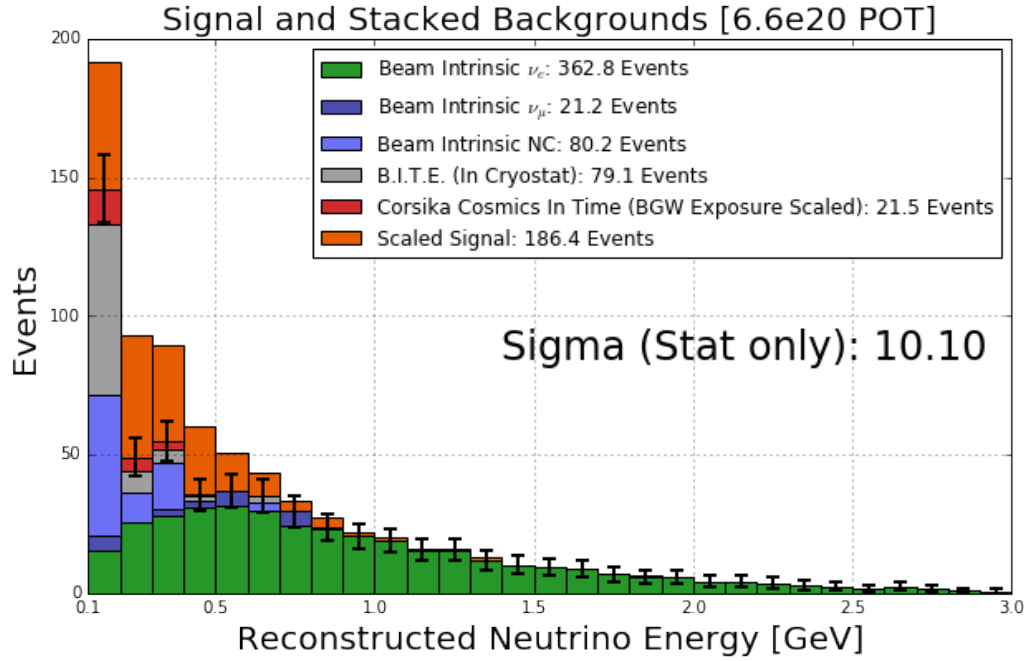


Figure 6.18: The backgrounds to the ν_e^{CCQE} appearance search in MicroBooNE with scaled signal drawn. The event selection is described in Section 6.3, the background topologies described in Section 6.4.1, the relative normalization between samples described in Section 6.4.2, and the energy reconstruction described in Section 6.3.3. The scaled signal is described in Section 6.5. Here the shower reconstruction efficiency has been decreased from the “perfect reconstruction” value of 100% to 85% to emulate possible realistic shower reconstruction efficiencies.

1643 developed are being used in combination with samples of MC simulation analyzed with full
 1644 reconstruction programs to make a better sensitivity estimate. Efforts to apply systematic
 1645 errors to this full reconstruction estimate are also in the process of being implemented. This
 1646 sensitivity study can be used to set goals for the experiment by smearing or modifying the
 1647 “perfect reconstruction” objects. For example, with this analysis the sensitivity to the low
 1648 energy excess can be computed as a function of shower reconstruction efficiency to drive
 1649 the shower reconstruction efforts. Also, the sensitivity as a function of POT delivered has

MicroBooNE Sensitivity Significances		
“Perfect Reco” (stat only)	“Realistic Reco” (stat only)	“Realistic Reco” (stat+sys)
11.57σ	10.10σ	6.52σ

Table 6.4: *Summary of computed significances to the MiniBooNE low energy excess in MicroBooNE assuming an electron-like signal hypothesis.*

1650 already been used to guide discussions on data blinding⁹.

1651

1652 As mentioned, no photon-like excess search is described in this thesis. It is important to
 1653 determine a sensitivity to an electron-like excess as well as a photon-like excess, because the
 1654 true origin of the excess is still unknown. In order to conduct a photon-like excess search,
 1655 event selection algorithms and analysis cuts would have to be developed to search for single
 1656 photon events rather than single electron events.

1657

1658 An important takeaway from this electron-like excess analysis is that systematics play
 1659 an important role in the ultimate sensitivity. The flux systematic is particularly large, but
 1660 is constrained by a ν_e and ν_μ combined analysis. As shown, the largest background in the
 1661 MicroBooNE low energy excess search is from intrinsic ν_e in the beam, which come from
 1662 either muon decay in the beam-line, or kaon decay in the beam-line. In the low energy
 1663 region, the majority of intrinsic ν_e come from muon decay, which is tied to the observed ν_μ
 1664 events, as demonstrated by MiniBooNE. Constraining the remaining ν_e from kaon decay
 1665 can be done by observing the high energy ν_μ rate, the topic of the next chapter.

⁹The MicroBooNE Collaboration allows for a small sample (about 7.5%) of its nominal collected neutrino data to be available to analyzers for reconstruction efforts and data to simulation comparisons. Developing analyses on a small subsample of the data (the “unblinded” portion) and then executing the analysis on the full data set only after it has been thoroughly vetted is important to prove that the analysis isn’t biased towards a particular result.

1666 **Chapter 7**

1667 **Studies of Kaons Produced at the**
1668 **Proton Target**

1669 This chapter of the thesis will describe a MicroBooNE analysis done with the goal of con-
1670 straining the intrinsic ν_e background for the previously described low energy excess search.
1671 As shown, this is the dominant background in the search. Over the entire booster neu-
1672 trino beam energy range, 38% of the intrinsic ν_e background comes from kaon decay in the
1673 booster neutrino beam-line. The breakdown of ν_e interactions from the beam by parentage
1674 is shown in Figure 7.1. The systematic uncertainty on the flux of ν_e from kaon decay is one
1675 of the largest uncertainties reducing the low energy excess significance; this uncertainty was
1676 set to 40% in initial MiniBooNE publications, which is discussed in more detail in Section
1677 7.1. This chapter will describe how measuring the highest energy ν_μ interactions in Mi-
1678 croBooNE provides information about the kaon production in the beam-line, and constrain
1679 this important systematic. Exactly how these events are reconstructed and selected will be
1680 described, data to Monte Carlo comparisons will be shown, and the future prospects and
1681 next steps for this analysis will be discussed.

1682 **7.1 BNB Kaon Production Introduction and Motivation**

1683 As described in Chapter 4, the BNB is predominantly composed of ν_μ (92.9%) and $\bar{\nu}_\mu$ (6.5%)
1684 with a small contamination of ν_e and $\bar{\nu}_e$ (0.6% combined). The BNB flux by neutrino type

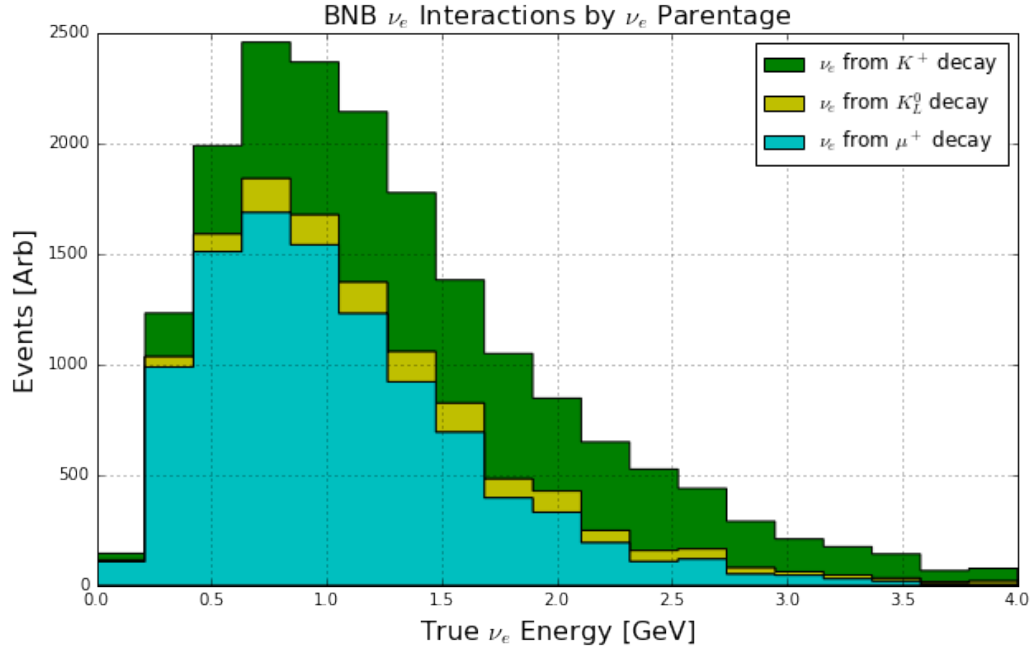


Figure 7.1: The breakdown of ν_e^{CC} interactions in MicroBooNE from the booster neutrino beam-line by ν_e parentage. ν_e from K^+ decay is the primary contributor to the intrinsic ν_e interaction rate at higher neutrino energies.

at the MicroBooNE detector in neutrino-mode running is shown in Figure 7.2.

The decay modes producing beam ν_μ and $\bar{\nu}_\mu$ are

$$\bullet \pi^+ \rightarrow \mu^+ + \nu_\mu$$

$$\bullet K^+ \rightarrow \mu^+ + \nu_\mu$$

$$\bullet \pi^- \rightarrow \mu^- + \bar{\nu}_\mu$$

and the decay modes producing beam ν_e and $\bar{\nu}_e$ are

$$\bullet K^+ \rightarrow \pi^0 + e^+ + \nu_e$$

$$\bullet \mu^+ \rightarrow e^+ + \bar{\nu}_\mu + \nu_e$$

$$\bullet K_L^0 \rightarrow \pi^- + e^+ + \nu_e$$

$$\bullet K_L^0 \rightarrow \pi^+ + e^- + \bar{\nu}_e.$$

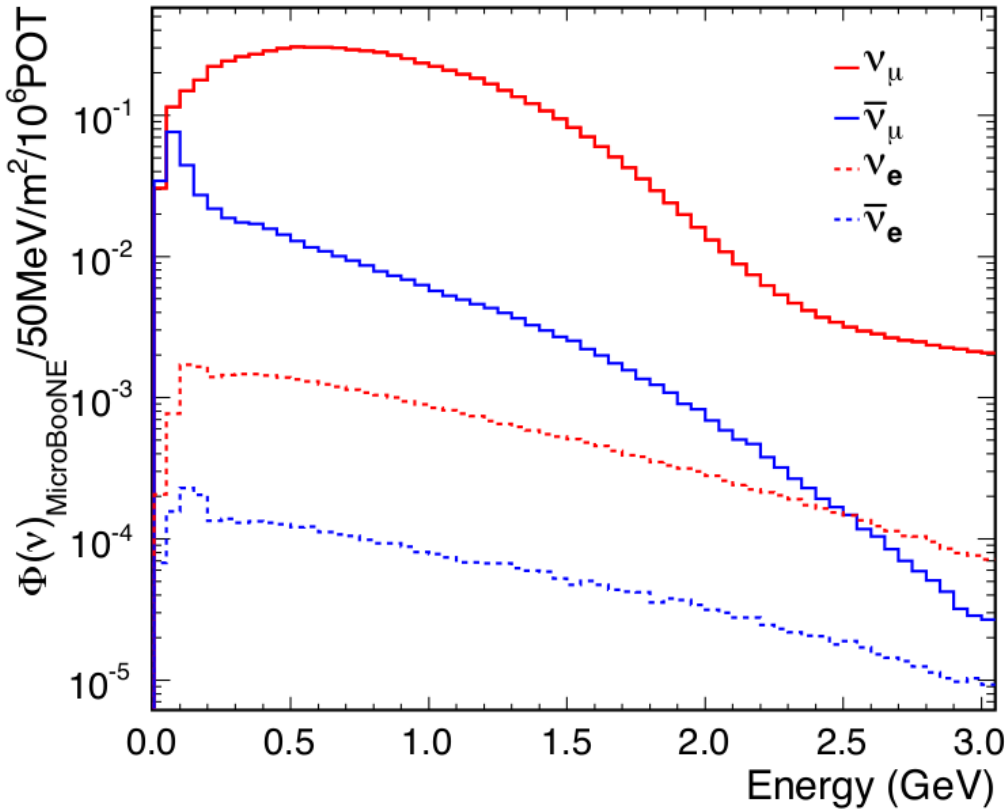


Figure 7.2: The Booster Neutrino Beam (BNB) flux at MicroBooNE.

For the ν_μ in the beam, the breakdown of ν_μ production parentage as a function of neutrino energy is shown in Figure 7.3. The two peaks in the K^+ curve (red) at neutrino energies below 0.3 GeV E_ν are from two- and three-body K^+ decays at rest. In the energy region $E_{\nu_\mu} < 2$ GeV, most ν_μ come from π^+ decay, whereas at higher energies most ν_μ come from K^+ decay. Therefore, the strategy to measure K^+ production in the beam is to select high energy ν_μ interactions and compare simulation to data in terms of event rates in order to compute a normalization factor with an uncertainty.

1702

In the initial MiniBooNE publications, the systematic uncertainty on the intrinsic ν_e from K^+ decay in the beam was 40%. This systematic came from several sources in the beam simulation process including proton delivery/optics, secondary particle productions, hadronic interactions in the target or horn, and horn magnetic field. In contrast to kaon

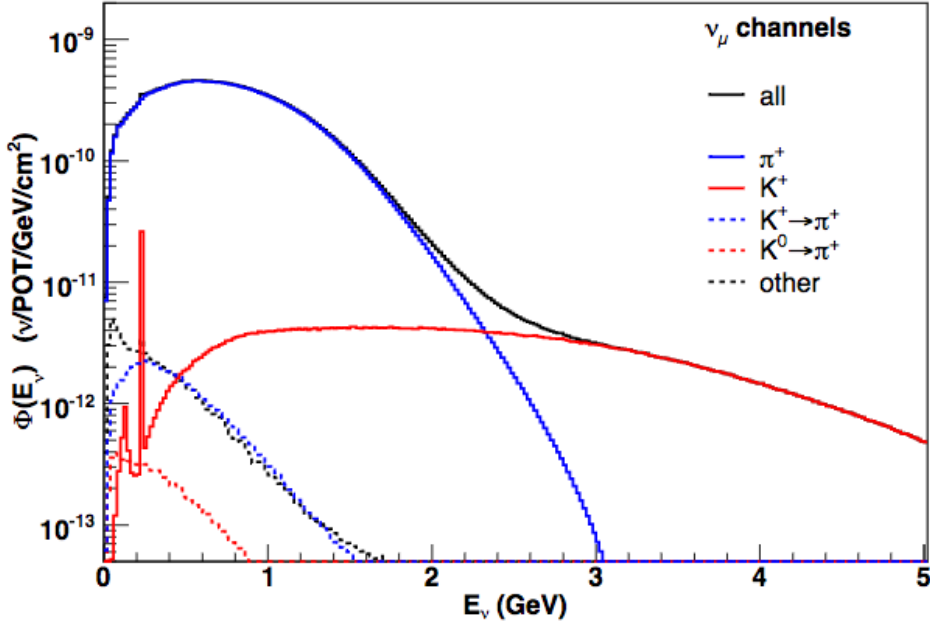


Figure 7.3: The beam ν_μ parentage as a function of true neutrino energy.

1707 production, the uncertainty for pion production is small since it was determined from spline
 1708 fits to external HARP pion double differential cross section data using the Sanford-Wang
 1709 (SW) parametrization [32] [13]. There was no published external data for K^+ production
 1710 at the BNB primary proton beam energy of 8 GeV, so the Feynman scaling hypothesis
 1711 was used to extrapolate K^+ production measurements to this energy [15]. Following a
 1712 measurement by the SciBooNE collaboration [16], the uncertainty on intrinsic ν_e from K^+
 1713 decay was reduced to 14%. Even with this drastic reduction, K^+ production is still the
 1714 largest source of uncertainty for BNB ν_e interactions above neutrino energies of around 0.6
 1715 GeV. With the SciBooNE result incorporated into the estimation of flux systematics, the
 1716 fractional error on the ν_μ flux in MicroBooNE is shown in Figure 7.4, and the fractional
 1717 error on the ν_e flux (relevant for the low energy excess search) is shown in Figure 7.5.
 1718

1719 The analysis described in the following sections aims to measure the K^+ production
 1720 in the beam-line by using the rate of very high energy ν_μ interactions in the MicroBooNE

¹⁷²¹ detector.

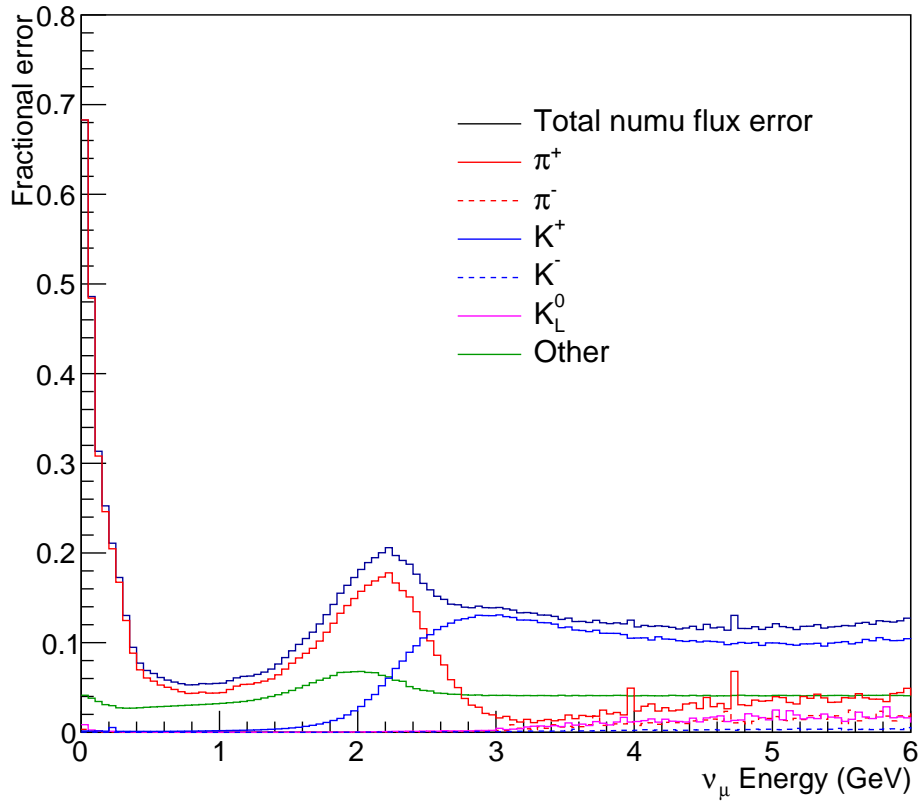


Figure 7.4: The fractional error for the BNB ν_μ flux through MicroBooNE, broken up by systematic source. “Other” includes hadronic interactions, horn current uncertainty, skin depth effects, etc. The production uncertainties are divided by neutrino parent. Note the largest uncertainty at higher ν_μ energies still comes from K^+ production, even including the SciBooNE measurement.

¹⁷²² 7.2 Event Selection

¹⁷²³ The topologies of interest for this analysis are charge-current ν_μ interactions in the Mi-
¹⁷²⁴ croBooNE TPC. In such interactions, a ν_μ interacts with a nucleon in an argon atom,
¹⁷²⁵ exchanging a charged boson. Which particles exit the interaction depend on interaction

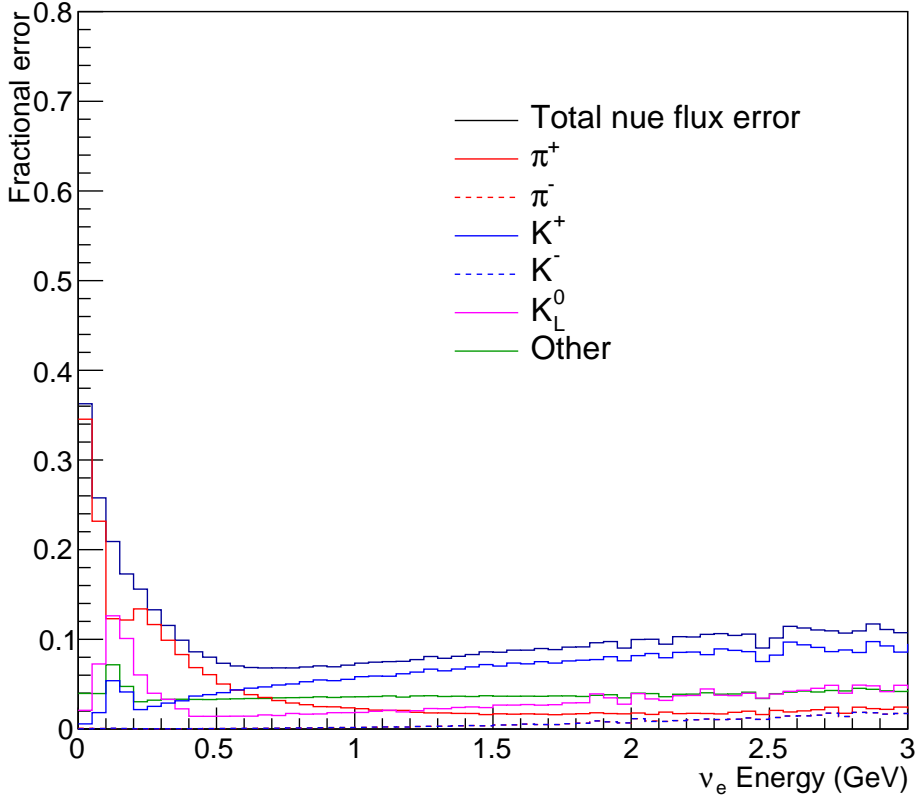


Figure 7.5: The fractional error for the BNB ν_e flux through MicroBooNE, broken up by systematic source. “Other” includes hadronic interactions, horn current uncertainty, skin depth effects, etc. The production uncertainties are divided by neutrino parent. Note the largest uncertainty for ν_e above about 0.5 GeV neutrino energy still comes from K^+ production, even including the SciBooNE measurement.

channel and final state interactions, but in general these events have a muon in the final state. The relative probability of interaction type (quasi-elastic *QE*, resonant production *RES*, or deep inelastic scattering *DIS*) can be inferred from Figure 7.6. While most ν_μ interactions in the dominant BNB energy region peaked at 0.7 GeV are quasi-elastic in nature, resonant production and deep inelastic scattering become more probable at higher neutrino energies.

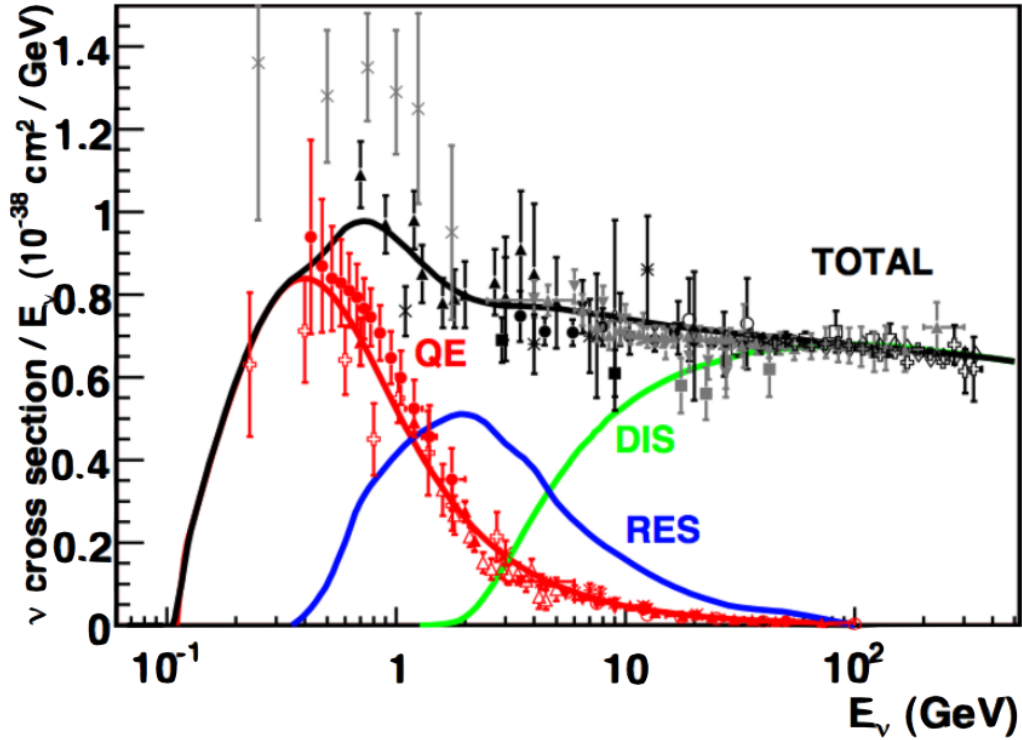


Figure 7.6: Muon neutrino charged-current cross section measurements and predictions as a function of neutrino energy. QE stands for quasielastic channels, RES stands for resonant channels, and DIS stands for deep inelastic scattering channels.

1733 The strategy is to select ν_μ interaction events in MicroBooNE, reconstruct the neutrino
 1734 energy, and then place a minimum energy cut to obtain a pure sample of ν_μ events origi-
 1735 nating from kaon decay in the beam-line. The interaction reconstruction, selection criteria,
 1736 and neutrino energy definition are described in the following subsections.

1737 7.2.1 Track Reconstruction

1738 This section provides a brief overview of how particles traversing the detector medium are
 1739 physically observed and are reconstructed in software. For a thorough description of the
 1740 MicroBooNE detector, see Section 3.

1741

1742 In a ν_μ^{CC} (charge current) interaction, a muon exits the interaction vertex. This particle

1743 leaves a trail of ionization electrons that create a relatively straight-line pattern in three di-
 1744 mensions. This line of ionization electrons is referred to as a track. Other relevant particles
 1745 traversing liquid argon that create tracks are protons and charged pions. These ionization
 1746 electrons are drifted by an external electric field past three anode wire planes, each with a
 1747 different angle with respect to the vertical (-60 degrees, 0 degrees, and +60 degrees). There
 1748 is a 3 mm spacing between each plane, and a 3 mm pitch between each wire. Scintillation
 1749 light from the particle is observed by photomultiplier tubes (PMTs) situated behind the
 1750 anode wire planes. The signals observed on each wire plane provides a 2D image of the
 1751 particle track, and combining information across multiple planes allows for a complete 3D
 1752 reconstruction, though there is ambiguity for the absolute location along the drift coordi-
 1753 nate. Matching the timing of PMT signals with that of wire signals from a track clarifies
 1754 this ambiguity, resulting in fully 3-dimensional reconstructed tracks.

1755

1756 The pattern recognition software used in this analysis to convert detector signals to
 1757 reconstructed 3D tracks is named Pandora [33]. This package is responsible for taking re-
 1758 constructed wire signals in a triggered MicroBooNE event, clustering them on each plane
 1759 (with clusters representing individual particles in the event), and matching those clusters
 1760 across planes to create 3D objects. In general, event reconstruction in a LArTPC is a
 1761 difficult problem which the MicroBooNE collaboration is currently working to solve. The
 1762 Pandora package is a complex one which consists of a large number of nested algorithms
 1763 designed to perform pattern recognition tasks, and these algorithms are not limited only to
 1764 LArTPCs.

1765

1766 The output of the Pandora package that is relevant for this analysis are 3D recon-
 1767 structed tracks created by Pandora's Projection Matching Algorithm (PMA), as well as 3D
 1768 reconstructed interaction vertices which represent candidate neutrino interaction locations.
 1769 Since ν_μ^{CC} interactions always include a muon track exiting an interaction vertex, this is
 1770 the fundamental criteria to select a sample of these CC events. More detailed criteria are
 1771 needed to mitigate backgrounds, and the selection cuts are described in more detail in the
 1772 following section.

¹⁷⁷³ **7.2.2 Selection Criteria**

¹⁷⁷⁴ The following selection criteria are placed on the reconstructed objects to select ν_μ charged-
¹⁷⁷⁵ current interactions in which a candidate muon track exits the interaction vertex:

- ¹⁷⁷⁶ 1. The event must have at least one bright (50 photoelectrons equivalent) optical flash, re-
¹⁷⁷⁷ constructed from PMT timing signals, in coincidence with the expected BNB-neutrino
¹⁷⁷⁸ arrival time.
- ¹⁷⁷⁹ 2. The z coordinate of the optical flash, as determined by the pulse height and timing
¹⁷⁸⁰ of signals in the 32 PMTs, must be within 70 cm of any point on the z projection of
¹⁷⁸¹ the candidate muon track.
- ¹⁷⁸² 3. Two or more reconstructed tracks must originate from the same reconstructed vertex
¹⁷⁸³ within the fiducial volume.
- ¹⁷⁸⁴ 4. For events with exactly two tracks originating from the vertex, additional calorimetric
¹⁷⁸⁵ criteria are applied to mitigate backgrounds from cosmic muons that arrive in time
¹⁷⁸⁶ with the passage of the beam, then stop and decay to an electron that is reconstructed
¹⁷⁸⁷ as a track.
- ¹⁷⁸⁸ 5. The length of the longest track associated with the interaction must be at least 15
¹⁷⁸⁹ centimeters in length.
- ¹⁷⁹⁰ 6. For events with exactly two tracks originating from the same reconstructed vertex,
¹⁷⁹¹ they must not have exactly opposite directions (to within 5 degrees).

¹⁷⁹² Selection criteria (1) and (2) are necessary to mitigate backgrounds originating from
¹⁷⁹³ cosmic rays arriving in coincidence with the expected beam-neutrino arrival time and trig-
¹⁷⁹⁴ gering a readout.

¹⁷⁹⁵
¹⁷⁹⁶ Selection criteria (3) is necessary to mitigate cosmic backgrounds. Cosmics entering
¹⁷⁹⁷ from outside of the TPC will often lead to reconstructed neutrino vertices very close to the
¹⁷⁹⁸ TPC boundaries. The boundaries of the fiducial volume used in this analysis are set back
¹⁷⁹⁹ from the six faces of the active volume by distances of between 20 and 37 cm, depending on

1800 the face. This volume was also chosen to reduce the impact of electric-field non-uniformities
 1801 near the edges of the TPC [34], which are relevant when reconstructing a track energy (de-
 1802 scribed in the next section). The fiducial volume corresponds to a mass of 55 tons.

1803

1804 Selection criteria (3) is also necessary to address mis-identifications stemming from track
 1805 reconstruction failures. There exists a sizable background in which a cosmic traverses the
 1806 entire detector, but only a portion of its track gets reconstructed, mimicking the one-track
 1807 topology. These one-track events are removed at the cost of ν_μ^{CCQE} interactions in which
 1808 only a muon exits the interaction vertex. Given that this analysis is geared towards the
 1809 highest energy ν_μ interactions which are often in the RES or DIS channel (multi-track),
 1810 this cut doesn't remove many high neutrino energy signal events.

1811

1812 Selection criteria (4) is necessary to remove the specific topology where a cosmic ray
 1813 muon stops in the detector (with an increased ionization rate as it approaches its endpoint,
 1814 known as a Bragg peak) and subsequently decays into an electron. This topology has two
 1815 tracks exiting a “kink”, which mimics a ν_μ^{CC} topology. This cut leverages the presence of
 1816 the Bragg peak to correctly identify the directions of the two tracks and therefore remove
 1817 this event from the analysis.

1818

1819 Selection criteria (5) and (6) are additional cuts to mitigate specific track reconstruction
 1820 failure modes that are present when reconstructing cosmic rays. In these failure modes, a
 1821 long straight track can be broken up and reconstructed as two or more straight tracks, with
 1822 a reconstructed vertex as the breaking point.

1823

1824 The above selection criteria serve only to select a sample of ν_μ^{CC} events, which come
 1825 from both pion and kaon decay. The efficiency to select these events these is defined as

$$\epsilon_{\nu_\mu^{CC}} = \frac{\# \text{ selected events}}{\# \text{ true } \nu_\mu^{CC} \text{ events in the fiducial volume}} \quad (7.1)$$

1826 and the purity is defined as

$$\pi_{\nu_\mu^{CC}} = \frac{\# \text{ true } \nu_\mu^{CC} \text{ correctly identified events in selected sample}}{\# \text{ selected events}}. \quad (7.2)$$

With the described selection criteria, the efficiency $\epsilon_{\nu_\mu^{CC}}$ is 27% in simulation. This efficiency is rather low because of the requirement of two reconstructed tracks exiting the interaction combined with a low track reconstruction efficiency, especially for short tracks near the vertex¹. The purity is 82%, and the primary contaminating backgrounds are those from cosmics. The backgrounds to this analysis are discussed in more detail in the following section.

7.2.3 Backgrounds

There are three main backgrounds to this ν_μ^{CC} from K^+ decay search: ν_μ^{CC} from π decay interactions, neutral current interactions, and cosmic-induced backgrounds. The ν_μ^{CC} from π decay interactions are the most dominant background and will be removed with a cut on neutrino energy, which is described in the following section.

1838

The neutral current backgrounds occur when a beam neutrino of any flavor interacts in such a way as to mimic a ν_μ^{CC} interaction. For example, a neutrino can interact with a nucleus and liberate a proton and a charged pion. In this case, the charged pion may be mis-identified as a muon.

1843

The cosmic-induced backgrounds are mitigated largely by the previously described event selection cuts. Their topologies are usually caused either by track reconstruction failures, or by stopping muons which decay into electrons. In the latter example, the track direction of the muon must be incorrect, and the decay electron must be reconstructed as a separate track. Though many calorimetric and track-length based selection criteria are used to reduce this background, it still persists because the rate of stopping cosmics in triggered readouts far outweighs that of ν_μ^{CC} interactions.

1851

With the events selected, the next step is to reconstruct the neutrino energy. This is

¹For this track reconstruction algorithm, the efficiency to reconstruct the muon in a ν_μ^{CC} interaction is on the order of 80% for muons with momenta above 0.4 GeV, sharply decreasing to 30% for muons with momenta around 0.1 GeV.

1853 necessary because the neutrino energy is the variable through which the ν_μ from K^+ decay
1854 sample of interest is isolated.

1855 **7.3 Neutrino Energy Reconstruction**

1856 Event selection (Section 7.2.2) provides a sample of candidate ν_μ^{CC} interactions consisting
1857 of a number (> 2) of reconstructed tracks exiting a common neutrino interaction vertex.
1858 Each track must first be associated with a particle identity (referred to as PID) in order
1859 to compute the energy of that track. Note that in $\nu_\mu^{CC}\pi^0$ interactions there will also be
1860 two showers exiting the vertex from the neutral pion decay. However, these showers (and
1861 therefore their associated energy) are ignored. The reason for this is that at the time of
1862 this analysis, the shower reconstruction performance in MicroBooNE software isn't at an
1863 adequate level to include them. Excluding them will ultimately worsen the energy recon-
1864 struction performance, but the performance is still sufficient to select a pure sample of ν_μ^{CC}
1865 interactions from K^+ decay, as will be shown later.

1866

1867 The longest track associated with the interaction is assumed to be the muon, which is
1868 reasonable because on average around half of the neutrino energy in a ν_μ^{CC} interaction is
1869 transferred to the outgoing muon, as shown in Figure 7.7. Also, muons are in general closer
1870 to minimally ionizing than to other final state particles like protons and therefore produce
1871 longer tracks.

1872

1873 The remaining tracks exiting the interaction are classified as either charged pions, or
1874 protons. This is reasonable because only one muon can exit a ν_μ^{CC} interaction vertex (bar-
1875 ring negligibly rare topologies in which a charged pion is created and decays within the
1876 nucleus, resulting in two muons in the final state). Protons are much more highly ionizing
1877 than charged pions, and therefore the measured dE/dx of the tracks are used in classifica-
1878 tion; shorter, highly ionizing tracks are tagged as protons, and longer, lower ionizing tracks
1879 are tagged as charged pions.

1880

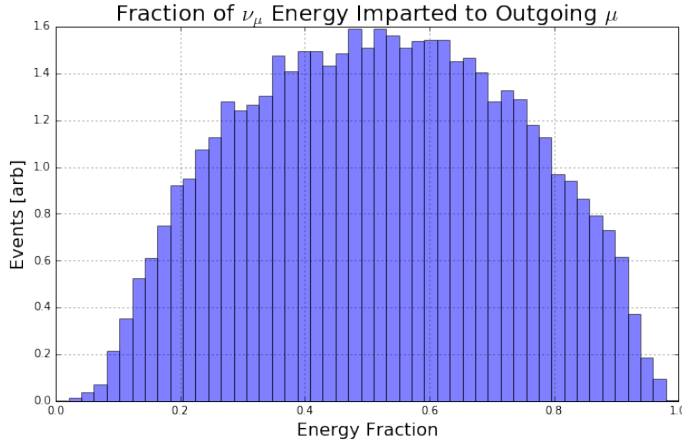


Figure 7.7: The fraction of ν_μ energy imparted to the outgoing lepton (μ) in ν_μ^{CC} interactions.

1881 The reconstructed neutrino energy is defined as the sum of the energies of all tracks
 1882 exiting the interaction vertex. For muon and pion tracks, their total energies are added
 1883 (including mass), while for proton tracks only the kinetic energy is added. This is because
 1884 while the muons and pions are created with energy directly from the neutrino, the neutrino
 1885 is scattering off of a nucleon (n or p) and is producing a nucleon (p or n). Since neutrons and
 1886 protons have very similar masses, one doesn't need to include the outgoing nucleon mass
 1887 in the energy calculations. This simplistic energy definition also neglects binding energy in
 1888 the nucleus, but that effect is small.

1889

1890 The method used to reconstruct the energy of the muon track depends on whether that
 1891 track is fully contained in the fiducial volume. In general, reconstructing the energies of
 1892 fully contained particle tracks in a LArTPC is straightforward, either with a range-based
 1893 approach, or a calorimetric approach (since calorimetric information can be gleaned from
 1894 the size of sense-wire signals). In this analysis, range-based energy is used for fully contained
 1895 muons. The stopping power of muons in liquid argon is well described by the continuous
 1896 slowing-down approximation (CSDA) by the particle data group, and agrees with data at
 1897 the sub-percent level [35] [36]. By using a linear interpolation between points in the stop-
 1898 ping power table of ref. [36], the length of a track can be used to reconstruct the muon's

¹⁸⁹⁹ total energy with resolution better than 4% and negligible bias.

¹⁹⁰⁰

¹⁹⁰¹ For muon tracks that exit the fiducial volume (which is ultimately the case for all se-
¹⁹⁰² lected ν_μ^{CC} from K^+ decay), a different method is required to compute the track energy.
¹⁹⁰³ This method leverages a phenomenon called multiple Coulomb scattering (MCS), and the
¹⁹⁰⁴ development and characterization of this method is the subject of the next chapter and
¹⁹⁰⁵ a pending publication by the author of this thesis. The MCS energy resolution for well
¹⁹⁰⁶ reconstructed exiting muon tracks with at least one meter of their length contained in the
¹⁹⁰⁷ fiducial volume is energy dependent and on the order of 15% for muons with momenta
¹⁹⁰⁸ below 2.5 GeV/c, and on the order of 30% for muons with momenta between 2.5 and 4.0
¹⁹⁰⁹ GeV/c. A downside to the MCS method is that it requires at least a meter of track to be
¹⁹¹⁰ contained. For muons that exit with less than a meter contained, the range-based energy
¹⁹¹¹ is necessarily used, which is often a significant underestimation of the true energy. Note
¹⁹¹² that, at this point, space charge effects most predominantly located near the edges of the
¹⁹¹³ TPC are not included in this simulation. These electric-field non-uniformities have the ef-
¹⁹¹⁴ fect of bending a track, which will cause the MCS technique to underestimate the track's
¹⁹¹⁵ energy. To remove the difference between data and Monte-Carlo, all reconstructed tracks
¹⁹¹⁶ in this analysis are truncated to be contained within the fiducial volume, the dimensions of
¹⁹¹⁷ which were chosen to include a region in which the effect of electric field non-uniformities
¹⁹¹⁸ are small. This effectively converts the fiducial volume to an active volume, in which space
¹⁹¹⁹ charge effects are negligible.

¹⁹²⁰

¹⁹²¹ Charged pion tracks are treated in much the same way as muon tracks. When they are
¹⁹²² contained, range-based energy is used, and when they exit, MCS energy is used (despite the
¹⁹²³ fact that MCS energy is tuned for muons, the same method works sufficiently well for the
¹⁹²⁴ purposes of this analysis on pions). Proton tracks are in general much shorter and therefore
¹⁹²⁵ their probability of exiting the fiducial volume is small. For these tracks, a range-based
¹⁹²⁶ energy is used based on the stopping power of protons in liquid argon published by the
¹⁹²⁷ same aforementioned references.

¹⁹²⁸

Given the described event selection criteria, particle identification techniques, and track energy methods, a distribution of the reconstructed neutrino energy versus true neutrino energy for a sample of correctly identified ν_μ^{CC} interactions in MicroBooNE simulation is shown in Figure 7.8. It can be seen that the reconstructed energy tends to be an underestimation of the true energy. This is caused by the failure to include shower-based energy from the interaction (as mentioned previously), as well as needing to use range-based energy for tracks which have less than one meter contained in the TPC. While this reconstructed neutrino energy could be improved upon, its performance is sufficient for this analysis. As you can see from the figure, placing a cut on reconstructed neutrino energy at around 2.5 GeV will provide a relatively pure sample of events in which the true neutrino energy is also above 2.5 GeV.

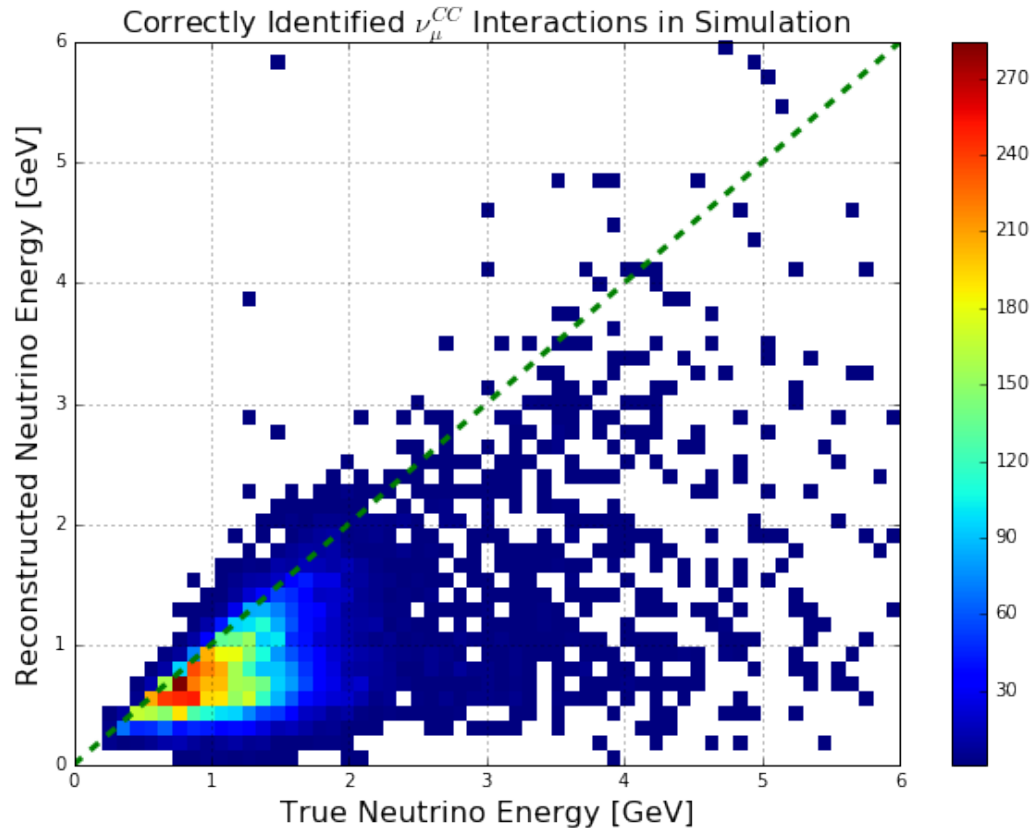


Figure 7.8: Reconstructed neutrino energy versus true neutrino energy for a sample of correctly identified BNB ν_μ^{CC} interactions in the MicroBooNE TPC.

¹⁹⁴⁰ **7.4 Results in Simulation**

¹⁹⁴¹ The simulation used for this analysis consists of BNB simulated neutrino interactions within
¹⁹⁴² the entire MicroBooNE TPC. The BNB flux is described in Chapter 4 of this thesis. The
¹⁹⁴³ neutrino interaction event generator used is GENIE [25]. These interactions also include
¹⁹⁴⁴ simulated cosmic rays by the CORSIKA package [27]. This “BNB + Cosmic” simulation
¹⁹⁴⁵ provides the measurement sample as well as all relevant backgrounds. If a reconstructed
¹⁹⁴⁶ neutrino vertex is within 3 cm of a true ν_μ^{CC} interaction vertex, that event will be classified
¹⁹⁴⁷ as either ν_μ from pion decay (background) or ν_μ from kaon decay (signal), depending on
¹⁹⁴⁸ the true neutrino parent. If the reconstructed neutrino vertex is within 3 cm of a true ν_x^{NC}
¹⁹⁴⁹ interaction vertex, that event is classified as a neutral current background. Lastly, if the re-
¹⁹⁵⁰ constructed neutrino vertex is not near any true neutrino interaction point, the interaction
¹⁹⁵¹ is classified as cosmic.

¹⁹⁵²
¹⁹⁵³ 2.2×10^{20} protons-on-target are simulated in this analysis, and the final histograms are
¹⁹⁵⁴ renormalized to 0.5×10^{20} . This scaling is done because when a comparison to data is made
¹⁹⁵⁵ (in the next section), only 0.5×10^{20} protons-on-target worth of data are available for this
¹⁹⁵⁶ analysis due to the blinding requirements imposed within the MicroBooNE collaboration.
¹⁹⁵⁷ Note that the nominal amount of protons-on-target scheduled to be delivered to Micro-
¹⁹⁵⁸ BooNE over a three-year running period is much more than this, 6.6×10^{20} ; unblinding the
¹⁹⁵⁹ full data set in the future will improve the strength of this analysis’ result by decreasing
¹⁹⁶⁰ the statistical uncertainty. At the time this thesis was written, MicroBooNE has accrued
¹⁹⁶¹ roughly 80% of the expected protons-on-target, corresponding to 5.3×10^{20} .

¹⁹⁶²
¹⁹⁶³ The distribution of simulated signal and backgrounds as a function of reconstructed
¹⁹⁶⁴ neutrino energy between 0 and 2.5 GeV (which is referred to as the sideband region for this
¹⁹⁶⁵ analysis, and contains 98.8% of all selected events are contained in this region, though very
¹⁹⁶⁶ few neutrinos from kaon decay) in Figure 7.9. In this stacked histogram figure, the green
¹⁹⁶⁷ histogram represents ν_μ^{CC} interactions from kaon decay, which is the signal of interest. In
¹⁹⁶⁸ this sideband region the ν_μ^{CC} from pion decay (blue) is the dominant background, while
¹⁹⁶⁹ cosmic-induced backgrounds (red) are mostly relevant at reconstructed neutrino energies

below 1 GeV. Neutral current backgrounds (yellow) are sub-dominant.

1970

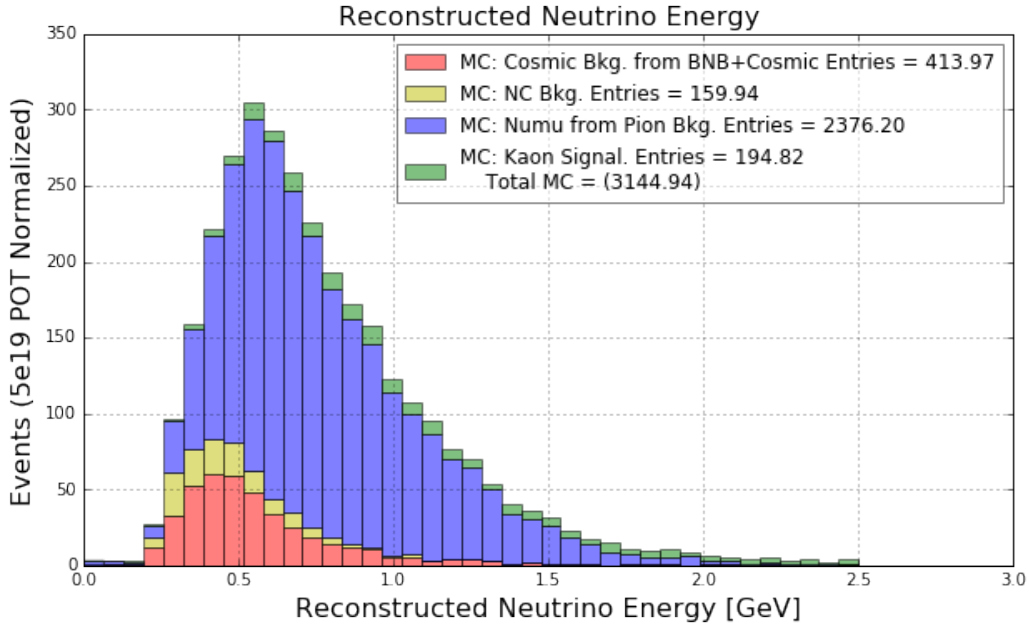


Figure 7.9: *Distribution of signal (green) and backgrounds normalized for 0.5×10^{20} protons-on-target worth of data, for reconstructed neutrino energy below 2.5 GeV. This comprises the sideband region.*

1971
1972 In order to select a relatively pure sample of ν_μ^{CC} from K^+ decay interactions, a cut on
1973 reconstructed neutrino energy is placed at 2.5 GeV. The resulting sample has a kaon signal
1974 purity of 81%, and is shown in Figure 7.10. In this region, the backgrounds from neutral
1975 current interactions and from ν_μ^{CC} from π decay are drastically suppressed. Still remaining is
1976 a cosmic-induced background which comprises 15% of the sample. The correlation between
1977 energy and angle of all kaons which decay to produce ν_μ^{CC} interactions in the fiducial volume
1978 is shown in Figure 7.11, and the subset of those which are reconstructed and selected in this
1979 analysis to pass the 2.5 GeV cut on neutrino energy are shown in Figure 7.12. The projection
1980 of these distributions onto the angle axis are shown in Figure 7.13, and onto the energy
1981 axis in Figure 7.14. The mean energy and angle information for kaons which produce ν_μ
1982 (all, and selected) and for those which produce ν_e (relevant for the electron-like low energy
1983 excess analysis) are summarized in Table 7.1. The kaons selected in the signal region tend

1984 to be skewed towards being more forward-going (smaller angle) and having higher energy,
1985 though the production phase-space is still reasonably covered by the selection (as seen by
1986 comparing Figures 7.11 and 7.12).

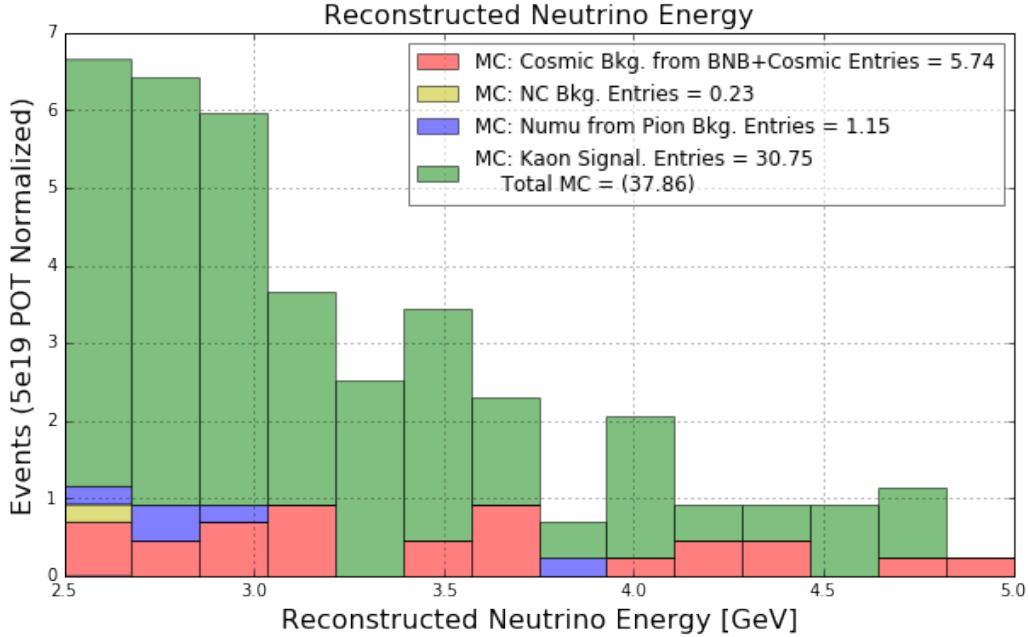


Figure 7.10: *Distribution of signal (green) and backgrounds normalized for 0.5×10^{20} protons-on-target worth of data, for reconstructed neutrino energy between 2.5 GeV and 5 GeV. This comprises the signal region, which has an 81% purity of ν_μ^{CC} interactions from K^+ decay in the beam.*

1987 7.5 Sideband Data and Simulation Comparisons

1988 As shown in the previous section, the event reconstruction and selection is able to provide a
1989 relatively pure signal sample of ν_μ^{CC} from kaon decay interactions in the detector by choos-
1990 ing those with reconstructed neutrino energy above 2.5 GeV. While the sideband region
1991 (with reconstructed neutrino energy below 2.5 GeV) is composed primarily of backgrounds
1992 from ν_μ^{CC} from π decay interactions, it is used for lower-level comparisons between data and
1993 simulation to increase confidence in results from the signal region. This section will show
1994 several such comparison plots.

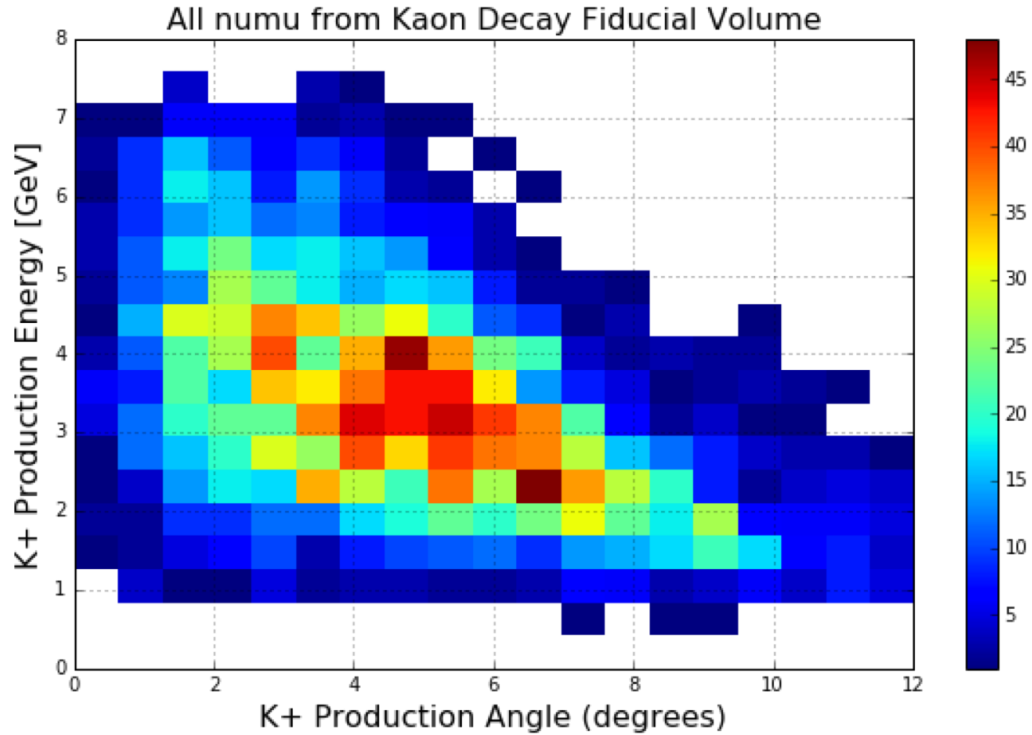


Figure 7.11: A two-dimensional plot of energy versus angle for all kaons in the beam producing ν_μ^{CC} interactions in the detector.

1995

1996 In order to compare data to simulation, there is a subtlety involving the cosmic back-
 1997 ground which needs to be taken into account. In the simulation, each triggered readout
 1998 event has a neutrino interacting somewhere within the TPC, along with several simulated
 1999 cosmic rays. However, in real data, the majority of triggers are induced by cosmic inter-
 2000 actions arriving during the expected neutrino arrival timing window ($1.6\mu s$), and do not
 2001 contain a neutrino interaction at all. To account for this, a sample of external (EXT) trig-
 2002 gered data is taken when the neutrino beam is turned off, in order to get an estimate of the
 2003 cosmic background. This “off-beam” data is then subtracted from the “on-beam” data in
 2004 the analysis, and the difference is what is directly comparable to simulation. The normal-
 2005 ization factor between “off-beam” and “on-beam” data is computed based on the number of
 2006 measured bright reconstructed optical flashes within the expected neutrino arrival window
 2007 both during “off-beam” (cosmic-only) runs and “on-beam” runs. This factor is computed

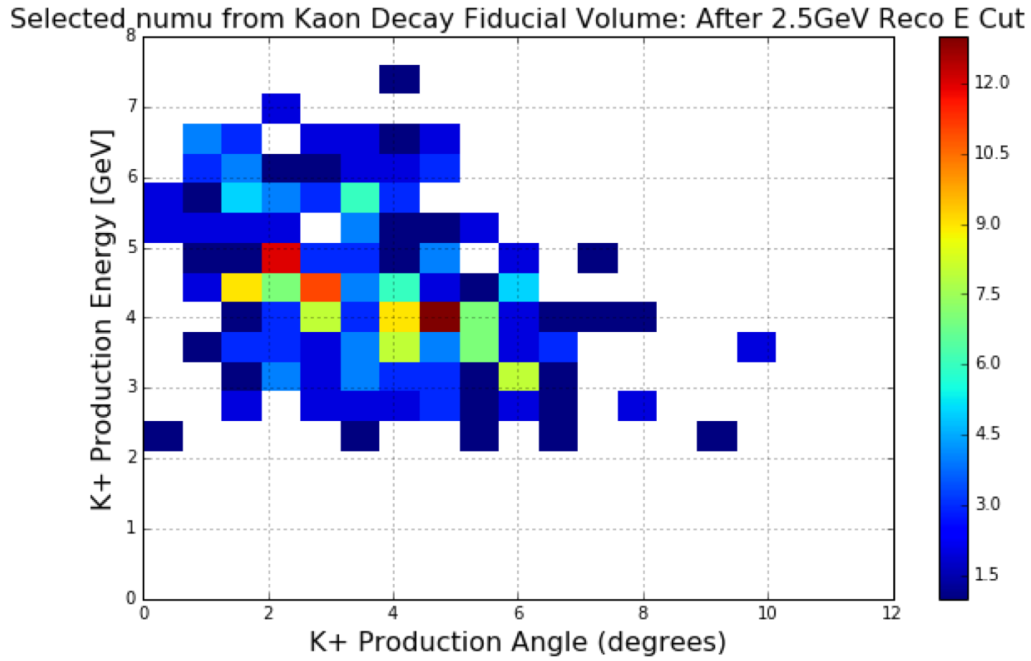


Figure 7.12: A two-dimensional plot of energy versus angle for the subset of kaons in Figure 7.11 which are reconstructed and selected for this analysis (having reconstructed neutrino energy above 2.5 GeV).

2008 to be 0.844, which means that 84% of triggered BNB readouts relevant to this analysis in
 2009 MicroBooNE data are cosmic-induced. Note that while subtracting “off-beam” data from
 2010 “on-beam” data accounts for the cosmic backgrounds not included in simulation, there still
 2011 exists a cosmic background originating from readouts which are truly triggered by a neu-
 2012 trino interaction, but with a cosmic arriving during the milliseconds-long readout window
 2013 that is mistakenly identified as the selected neutrino interaction. This is the background
 2014 shown in red in the previously shown stacked histograms (for example in Figure 7.9). In
 2015 the forthcoming data-MC comparison plots, the “off-beam” data points are shown in cyan
 2016 for reference only; the purple points are the result of their subtraction from the on-beam
 2017 data.

2018

2019 The first low level data to simulation comparison done in the sideband region is a distri-
 2020 bution of the 3D length of the muon track associated with the interaction, and is shown in

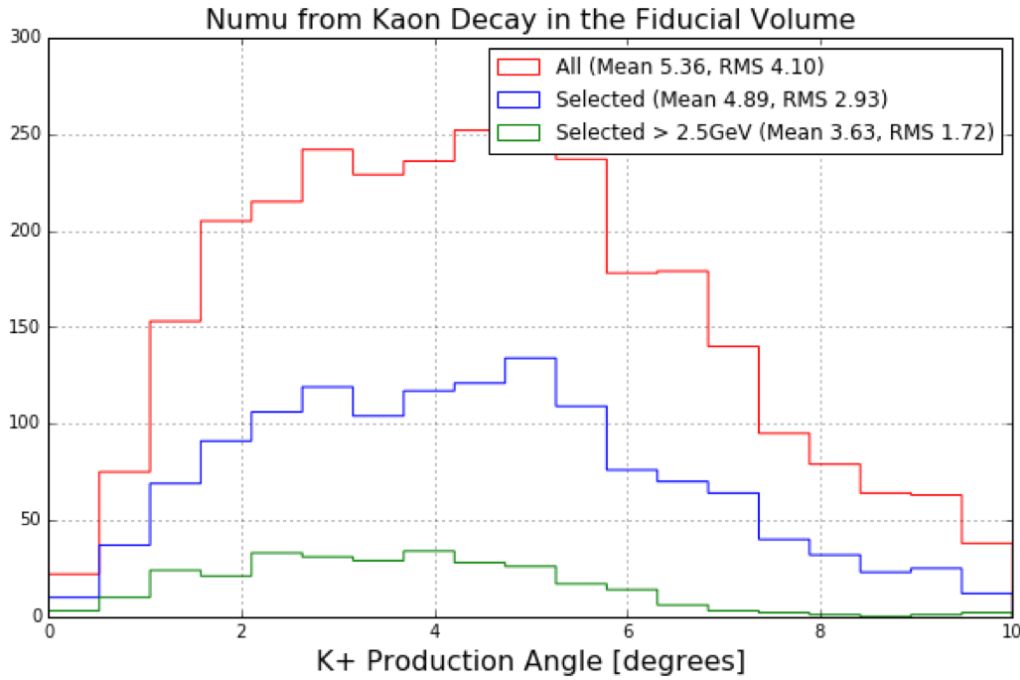


Figure 7.13: The kaon production angle distribution for all kaons in the beam producing ν_μ^{CC} interactions in the detector (red), the subset of those which are reconstructed and selected in both the sideband and signal region (blue) and the subset of those in the Kaon enriched signal sample, with reconstructed neutrino energy above 2.5 GeV (green).

2021 Figure 7.15. This plot shows the simulated background and signals as a stacked histogram
 2022 with the same color-coding as shown previously (Figure 7.9). Statistical error bars are
 2023 drawn on the purple data points, taking into account the statistical uncertainties associ-
 2024 ated with the subtraction of the “on-beam” and “off-beam” samples. Below the main figure
 2025 is a bin-by-bin ratio plot of data divided by simulation. We see a normalization difference
 2026 over the entire length range of 0 to 600 cm between data and simulation of about 8%, with
 2027 data having fewer events than expected in simulation. This normalization difference is not
 2028 flat with length; the data deficit is more prominent for longer length tracks, perhaps at-
 2029 tributable to noise sources in the detector not adequately modeled in simulation. Such noise
 2030 sources include broken or sporadically noisy anode plane sense wires that tend to prevent
 2031 the longest tracks from being fully reconstructed. The overall normalization difference in
 2032 the sideband serves as a calibration factor to be applied to the signal region.

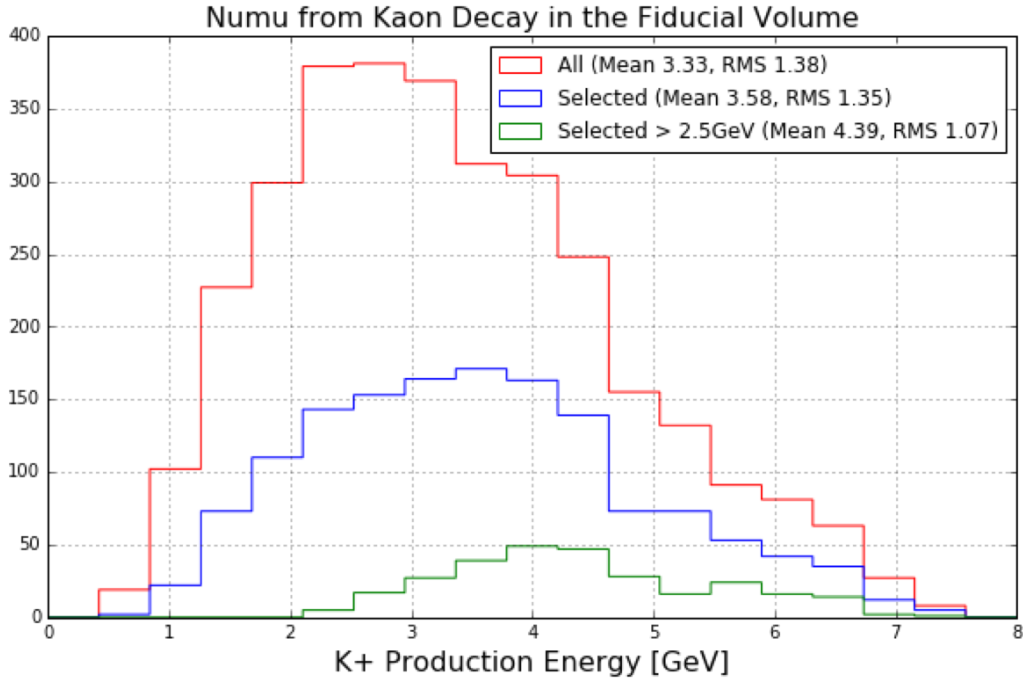


Figure 7.14: The kaon production energy distribution for all kaons in the beam producing ν_μ^{CC} interactions in the detector (red), the subset of those which are reconstructed and selected in both the sideband and signal region (blue) and the subset of those in the Kaon enriched signal sample, with reconstructed neutrino energy above 2.5 GeV (green).

2033

The next low-level data to simulation comparison in the sideband region is shown in Figure 7.16. This is the track multiplicity (the number of reconstructed tracks associated with the interaction). The same normalization offset of 8% persists, as these are the same events as in Figure 7.15. While data and simulation agree for two- and three-track events, they begin to disagree for other multiplicities. The reason for this could be imperfect modeling of nuclear interactions (including final-state intra-nuclear interactions) within the neutrino interaction simulation package.

2041

The next two data to simulation comparisons in the sideband region are shown in Figures 7.17 and 7.18. In these plots, the difference between data and simulation becomes sizable. The first plot is the ϕ angle of the muon track associated with the interaction, where ϕ is

Kaon Production Summary				
	All \bar{K}_θ [deg]	Selected \bar{K}_θ [deg]	All \bar{K}_E [GeV]	Selected \bar{K}_E [GeV]
ν_μ	5.36 [4.10]	3.63 [1.72]	3.33 [1.38]	4.39 [1.07]
ν_e	5.10 [3.68]	N/A	3.32 [1.28]	N/A

Table 7.1: *A summary of the mean kaon production angle (\bar{K}_θ) and energy (\bar{K}_E) in the BNB for ν_μ interactions (all interactions interacting within the TPC, and the subset of those which are selected in the analysis), and for ν_e interactions (providing backgrounds to the electron-like low energy excess search). Reported in brackets is the RMS of each distribution.*

measured in radians with respect to the vertical, around the beam direction. Naively the shape of this distribution should be flat, but the dips at $\pm \frac{\pi}{2}$ correspond to tracks oriented along the drift direction, which are difficult to reconstruct because of the geometry of the sense wires. These dips are well matched between data and simulation but there are big discrepancies at 0 and $\pm \pi$ radians which are not understood. The second plot is the θ angle of the muon track, measured with respect to the beam direction. A clear deficit of forward-going tracks (with small θ) can be seen in data, with an excess of vertically-oriented tracks (with $\theta \approx \frac{\pi}{2}$). This difference between data and simulation is particularly important because the high energy ν_μ^{CC} interactions which comprise the kaon-enriched signal region have generally very forward-going muons. This difference might be attributed to poor neutrino interaction kinematics by GENIE in which GENIE incorrectly models the outgoing muon angles, though there are no other analyses yet which confirm this. Additionally, the difference might be attributed to a mis-estimation of the cosmic background, since cosmic backgrounds tend to be more vertical with θ above 1 radian, where the data excess occurs. Since the off-beam subtraction technique appropriately handles all out-of-time cosmic backgrounds, this mis-estimation would apply only to events in which a neutrino triggered the readout but a cosmic was mistakenly identified as the candidate neutrino interaction. Again, no independent studies within MicroBooNE have yet indicated that this cosmic background estimation is incorrect.

2064

2065 The last low level data to simulation comparison is the computed multiple Coulomb scat-

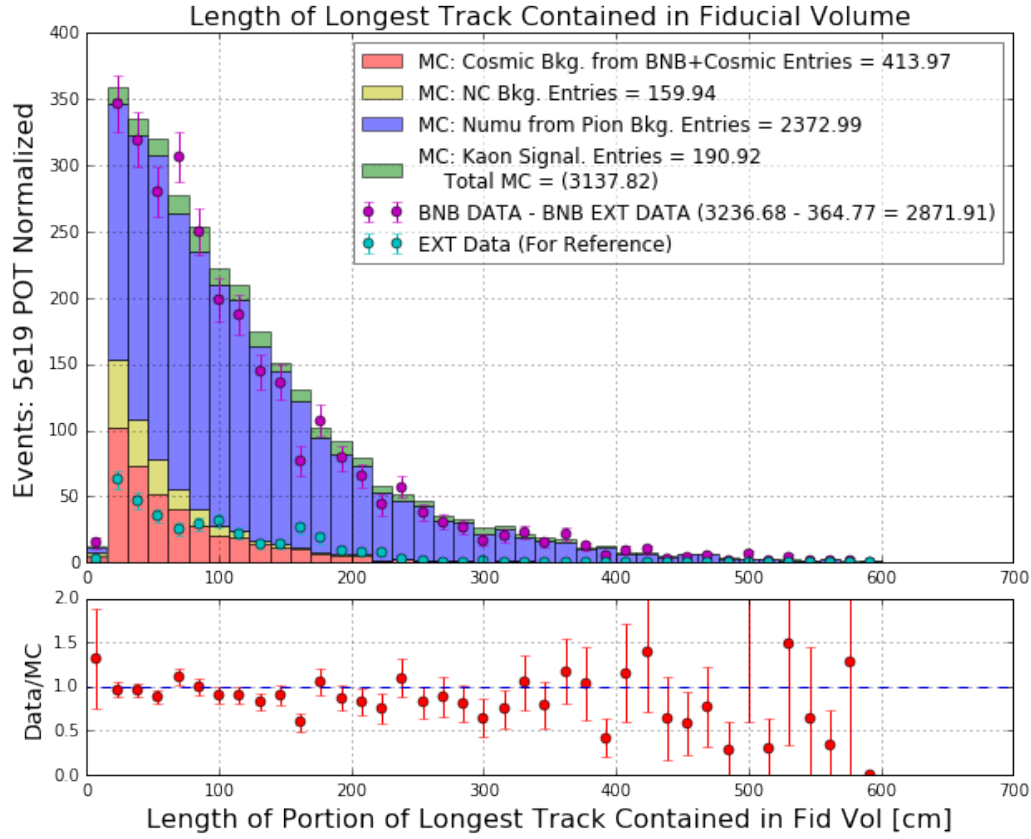


Figure 7.15: The distribution of length of the longest track associated with the interaction contained within the fiducial volume for simulated backgrounds and signal (solid histograms) overlaid with data measurements (“on-beam” minus “off-beam” drawn in purple) for the sideband region in which reconstructed neutrino energy is less than 2.5 GeV. Statistical error bars are drawn on the data points, taking into account statistics from both the “on-beam” and “off-beam” samples. Below the main figure is a bin-by-bin ratio of data divided by simulation.

tering (MCS) momentum of the muon track, and is shown in Figure 7.19. This distribution includes only tracks with at least one meter contained in the fiducial volume, as having this much track visible is necessary for the MCS technique to work. In this distribution there is a deficit of data events at higher reconstructed momenta. Since MCS momentum is a key ingredient in computing the neutrino energy (Section 7.3), and this analysis selects the highest energy events, this data to simulation disagreement is particularly important.

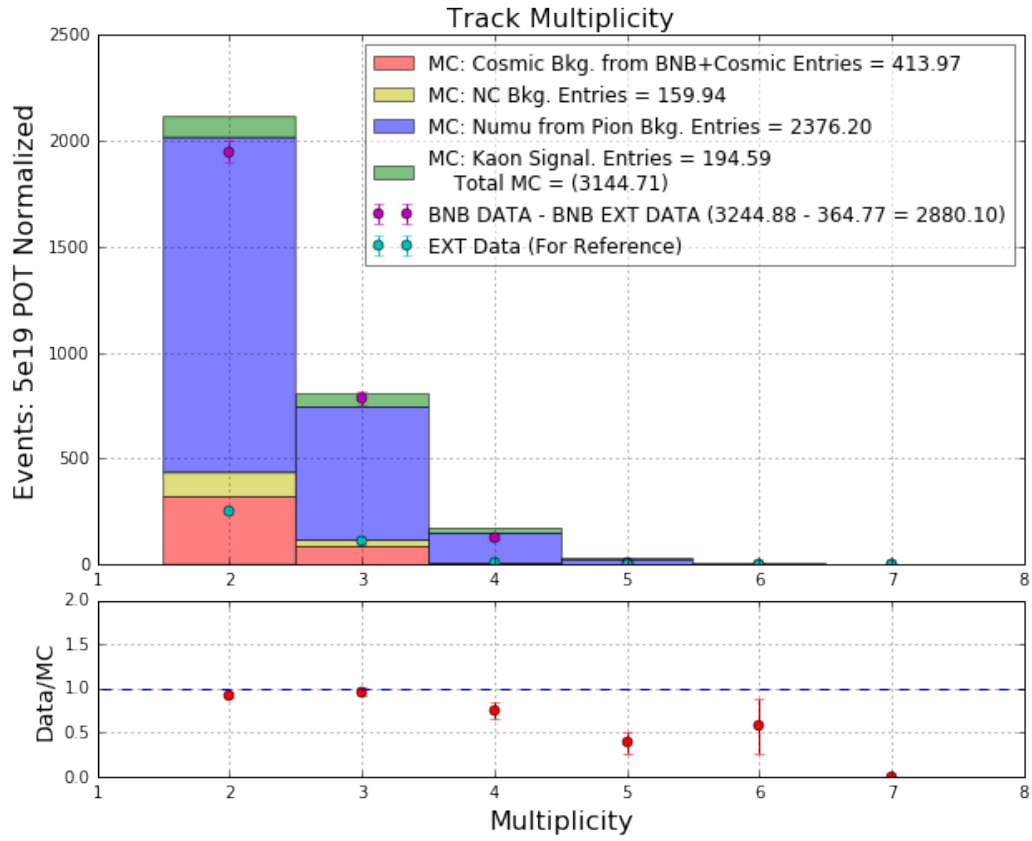


Figure 7.16: *The distribution of track multiplicity (number of tracks associated with the interaction) for simulated backgrounds and signal (solid histograms) overlaid with data measurements (“on-beam” minus “off-beam” drawn in purple) for the sideband region in which reconstructed neutrino energy is less than 2.5 GeV. Statistical error bars are drawn on the data points, taking into account statistics from both the “on-beam” and “off-beam” samples. Below the main figure is a bin-by-bin ratio of data divided by simulation.*

2072 For this reason, an extensive analysis of the MCS algorithm including data to simulation
2073 comparisons was conducted by the author of this thesis. This analysis improved the perfor-
2074 mance of the algorithm, including an important change to the underlying phenomenological
2075 formula not yet discovered by other LArTPC experiments using the MCS technique. This
2076 analysis is expected to be published in the Journal of Instrumentation, and a description of
2077 this analysis is included in Chapter 8 of this thesis. The resulting improved MCS algorithm
2078 is the one used in the analysis described in this chapter.

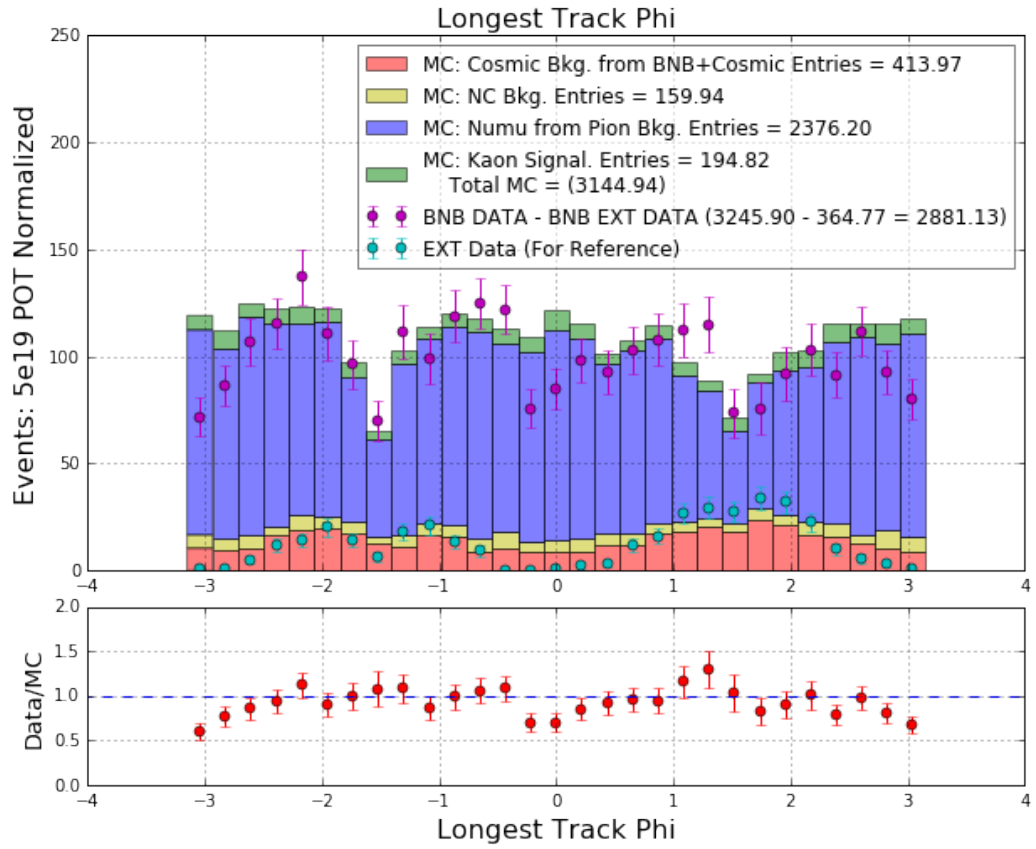


Figure 7.17: The distribution of ϕ angle (measured in radians with respect to the vertical) of the longest track associated with the interaction for simulated backgrounds and signal (solid histograms) overlaid with data measurements (“on-beam” minus “off-beam” drawn in purple) for the sideband region in which reconstructed neutrino energy is less than 2.5 GeV. Statistical error bars are drawn on the data points, taking into account statistics from both the “on-beam” and “off-beam” samples. Below the main figure is a bin-by-bin ratio of data divided by simulation.

2079

2080 Despite extensive studies to uncover the underlying causes of the data to simulation dis-
 2081 parities (for example the deficit of tracks at small θ angle in data and the systematic shift
 2082 downward in multiple Coulomb scattering energy in data) either to fix them or calibrate
 2083 them out without introducing new systematic errors, the differences remain. Since Micro-
 2084 BooNE is in part an R&D experiment paving the way for future LArTPC experiments,

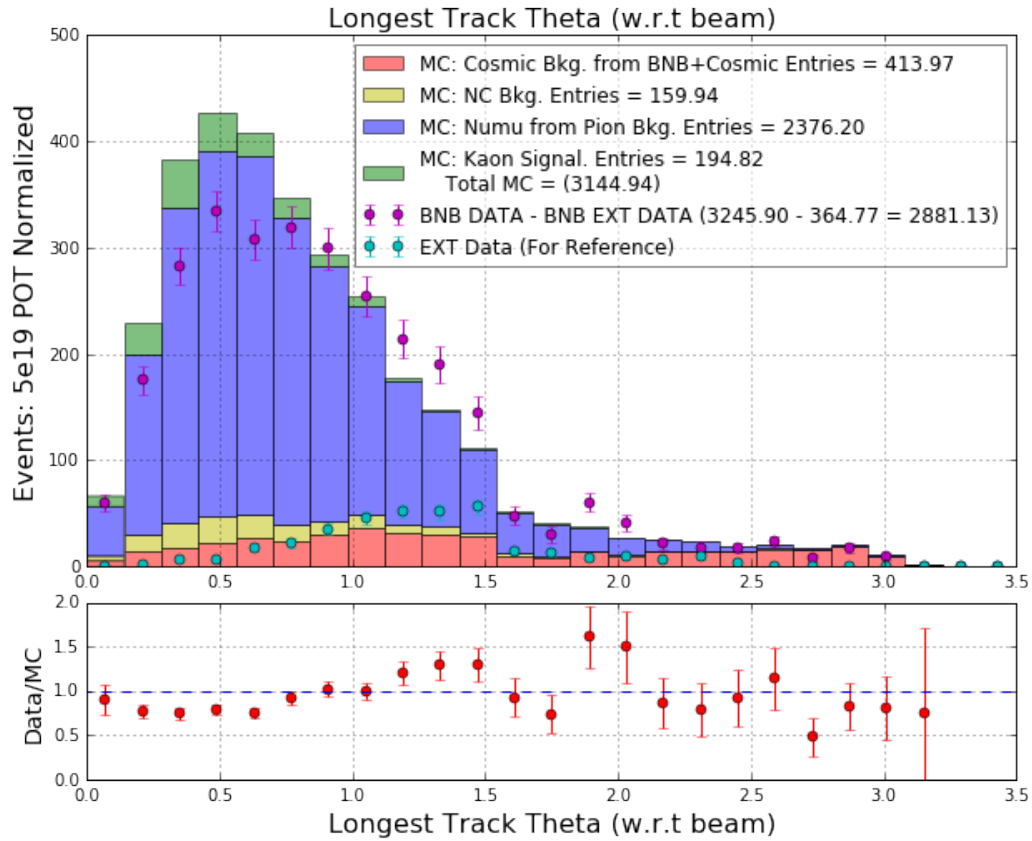


Figure 7.18: *The distribution of θ angle (measured in radians with respect to the beam direction) of the longest track associated with the interaction for simulated backgrounds and signal (solid histograms) overlaid with data measurements (“on-beam” minus “off-beam” drawn in purple) for the sideband region in which reconstructed neutrino energy is less than 2.5 GeV. Statistical error bars are drawn on the data points, taking into account statistics from both the “on-beam” and “off-beam” samples. Below the main figure is a bin-by-bin ratio of data divided by simulation.*

understanding these differences are a problem that the MicroBooNE collaboration is still working to solve.

2087

2088 The comparison of data to simulation in terms of reconstructed neutrino energy for the
2089 sideband region with $E_\nu < 2.5$ GeV is shown in Figure 7.20. Given the clear systematic
2090 shift in energy to lower values in data, any measurement coming from the signal region

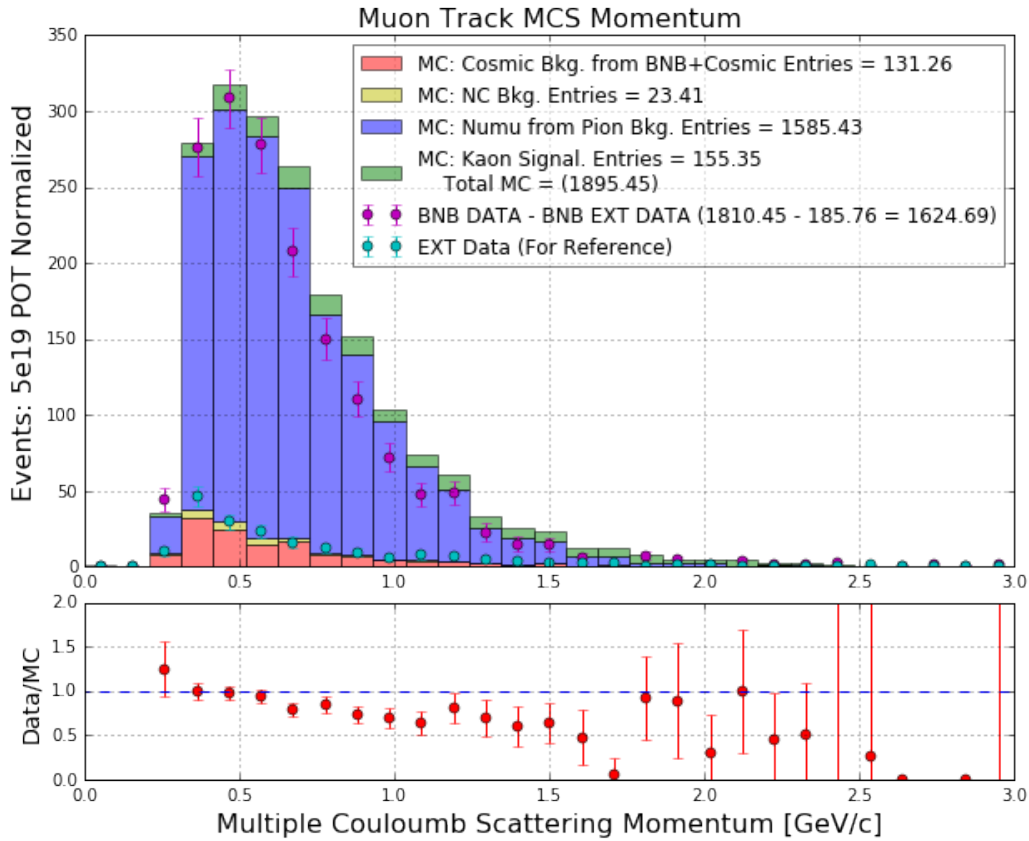


Figure 7.19: The distribution of multiple Coulomb scattering computed energy for the longest track associated with the interaction for simulated backgrounds and signal (solid histograms) overlaid with data measurements (“on-beam” minus “off-beam” drawn in purple) for the sideband region in which reconstructed neutrino energy is less than 2.5 GeV. Statistical error bars are drawn on the data points, taking into account statistics from both the “on-beam” and “off-beam” samples. Below the main figure is a bin-by-bin ratio of data divided by simulation. This plot has fewer entries than previous plots because only tracks longer than 1 meter have an associated MCS momentum as described in Section 7.3.

2091 (which is a small tail at high energies) will have an extremely large systematic uncertainty

2092 associated with it. This figure is zoomed in on reconstructed neutrino energies between 1.5

2093 GeV and 2.5 GeV in Figure 7.21.

2094

2095 For completeness, the reconstructed energy in the signal region is shown in Figure 7.22.

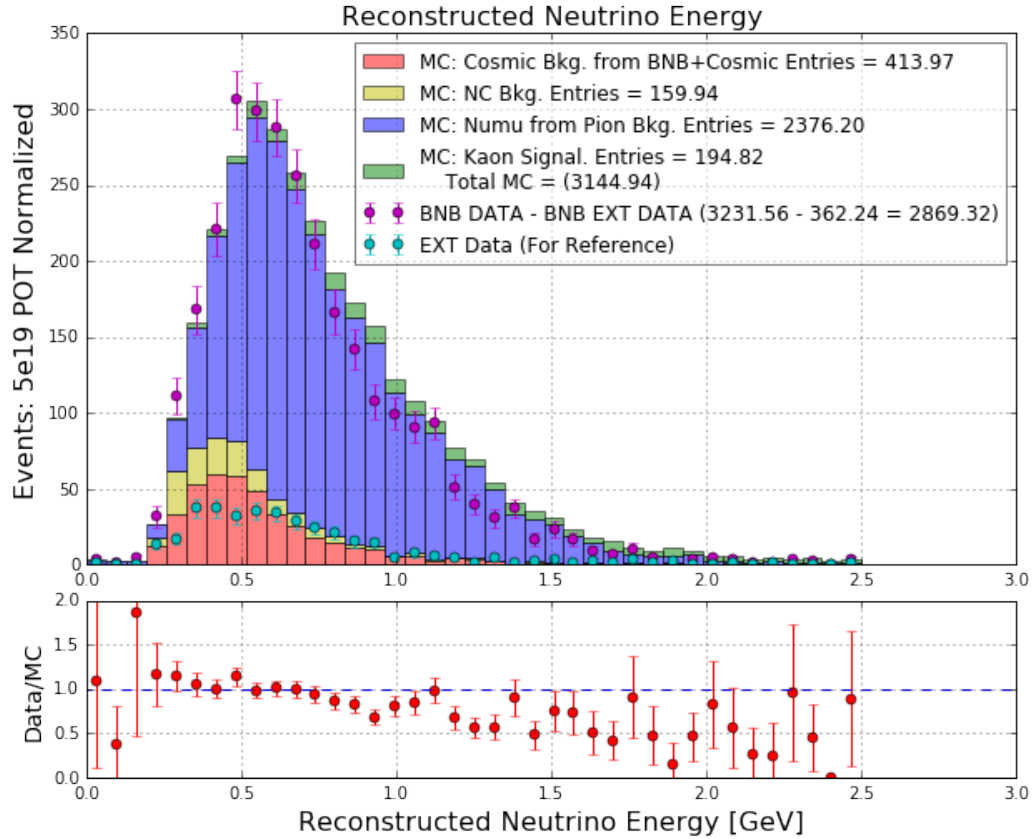


Figure 7.20: *The distribution of reconstructed neutrino energy for simulated backgrounds and signal (solid histograms) overlaid with data measurements (“on-beam” minus “off-beam” drawn in purple) for the sideband region in which reconstructed neutrino energy is less than 2.5 GeV. Statistical error bars are drawn on the data points, taking into account statistics from both the “on-beam” and “off-beam” samples. Below the main figure is a bin-by-bin ratio of data divided by simulation.*

2096 While the referenced SciBooNE result predicts the K^+ production rate in simulation is
 2097 underestimated by a factor of 0.85 ± 0.11 [16], the underestimation of data with respect
 2098 to simulation seen in this analysis is likely not indicative of incorrectly simulated kaon
 2099 production in the beam-line, but instead due to systematic detector and reconstruction
 2100 effects that have not yet been resolved.

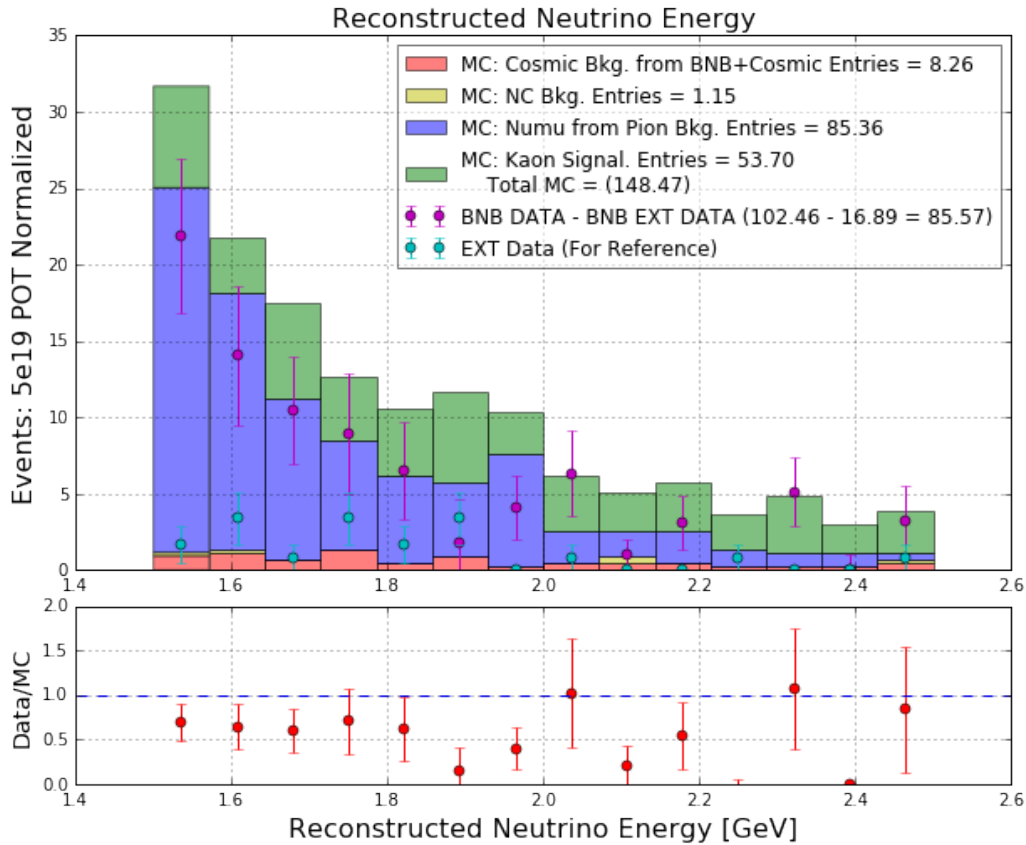


Figure 7.21: *The distribution of reconstructed neutrino energy for simulated backgrounds and signal (solid histograms) overlaid with data measurements (“on-beam” minus “off-beam” drawn in purple) for the higher-energy end of the sideband region in which reconstructed neutrino energy is between 1.5 and 2.5 GeV. Statistical error bars are drawn on the data points, taking into account statistics from both the “on-beam” and “off-beam” samples. Below the main figure is a bin-by-bin ratio of data divided by simulation.*

2101 7.6 Conclusions

2102 This thesis chapter has presented an analysis serving as an essential first step towards mea-
2103 suring the kaon production in the beam-line by MicroBooNE, an important measurement
2104 used to constrain a main intrinsic ν_e background in the electron-like low energy excess
2105 search described in Chapter 6. While a similar measurement was previously done by the
2106 SciBooNE collaboration, this MicroBooNE measurement is important because it will be

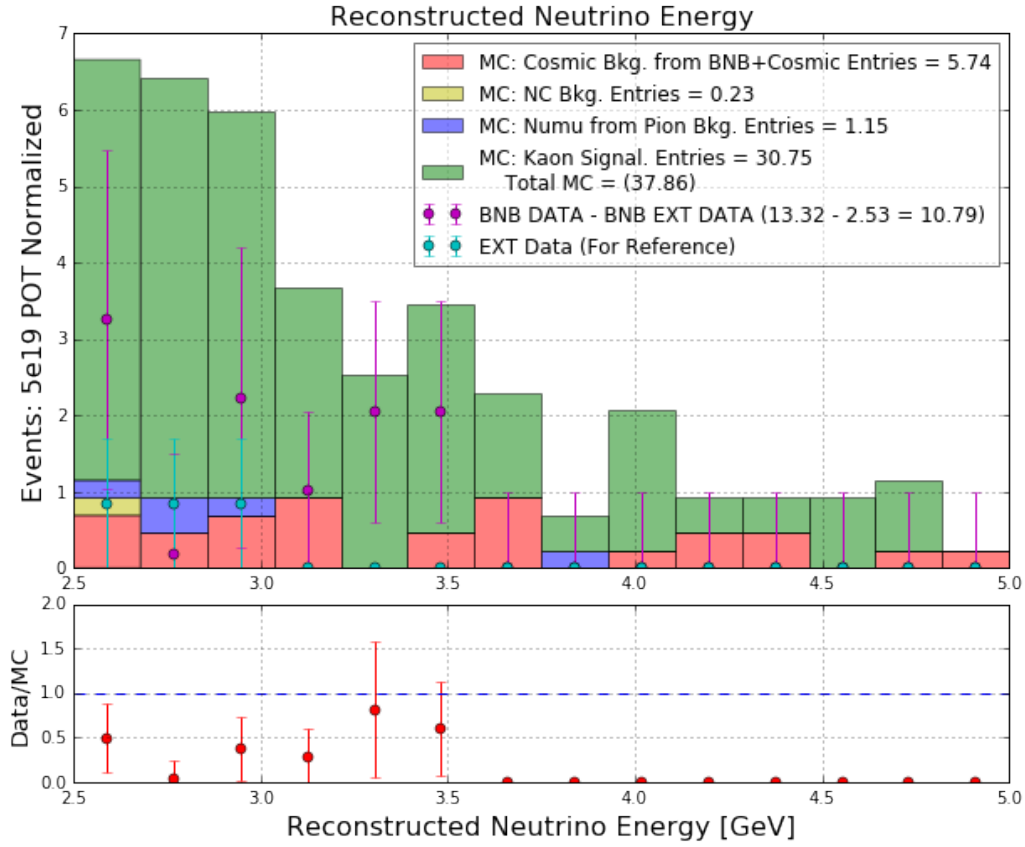


Figure 7.22: *The distribution of reconstructed neutrino energy for simulated backgrounds and signal (solid histograms) overlaid with data measurements (“on-beam” minus “off-beam” drawn in purple) for the signal region in which reconstructed neutrino energy is greater than 2.5 GeV. Statistical error bars are drawn on the data points, taking into account statistics from both the “on-beam” and “off-beam” samples. Below the main figure is a bin-by-bin ratio of data divided by simulation.*

done *in situ* with the same detector that will search for the low energy excess. The method used in this analysis is to select the highest energy ν_μ^{CC} interactions within the detector in order to obtain a pure sample of ν_μ from K^+ decay. The method was demonstrated to be viable in order to make a measurement with comparable significance as that of SciBooNE. As of now, some unresolved discrepancies between data and simulation prevent the analysis from coming to fruition. These differences are still being investigated by the MicroBooNE collaboration, and once they are understood this important analysis will proceed. Addi-

2114 tional items left to be resolved before this kaon production systematic can be estimated in
2115 MicroBooNE aside from understanding the aforementioned data to simulation discrepan-
2116 cies include more thorough estimates of detector systematics, cross-section systematics, and
2117 the unblinding of more MicroBooNE data for this analysis. All of these tasks are currently
2118 being investigated within the MicroBooNE collaboration at the time this thesis was written.

2119

2120 With respect to these data to simulation discrepancies discussed in Section 7.5 above,
2121 one of the most important discrepancies lies within the calculation of muon momentum
2122 via multiple Coulomb scattering (MCS). Since MicroBooNE has no magnetic field, this
2123 MCS momentum determination method is the only technique by which the momentum of a
2124 muon that exits the TPC can be calculated, and the muons from the high neutrino energy
2125 interactions in the kaon enriched signal sample are all exiting. A detailed study of the MCS
2126 algorithm was conducted by the author of this thesis and has been submitted for publication
2127 to the Journal of Instrumentation (JINST). The analysis and results associated with this
2128 work is presented as the following chapter of this thesis.

2129 **Chapter 8**

2130 **Multiple Coulomb Scattering**

2131 This chapter consists of a copy of an analysis recently submitted for publication by the
2132 MicroBooNE collaboration primarily authored by the thesis author which discusses in detail
2133 the algorithm used to compute the momentum of tracks in a LArTPC by means of multiple
2134 Coulomb scattering. This is a crucial part of the previously described kaon production
2135 measurement, which in turn is a crucial part of constraining the sizable intrinsic ν_e from
2136 kaon decay background in the electron-like low energy excess search. The title of the
2137 publication is “Determination of muon momentum in the MicroBooNE LArTPC using an
2138 improved model of multiple Coulomb scattering”.

2139 **8.1 Introduction and motivation**

2140 In this paper we summarize the theory of multiple Coulomb scattering (MCS) and describe
2141 how the underlying Highland formula is retuned based on Monte Carlo simulation for use
2142 in liquid-argon time-projection chambers (LArTPCs). We present a maximum likelihood
2143 based algorithm that is used to determine the momentum of particles in a LArTPC. The
2144 only way to determine the momentum of a particle that exits the active volume of a LArTPC
2145 is through MCS measurements. We demonstrate that this technique works well for a sam-
2146 ple of fully contained muons from Booster Neutrino Beam (BNB) ν_μ charged-current (CC)
2147 interactions, and determine the resolutions and biases of the measurement. In addition we
2148 demonstrate the performance of the method on simulated exiting tracks.

2149

2150 MicroBooNE (Micro Booster Neutrino Experiment) is an experiment that uses a large
2151 LArTPC to investigate the excess of low energy events observed by the MiniBooNE exper-
2152 iment [37] and to study neutrino-argon cross-sections. MicroBooNE is the first detector of
2153 the Short-Baseline Neutrino (SBN) [38] physics program at the Fermi National Accelerator
2154 Laboratory (Fermilab), to be joined by two other LArTPCs: the Short Baseline Near De-
2155 tector (SBND) and the Imaging Cosmic And Rare Underground Signal (ICARUS) detector
2156 [39]. MicroBooNE also performs important research and development in terms of detector
2157 technology and event reconstruction techniques for future LArTPC experiments including
2158 DUNE (Deep Underground Neutrino Experiment) [40].

2159

2160 The MicroBooNE detector [41] consists of a rectangular time-projection chamber (TPC)
2161 with dimensions $2.6 \text{ m} \times 2.3 \text{ m} \times 10.4 \text{ m}$ (width \times height \times length) located 470 m down-
2162 stream from the Booster Neutrino Beam (BNB) target [42]. LArTPCs allow for precise
2163 three-dimensional reconstruction of particle interactions. For later reference, the z axis of
2164 the detector is horizontal, along the direction of the BNB, while the x direction of the TPC
2165 corresponds to the drift coordinate and the y direction is the vertical direction. The mass
2166 of active liquid argon contained within the MicroBooNE TPC volume is 89 tons, out of a
2167 total mass of 170 tons.

2168

2169 A set of 32 photomultiplier tubes (PMTs) and three planes of wires with 3 mm spacing
2170 at angles of 0, and ± 60 degrees with respect to the vertical are located in the TPC for
2171 event reconstruction as shown in figure 8.1. The cathode plane operating voltage is -70 kV.
2172 A neutrino in the beam interacts with an argon nucleus and the charged outgoing particles
2173 traverse the medium, lose energy and leave an ionization trail. The resulting ionization
2174 electrons drift in a 273 V/cm electric field to the wire planes constituting the anode. The
2175 passage of these electrons through the first two wire planes induces a signal in the wires, and
2176 their collection on the third plane also generates a signal. These signals are used to create
2177 three distinct two-dimensional views (in terms of wire and time) of the event. Combining
2178 these wire signals allow for full three-dimensional reconstruction of the event, with PMT

signals providing information about the absolute drift (x) coordinate. The boundaries of the fiducial volume used in this analysis are set back from the six faces of the active volume by distances of between 20 and 37 cm, depending on the face, to reduce the impact of electric-field non-uniformities near the edges of the TPC. This volume corresponds to a mass of 55 tons.

2184

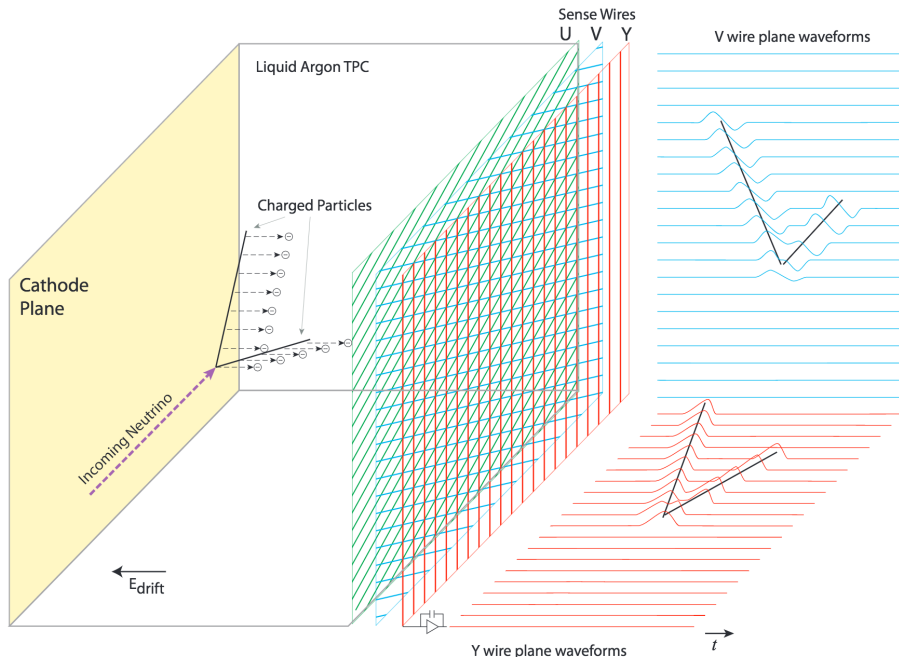


Figure 8.1: A diagram of the time projection chamber of the MicroBooNE detector. PMTs (not shown) are located behind the wire planes.

2185 The Booster Neutrino Beam (BNB) is composed predominantly of muon neutrinos (ν_μ)
 2186 with a peak neutrino energy of about 0.7 GeV. Some of these neutrinos undergo charge-
 2187 current (ν_μ CC) interactions in the TPC and produce muons and other particles. For muon
 2188 tracks that are completely contained in the TPC, we calculate the momentum with a mea-
 2189 surement of the length of the particle's track, or with calorimetric measurements which come
 2190 from wire signal size measurements. Around half of the muons from BNB ν_μ CC interactions

in MicroBooNE are not fully contained in the TPC, and therefore using a length-based or calorimetry-based method to determine the momenta for these uncontained tracks is not a possibility; the only way to determine their momenta is through MCS.

2194

2195 8.2 Multiple Coulomb scattering

2196 Multiple Coulomb scattering occurs when a charged particle traverses medium and un-
 2197 dergoes electromagnetic scattering off atomic nuclei. This scattering perturbs the original
 2198 trajectory of the particle within the material (figure 8.2). For a given initial momentum
 2199 p , the angular deflection scatters of a particle in either the x' direction or y' direction (as
 2200 indicated in the aforementioned figure) form a Gaussian distribution centered at zero with
 2201 an RMS width, σ_o^{HL} , given by the Highland formula [43][44]

$$\sigma_o^{\text{HL}} = \frac{S_2}{p\beta c} z \sqrt{\frac{\ell}{X_0}} \left[1 + \epsilon \times \ln \left(\frac{\ell}{X_0} \right) \right], \quad (8.1)$$

2202 where β is the ratio of the particle's velocity to the speed of light (assuming the particle is a
 2203 muon), ℓ is the distance traveled inside the material, z is the magnitude of the charge of the
 2204 particle (unity, for the case of muons), and X_0 is the radiation length of the target material
 2205 (taken to be a constant 14 cm in liquid argon). S_2 and ϵ are parameters determined to
 2206 be 13.6 MeV and 0.0038, respectively. In this study, a modified version of the Highland
 2207 formula is used that includes a detector-inherent angular resolution term, σ_o^{res}

$$\sigma_o = \sqrt{(\sigma_o^{\text{HL}})^2 + (\sigma_o^{\text{res}})^2}. \quad (8.2)$$

2208 For this analysis, the σ_o^{res} term is given a fixed value of 3 mrad which has been determined
 2209 to be an acceptable value based on MicroBooNE simulation studies of muons at higher mo-
 2210 menta. At 4.5 GeV/c muon momentum and $l \approx X_0$, equation 8.1 predicts an RMS angular
 2211 scatter of 3 mrad, comparable to the detector resolution. The fully contained muons ad-
 2212 dressed in this analysis have momenta below 1.5 GeV/c, making the impact of this detector
 2213 resolution minimal for that sample.

2214

With the Highland formula, the momentum of a track-like particle can be determined using only the 3D reconstructed track information, without any calorimetric or track range information. In neutrino physics experiments, emulsion detectors like the DONUT [45] and OPERA [46] Collaborations have used MCS to determine particle momenta. Additionally, the MACRO [47] Collaboration at Gran Sasso Laboratory utilized this technique. The original method for using MCS to determine particle momentum in a LArTPC used a Kalman Filter and was described by the ICARUS collaboration [48], and they more recently described another method [49]. The likelihood-based method, discussed in this paper for use in the Microboone detector and described in detail in section 8.3, has improved on the ICARUS method by tuning the underlying phenomenological formula.

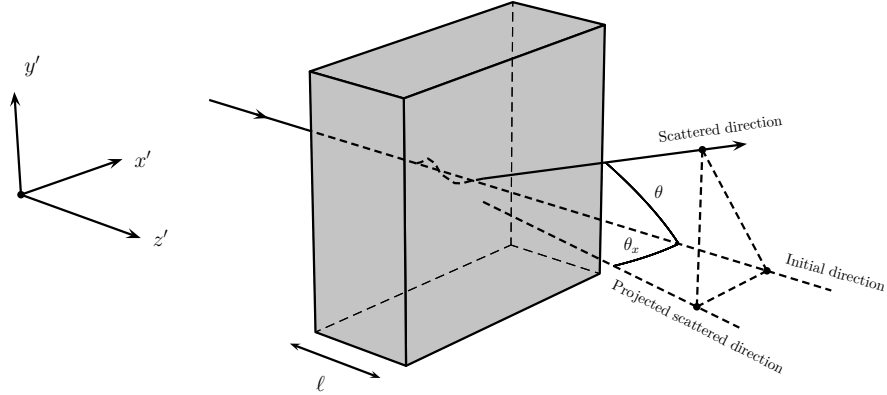


Figure 8.2: The particle’s trajectory is deflected as it traverses the material. The angular scatter in the labeled x' plane is shown as θ_x .

8.2.1 Tuning the Highland formula for argon

The Highland formula as written in equation 8.1 originates from a 1991 publication by G. R. Lynch and O. I. Dahl [44]. The parameters in the equation (S_2 and ϵ) were determined using a global fit over MCS simulated data using a modified GEANT simulation package of 14 different elements and 7 thickness ranges. All of the simulated particles were rela-

tivistic, with $\beta = 1$. The materials in which they studied scattering ranged from hydrogen (with Z=1) to uranium (with Z=92). Given that the parameters in the formula were determined from a single fit to a wide range of Z with a wide range of material thicknesses, there is reason to believe that these parameters should differ for scattering specifically in liquid argon with $l \approx X_0$. There is also reason to believe that these parameters might be momentum-dependent for particles with $\beta < 1$, which is the case for some of the contained muons in this analysis.

2237

In order to re-tune these parameters to liquid argon, a large sample of muons are simulated with GEANT4¹ [50] in the MicroBooNE TPC and their true angular scatters are used in a fit, with $l = X_0$. The reason for using $l = X_0$ is that the Highland formula simplifies to remove its dependence on ϵ

$$\sigma_o^{\text{HL}} = \frac{S_2}{p\beta c}. \quad (8.3)$$

The S_2 parameter in equation 8.3 is fit for as a function of true muon momentum at each scatter, in order to explore the β dependence of this parameter. The fitted parameter value as a function of true momentum is shown in figure 8.3.

The fitted value of S_2 is always less than the nominal 13.6 MeV for momentum greater than 0.25 GeV/c and asymptotically approaches a constant at higher momentum (where $\beta = 1$) of about 11.0 MeV. The value increases in the momentum region where $\beta < 1$. Shown in red is a fit to these data points with functional form $a \times p^{-2} + c$, with best fit values for floating parameters a and c being $0.105 \text{ MeV}^3 c^{-2}$ and 11.004 MeV respectively. This functional form is chosen because it fits the data well, and asymptotically approaches a constant value when β approaches 1. This function, used as a replacement for the S_2 parameter in the Highland formula, will henceforth be referred to as $\kappa(p)$:

$$\kappa(p) = \frac{0.105}{p^2} \text{ MeV}^3 c^{-2} + 11.004 \text{ MeV}. \quad (8.4)$$

To visualize the Highland formula for $l = X_0$ both before and after the $\kappa(p)$ replacement, see figure 8.4. It is recommended that future LArTPC experiments use this parameteriza-

¹The GEANT4 version used in this simulation is 4.9.6.

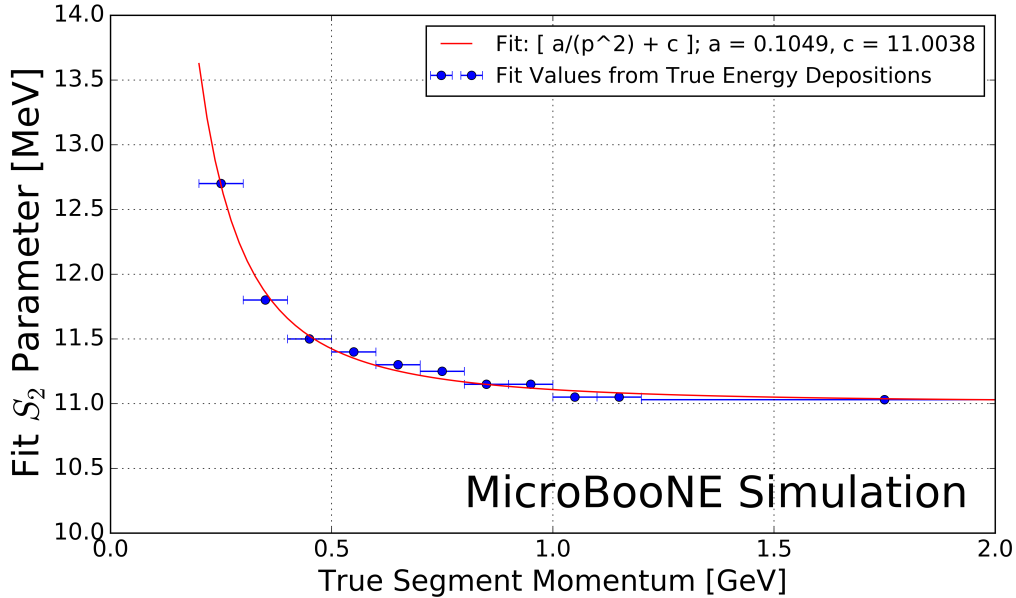


Figure 8.3: Fitted Highland parameter S_2 as a function of true segment momentum for $\ell = X_0$ simulated muons in the MicroBooNE LArTPC. Blue x- error bars indicate the true momentum bin width with data points drawn at the center of each bin. Shown in red is a fit to these data points with functional form $a \times p^{-2} + c$, with best fit values for parameters a and c shown in the legend.

2255 tion of the Highland formula, or at the very least conduct their own studies to tune the
 2256 Highland formula for scattering in argon. This formulation can also be checked in LAr-
 2257 based test-beam experiments like LArIAT [51].

2258

2259 With $\ell = X_0$, the form of the Highland equation used in this analysis is therefore

$$\sigma_o^{\text{RMS}} = \sqrt{(\sigma_o)^2 + (\sigma_o^{\text{res}})^2} = \sqrt{\left(\frac{\kappa(p)}{p\beta c}\right)^2 + (\sigma_o^{\text{res}})^2}. \quad (8.5)$$

2260 8.3 MCS implementation using the maximum likelihood method

2261 This section explains in detail how the phenomenon of multiple Coulomb scattering is used
 2262 to determine the momentum of a muon track reconstructed in a LArTPC. In general, the

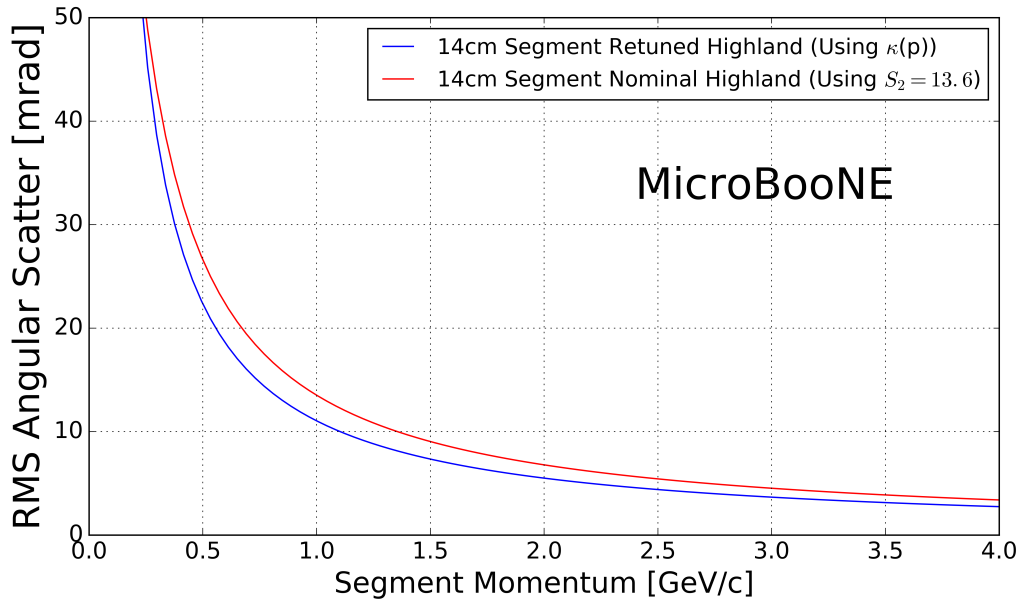


Figure 8.4: The Highland scattering RMS σ_o^{HL} for 14 cm segment lengths and 0 detector-inherent angular resolution as a function of true momentum before and after tuning. In red is shown equation 8.3 (the nominal Highland formula using $S_2 = 13.6$ MeV) and in blue is the retuned Highland formula (replacing S_2 with $\kappa(p)$).

2263 approach is as follows:

- 2264 1. The three-dimensional track is divided into segments of configurable length.
- 2265 2. The scattering angles between consecutive segments are measured.
- 2266 3. Those angles combined with the modified, tuned Highland formula (equation 8.5) are
2267 used to build a likelihood that the particle has a specific momentum, taking into
2268 account energy loss in upstream segments of the track.
- 2269 4. The momentum corresponding to the maximum of the likelihood is chosen to be the
2270 MCS-computed momentum.

2271 Each of these steps is discussed in detail in the following subsections.

2272

2273 **8.3.1 Track segmentation and scattering angle computation**

2274 Track segmentation refers to the subdivision of three-dimensional reconstructed trajectory
 2275 points of a reconstructed track into portions of definite length. In this analysis, the tracks
 2276 are automatically reconstructed by the “pandoraNuPMA” projection matching algorithm
 2277 [52]. The algorithm constructs the three-dimensional trajectory points by combining two-
 2278 dimensional hits reconstructed from signals on the different wire planes along with timing
 2279 information from the photomultiplier tubes. The segmentation process begins at the start
 2280 of the track, and iterates through the trajectory points in order, defining segment start and
 2281 stop points based on the straight-line distance between them. There is no overlap between
 2282 segments. Given the subset of the three-dimensional trajectory points that corresponds
 2283 to one segment of the track, a three-dimensional linear fit is applied to the data points,
 2284 weighting all trajectory points equally in the fit. In this analysis, a segment length of 14 cm
 2285 is used, which is a tunable parameter that has been chosen as described in the derivation
 2286 of $\kappa(p)$ (equation 8.4).

2287

2288 With the segments defined, the scattering angles between the linear fits from adjacent
 2289 segments are computed. A coordinate transformation is performed such that the z' direction
 2290 is oriented along the direction of the linear fit to the first of the segment pair. The x' and
 2291 y' coordinates are chosen such that all of x' , y' , and z' are mutually orthogonal and right-
 2292 handed, as shown in figure 8.2. The scattering angles with respect to the x' direction and
 2293 the y' direction are computed as input to the MCS algorithm. Only the scattering angle
 2294 with respect to the x' direction is drawn in figure 8.2.

2295 **8.3.2 Maximum likelihood theory**

2296 The normal probability distribution for a scattering angle in either the x' or y' direction,
 2297 $\Delta\theta$, with an expected Gaussian uncertainty σ_o and mean of zero is given by

$$f_X(\Delta\theta) = (2\pi\sigma_o^2)^{-\frac{1}{2}} \exp\left[-\frac{1}{2}\left(\frac{\Delta\theta}{\sigma_o}\right)^2\right]. \quad (8.6)$$

2298 Here, σ_o is the RMS angular deflection computed by the modified, tuned Highland for-
 2299 mula (equation 8.5), which is a function of the momentum and the length of that segment.

2300 Since energy is lost between segments along the track, σ_o increases for each angular measurement along the track. We therefore replace σ_o with $\sigma_{o,j}$, where j is an index representative
2301 of the segment.

2303

2304 To obtain the likelihood, we take the product of $f_X(\Delta\theta_j)$ over all n of the $\Delta\theta_j$ segment-
2305 to-segment scatters along the track. This product can be written as

$$L(\sigma_{o,1}, \dots, \sigma_{o,n}; \Delta\theta_1, \dots, \Delta\theta_n) = (2\pi)^{-\frac{n}{2}} \times \prod_{j=1}^n (\sigma_{o,j})^{-1} \times \exp \left[-\frac{1}{2} \sum_{j=1}^n \left(\frac{\Delta\theta_j}{\sigma_{o,j}} \right)^2 \right]. \quad (8.7)$$

2306 Rather than maximizing the likelihood it is more computationally convenient to instead
2307 minimize the negative log likelihood. Inverting the sign and taking $\ln(L)$ gives an expression
2308 that is related to a χ^2 variable:

$$-l(\mu_o; \sigma_{o,1}, \dots, \sigma_{o,n}; \Delta\theta_1, \dots, \Delta\theta_n) = -\ln(L) = \frac{n}{2} \ln(2\pi) + \sum_{j=1}^n \ln(\sigma_{o,j}) + \frac{1}{2} \sum_{j=1}^n \left(\frac{\Delta\theta_j}{\sigma_{o,j}} \right)^2 \quad (8.8)$$

2309 8.3.3 Maximum likelihood implementation

2310 Given a set of angular deflections in the x' and y' directions for each segment as described
2311 in section 8.3.1 a scan is done over the postulated initial energy, E_t , in steps of 1 MeV up
2312 to 7.5 GeV. The step with the smallest negative log likelihood (equation 8.8) is chosen as
2313 the MCS energy. Equation 8.8 includes a $\sigma_{o,j}$ term that changes for consecutive segments
2314 because their associated energy is decreasing. The energy of the j th segment is related to
2315 E_t by

$$E_j = E_t - \Delta E_j, \quad (8.9)$$

2316 where ΔE_j is the energy loss upstream of this segment, computed by integrating the muon
2317 stopping power curve given by the Bethe-Bloch equation described by the Particle Data
2318 Group (PDG) [53] along the length of track upstream of this segment. Equation 8.9 in-
2319 troduces a minimum allowable track energy determined by the length of the track, as E_j
2320 must remain positive. This value of segment energy is converted to a momentum p with
2321 the relativistic energy-momentum relation assuming the muon mass, and is then used to
2322 predict the RMS angular scatter for that segment (σ_o) by way of equation 8.5.

2323 8.4 Range-based energy validation from simulation

2324 In order to quantify the performance of the MCS energy estimation method on fully con-
2325 tained muons in data, an independent determination of energy is needed. Range-based
2326 energy, E_{range} is used here because the true energy E_{true} will not be known in analyzing
2327 detector data. The stopping power of muons in liquid argon is well described by the con-
2328 tinuous slowing-down approximation (CSDA) by the particle data group, and agrees with
2329 data at the sub-percent level [35] [36] [54]. By using a linear interpolation between points
2330 in the stopping power table of ref. [36], the length of a track can be used to reconstruct
2331 the muon's total energy with good accuracy. A simulated sample of fully contained BNB
2332 neutrino-induced muons longer than one meter is used to quantify the bias and resolution
2333 for the range-based energy estimation technique. The range is defined as the straight-line
2334 distance between the true starting point and true stopping point of a muon, even though
2335 the trajectories are not perfectly straight lines. The bias and resolution are computed in
2336 bins of true total energy of the muons by fitting a Gaussian function to a distribution of
2337 the fractional energy difference $(E_{\text{Range}} - E_{\text{True}})/(E_{\text{True}})$ in each bin. The mean of each
2338 Gaussian yields the bias for that true energy bin, and the width indicates the resolution.
2339 Figure 8.5 shows the bias and resolution for the range-based energy reconstruction method.
2340 The bias is negligible and the resolution for this method of energy reconstruction increases
2341 slightly with true muon energy but remains on the order of (2-4)%. This result demon-
2342 strates that range-based energy (and therefore range-based momentum) is a good estimator
2343 of the true energy (momentum) of a reconstructed contained muon track in data, assuming
2344 that the track is well reconstructed in terms of length.

2345 8.5 MCS performance on beam neutrino-induced muons in 2346 MicroBooNE data

2347 8.5.1 Input sample

2348 This part of the analysis is based on triggered neutrino interaction events in MicroBooNE
2349 corresponding to $\approx 5 \times 10^{19}$ protons on target, which is a small subset (<10%) of the

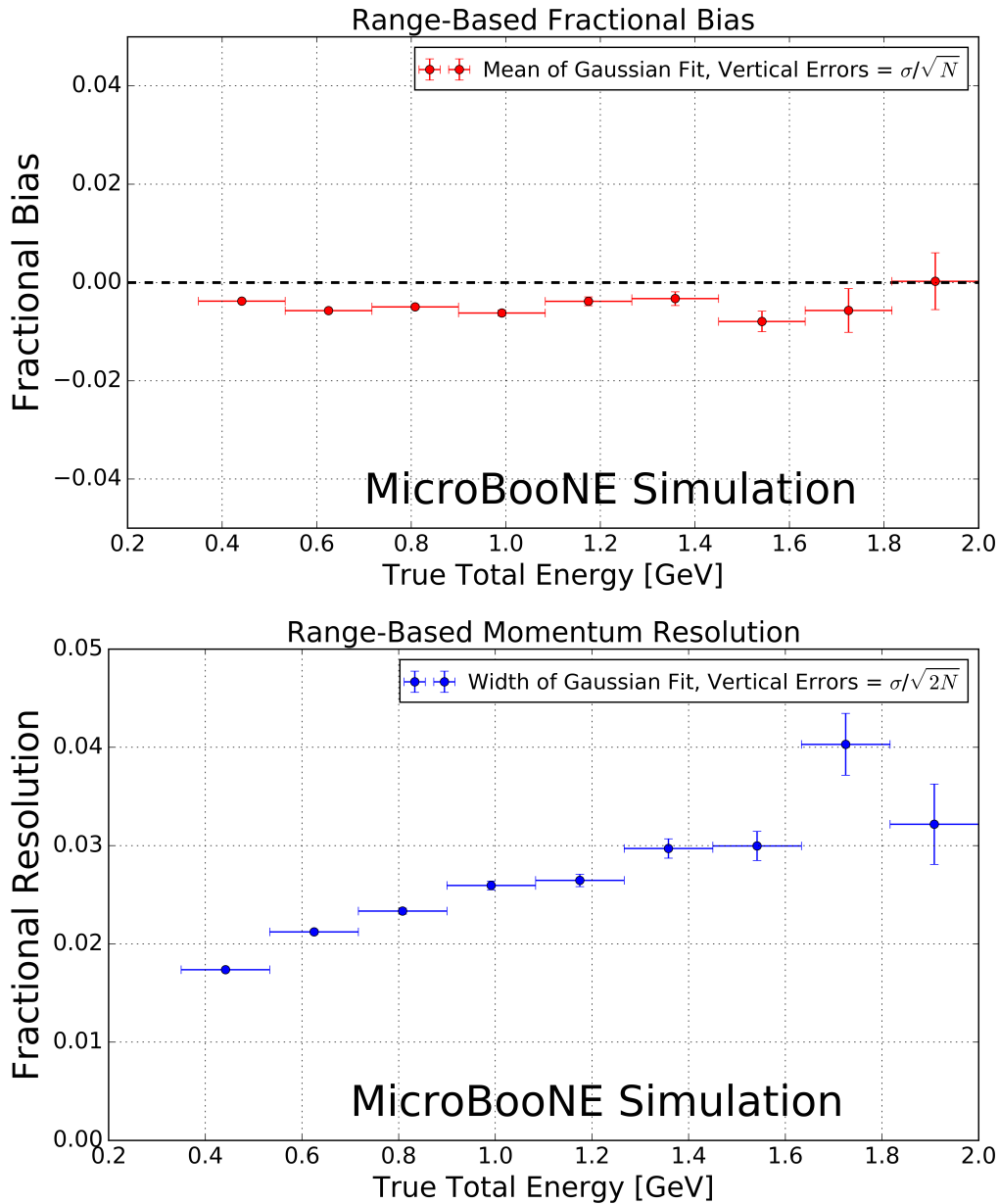


Figure 8.5: Range-based energy fractional bias (a) and resolution (b) from a sample of simulated fully contained BNB neutrino-induced muons using true starting and stopping positions of the track. The bias is less than 1% and the resolution is below $\approx 4\%$.

nominal protons on target scheduled to be delivered to the detector. These events are run through a fully automated reconstruction chain that produces reconstructed objects including three-dimensional neutrino interaction points (vertices), three-dimensional tracks (as described in section 8.3.1) for each outgoing secondary particle from the interaction, and PMT-reconstructed optical flashes from the interaction scintillation light. The fiducial volume used in this analysis is defined in section 8.1.

8.5.2 Event selection

The following selection criteria are placed on the reconstructed objects to select ν_μ charged-current interactions in which a candidate muon track exiting the interaction vertex is fully contained within the fiducial volume:

1. The event must have at least one bright optical flash, reconstructed from PMT timing signals, in coincidence with the expected BNB-neutrino arrival time.
2. Two or more reconstructed tracks must originate from the same reconstructed vertex within the fiducial volume.
3. The z coordinate of the optical flash, as determined by the pulse height and timing of signals in the 32 PMTs, must be within 70 cm of any point on the z projection of the candidate muon track.
4. For events with exactly two tracks originating from the vertex, additional calorimetric criteria are applied to mitigate backgrounds from cosmic muons that arrive in time with the passage of the beam, then stop and decay to an electron that is reconstructed as a track.
5. The longest track originating from the vertex is assumed to be a muon, and it must be fully contained within the fiducial volume.
6. The length of the longest track must be >1 m in order to have sufficient sampling points in the MCS likelihood to obtain a reasonable estimate of momentum.

These selection criteria are chosen to select a sample of tracks with high purity. In this sample of MicroBooNE data, 598 events (tracks) remain after all selections. The low

statistics in this sample is due to the size of the input sample and the low efficiency associated with the applied high-purity selection, described in section 8.5.1. Each of these events (tracks) was scanned by hand with a 2D interactive event display showing the raw wire signals of the interaction from each wire plane, with the 2D projection of the reconstructed muon track and vertex overlaid. The scanning was done to ensure the track is well reconstructed with start point close to the reconstructed vertex and end point close to the end of the visible wire-signal track in all three planes. During the scanning, obvious mis-identification topologies were removed. An example of such a topology is a stopping cosmic-ray muon decaying into an electron. After rejecting events (tracks) based on hand scanning, 396 tracks remain for analysis.

8.5.3 Validation of the Highland formula

The Highland formula indicates that distributions of angular deviations of the track, segment by segment, in both the x' and y' directions divided by the width predicted from the Highland equation σ_o^{RMS} (equation 8.5) should be Gaussian with a width of unity. In order to calculate the momentum p in the Highland equation, p for each segment is computed with equation 8.9, where E_t comes from the converged MCS-computed momentum of the track. For each consecutive pair of segments in this sample of 396 tracks, the angular scatter divided by the Highland expected RMS (including detector resolution term, σ_o^{res}) is an entry in the area-normalized distribution shown in figure 8.6. These 396 tracks have on average 12 segments each, therefore this histogram has approximately $396 \times 12 \times 2 = 9504$ entries. The additional factor of 2 comes from angular scatters both in the x' and y' directions. The distribution has an RMS of unity, thus validating the MCS technique used in this analysis.

8.5.4 MCS momentum validation

MCS momentum versus range-based momentum for this sample of 396 tracks is shown in figure 8.7. The fractional bias and resolution as a function of range-based momentum for this sample is shown in figure 8.8. In order to compute this bias and resolution, distributions of fractional inverse momentum difference $(p_{\text{MCS}}^{-1} - p_{\text{Range}}^{-1})/(p_{\text{Range}}^{-1})$ in bins of range-based momentum p_{Range} are fit to Gaussian functions, where the mean of the fit determines the

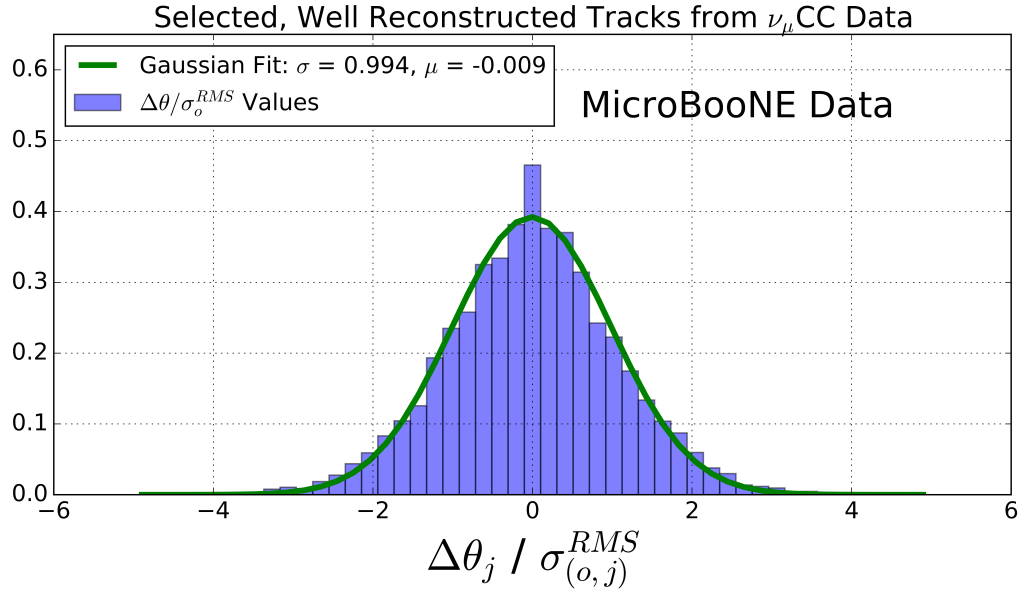


Figure 8.6: Segment-to-segment measured angular scatters in both the x' and y' directions divided by the width σ_o^{RMS} predicted by the Highland formula (equation 8.1) for the automatically selected beam neutrino-induced fully contained muon sample in MicroBooNE data after hand scanning to remove poorly reconstructed tracks and obvious mis-identification topologies.

2405 bias while the width of the fit determines the resolution for that bin. Inverse momentum is
 2406 used here because the binned distributions are more Gaussian since the Highland formula
 2407 measures inverse momentum in terms of track angles that have reasonably Gaussian errors.
 2408 Simply using the mean and RMS of the binned distributions yields similar results. Also
 2409 shown in this figure are the bias and resolutions for a simulated sample consisting of a full
 2410 BNB simulation with CORSIKA-generated [55] cosmic overlays passed through an identical
 2411 reconstruction and event selection chain. Rather than hand scanning this sample, true
 2412 simulation information is used by requiring the longest reconstructed track to be matched
 2413 well to the true starting and stopping point of the ν_μ CC muon. This removes any mis-
 2414 identifications or interference from the simulated cosmics.

2415 Figure 8.8 indicates a bias in the MCS momentum calculation on the order of a few per-
 2416 cent, with a resolution that decreases from about 10% for contained reconstructed tracks

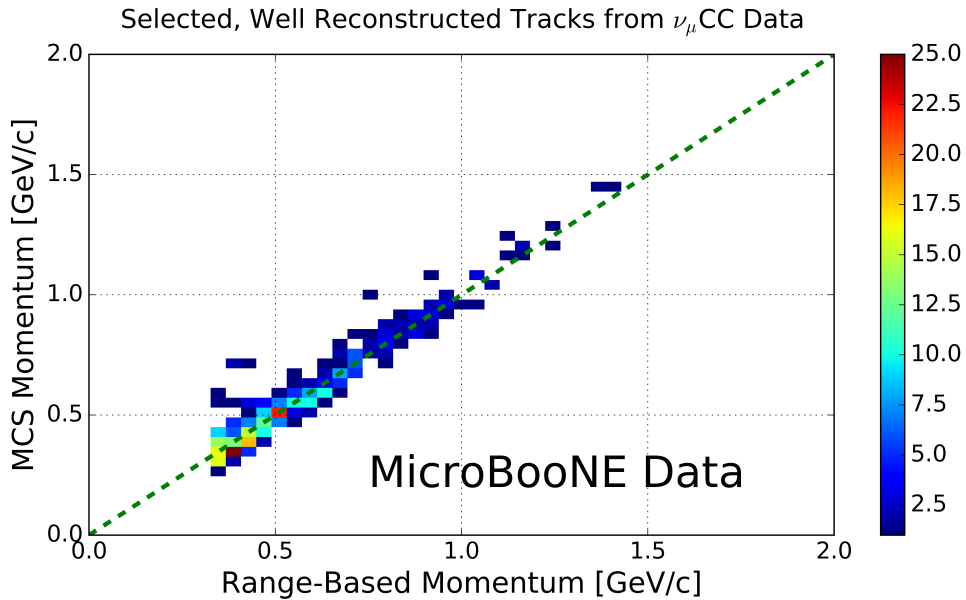


Figure 8.7: MCS-computed momentum versus range momentum for the automatically selected beam neutrino-induced fully contained muon sample in MicroBooNE data after hand scanning to remove poorly reconstructed tracks and obvious mis-identification topologies. The color (z) scale indicates number of tracks.

2417 in data and simulation with range momentum around 0.45 GeV/c (which corresponds to a
 2418 length of about 1.5 m) to below 5% for contained reconstructed tracks in data and simula-
 2419 tion with range momentum about 1.15 GeV/c (which corresponds to a length of about 4.6
 2420 meters). Resolution improving with length of track is expected; the longer the track, the
 2421 more angular scattering measurements can be made to improve the likelihood. In general
 2422 the bias and resolutions agree between data and simulation within uncertainty.

2423

2424 8.5.5 Impact of Highland formula tuning

2425 In order to examine the impact of the Highland formula tuning described in section 8.2.1,
 2426 the fractional bias and resolution on the simulated sample of contained muons described in
 2427 section 8.5.4 both with the nominal Highland formula (equation 8.2) and with the retuned
 2428 Highland formula (equation 8.5) are shown in figure 8.9. Tuning the Highland formula

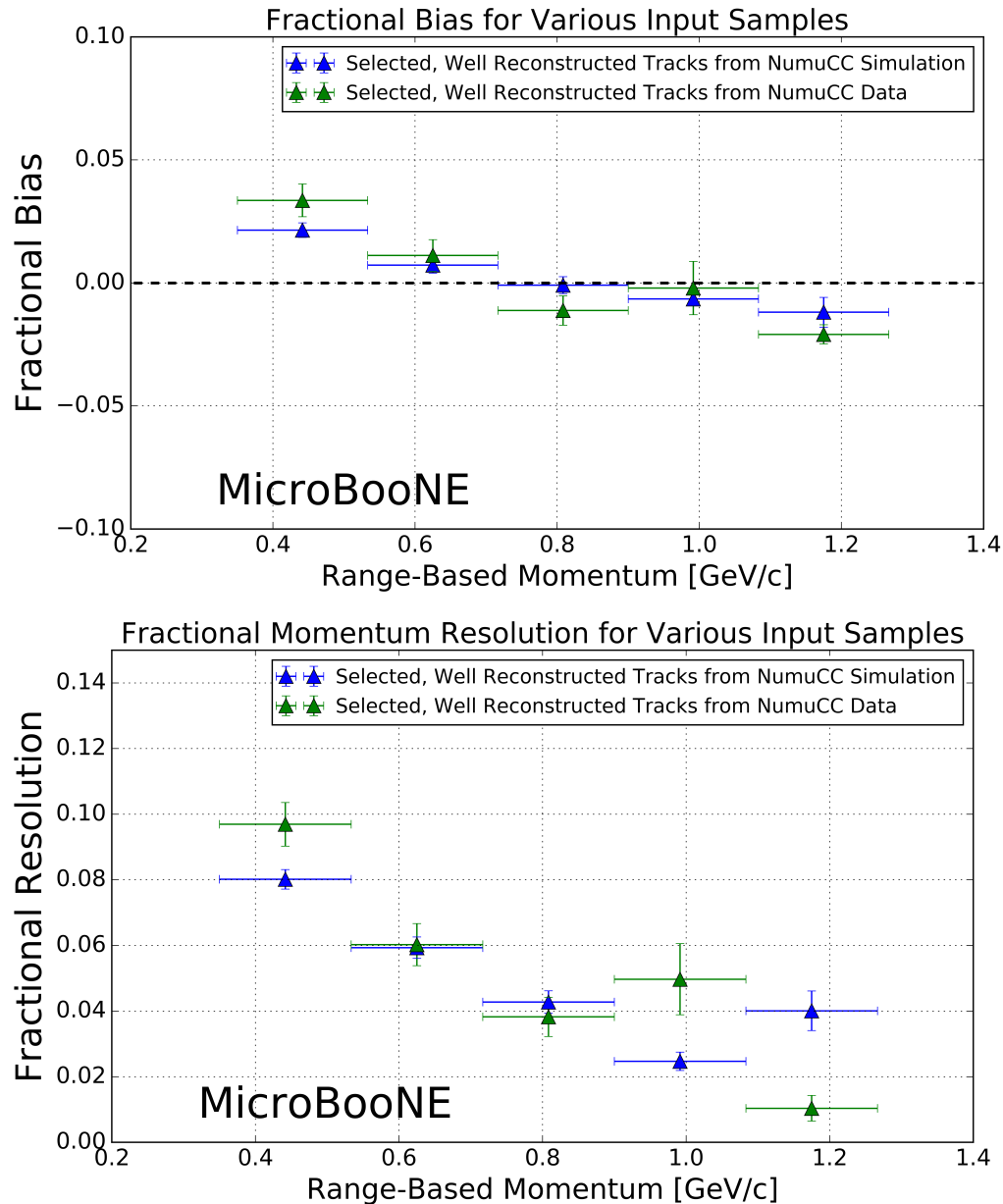


Figure 8.8: Inverse momentum difference (as defined in the text) fractional bias (top) and resolution (bottom) for automatically selected contained ν_μ CC-induced muons from full simulated BNB events with cosmic overlay where the track matches with the true muon track (blue), and automatically selected and hand-scanned (see text) contained ν_μ CC-induced muons from MicroBooNE data (green).

2429 improves the magnitude of the fractional bias to below 2%, and improves the fractional
2430 resolution by (2-3)%, with the most improvement at the lowest momenta.

2431 8.6 MCS performance on exiting muons in MicroBooNE simulation

2432

2433 In this section we quantify the MCS algorithm performance on a sample of well recon-
2434 structed exiting muon tracks in simulated BNB ν_μ CC interactions within the MicroBooNE
2435 detector. The tracks are automatically reconstructed by the same “pandoraNuPMA” al-
2436 gorithm described in section 8.3.1, and all tracks have a length of at least 1 m within the
2437 TPC. This simulation does not include space-charge effects. The relationship between the
2438 MCS and the true momenta at the beginning of the track as given by simulation for this
2439 sample of 28,000 exiting muon tracks is shown in figure 8.10.

2440

2441 The distribution of $(p_{\text{MCS}}^{-1} - p_{\text{true}}^{-1})/(p_{\text{true}}^{-1})$ is shown for four representative bins of true
2442 momentum in figure 8.11, along with the Gaussian fit to each distribution. Low-momentum
2443 tails where the MCS momentum is underestimated due to poor track reconstruction lie
2444 outside the fitted Gaussian function.

2445

2446 The fractional bias and resolution as a function of true momentum are shown in figure
2447 8.12. The bias is below 4% for all momenta, and the resolution is $\approx 14\%$ in the relevant
2448 momentum region for BNB ν_μ CC muons (below 2 GeV/c). The resolution worsens for
2449 muon momenta above this region because the angular scatters begin to be comparable with
2450 the detector resolution term of 3 mrad. The resolution improves for longer lengths of track
2451 contained, with 10% resolution for muons with $p < 2$ GeV/c with more than 3.5 meters
2452 contained. The mean length of track contained for muons in this analysis is 212 cm.

2453

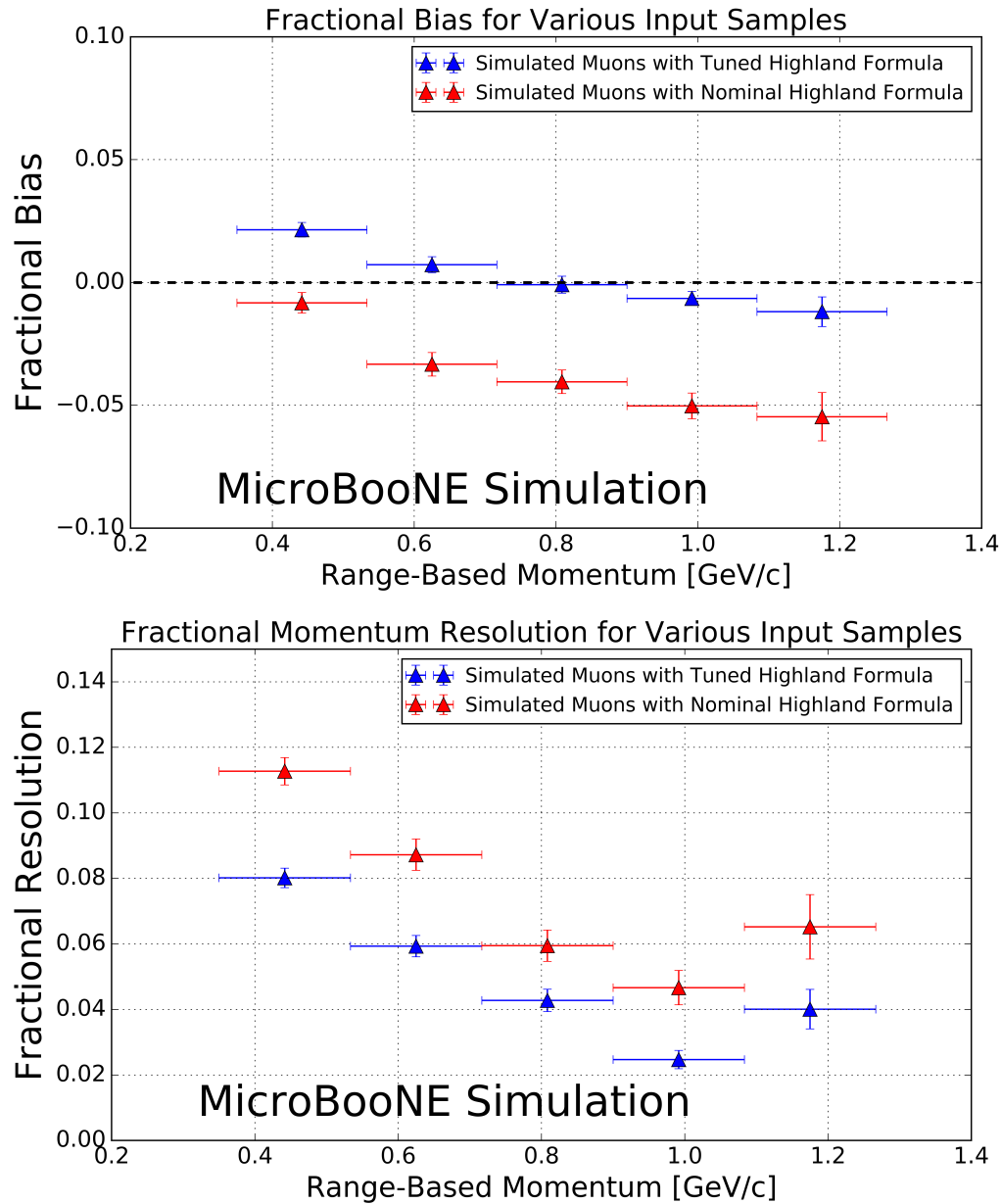


Figure 8.9: Inverse momentum difference (as defined in the text) fractional bias (top) and resolution (bottom) for automatically selected contained ν_μ CC-induced muons from full simulated BNB events with cosmic overlay where the track matches with the true muon track both using the nominal Highland formula (equation 8.2) (red) and the retuned Highland formula (equation 8.5) (blue).

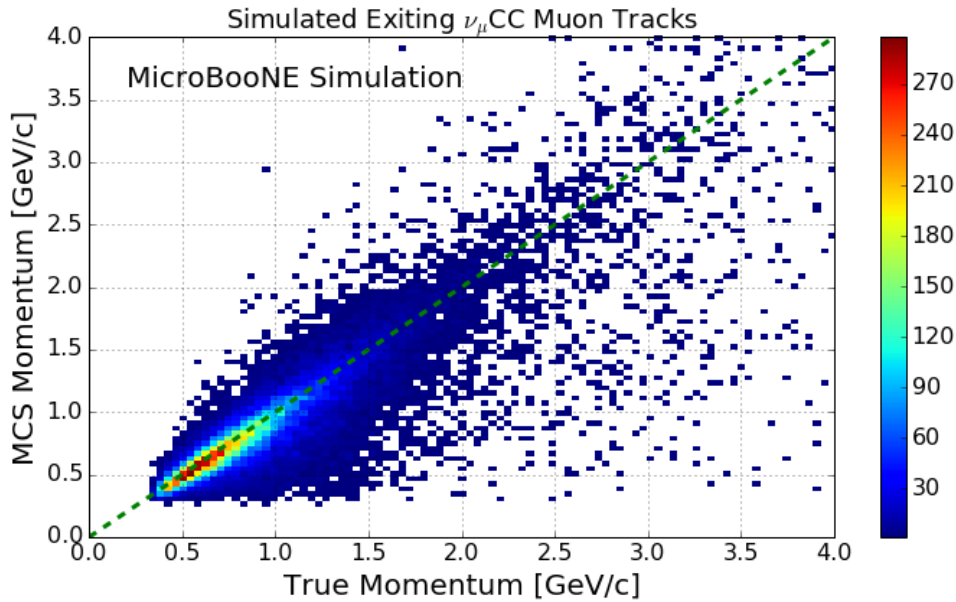


Figure 8.10: MCS-computed momentum versus true momentum for the sample of simulated exiting BNB ν_μ CC muons in MicroBooNE with at least one meter of track contained within the TPC. The color (z) scale indicates number of tracks.

2454 8.7 Conclusions

2455 We have described a multiple Coulomb scattering maximum likelihood method for esti-
2456 mating the momentum of a three dimensional reconstructed track in a LArTPC and have
2457 provided motivation for development of such a technique. Using simulation, we have shown
2458 that the standard Highland formula should be re-tuned specifically for scattering in liquid ar-
2459 gon. After validating range-based momentum-determination techniques with MicroBooNE
2460 simulation, we have demonstrated the accuracy and precision of the MCS-based momen-
2461 tum reconstruction in MicroBooNE data by comparing its performance to the range-based
2462 method. For 398 fully-contained BNB ν_μ CC-induced muons, the MCS method exhibits
2463 a fractional bias below 3% and a momentum resolution below 10%, agreeing with simu-
2464 lation predictions. Using simulation of a separate sample of uncontained muon tracks in
2465 MicroBooNE with at least one meter contained in the active volume, the MCS-based re-
2466 construction is shown to produce a fractional bias below 4% and a momentum resolution

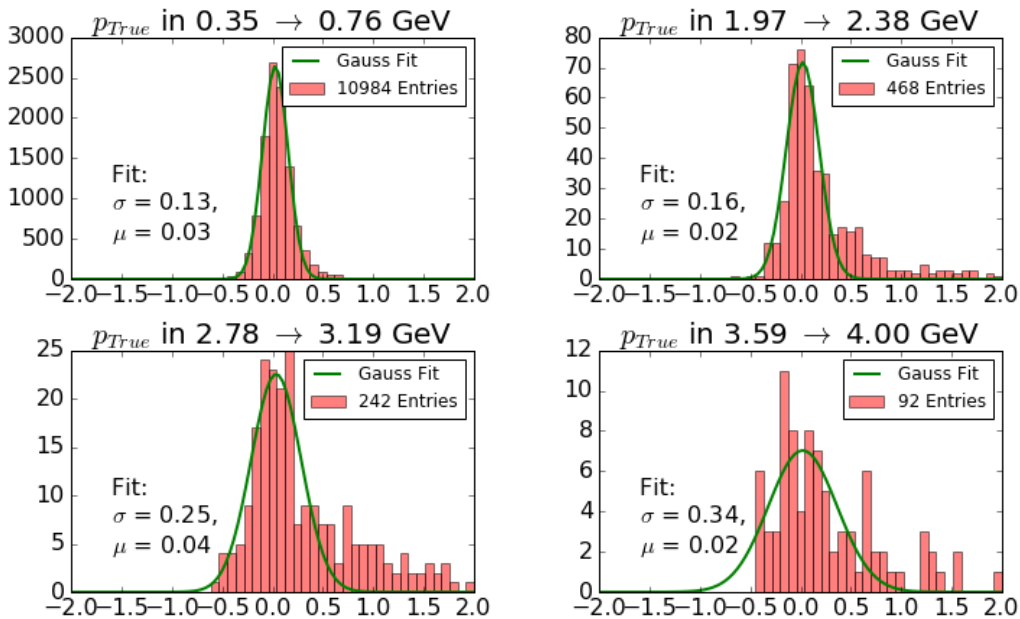


Figure 8.11: Fractional momentum difference for a few representative bins of true momentum for a sample of simulated exiting muon tracks. The y-axis is number of tracks, and the x-axis is $(p_{\text{MCS}}^{-1} - p_{\text{true}}^{-1})/(p_{\text{true}}^{-1})$.

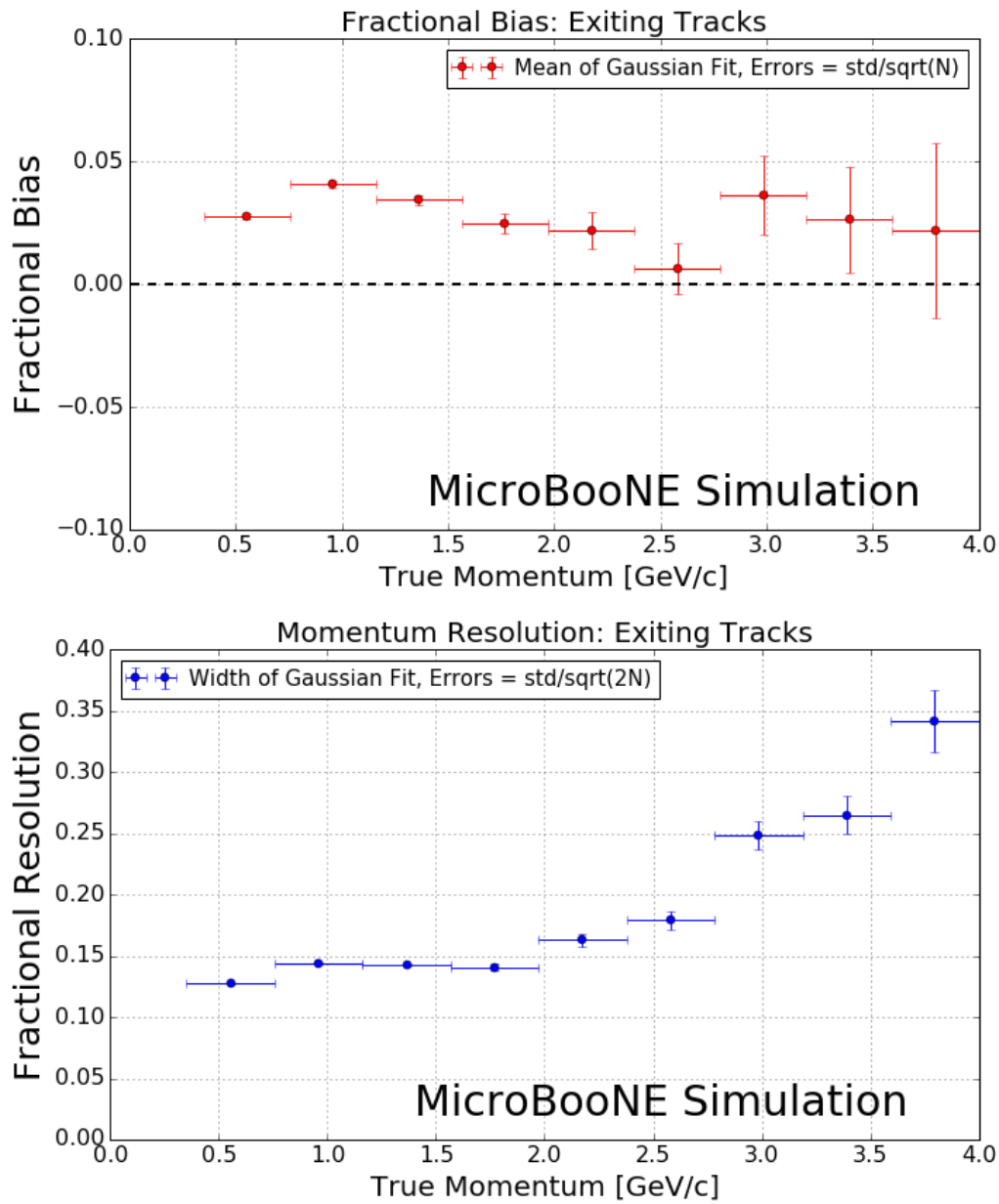


Figure 8.12: MCS momentum fractional bias (top) and resolution (bottom) as a function of true momentum from a sample of exiting reconstructed muon tracks.

2467 of better than 15% for muons in the relevant BNB energy region of below 2 GeV.

2468 8.8 Acknowledgments

2469 This material is based upon work supported by the following: the U.S. Department of
2470 Energy, Office of Science, Offices of High Energy Physics and Nuclear Physics; the U.S. Na-
2471 tional Science Foundation; the Swiss National Science Foundation; the Science and Technol-
2472 ogy Facilities Council of the United Kingdom; and The Royal Society (United Kingdom).
2473 Additional support for the laser calibration system and cosmic ray tagger was provided
2474 by the Albert Einstein Center for Fundamental Physics. Fermilab is operated by Fermi
2475 Research Alliance, LLC under Contract No. DE-AC02-07CH11359 with the United States
2476 Department of Energy.

²⁴⁷⁷ Bibliography

- 2478 [1] J Chadwick. Intensittsverteilung im magnetischen Spectrum der β -Strahlen von radium
2479 B + C. *Verhandl. Dtsc. Phys. Ges.*, 16:383, 1914.
- 2480 [2] W. Pauli. Open letter to the group of radioactive people at the gauverein meeting in
2481 tubingen. 1930.
- 2482 [3] S. Schael et al. Precision electroweak measurements on the Z resonance. *Phys. Rept.*,
2483 427:257–454, 2006.
- 2484 [4] Y. Fukuda et al. Evidence for oscillation of atmospheric neutrinos. *Phys. Rev. Lett.*,
2485 81:1562–1567, 1998.
- 2486 [5] Q. R. Ahmad and others. Measurement of the rate of $\nu_e + d \rightarrow p + p + e^-$ interactions
2487 produced by 8b solar neutrinos at the sudbury neutrino observatory. *Phys. Rev. Lett.*,
2488 87:071301, Jul 2001.
- 2489 [6] X. Qian and P. Vogel. Neutrino Mass Hierarchy. *Prog. Part. Nucl. Phys.*, 83:1–30,
2490 2015.
- 2491 [7] S. Abe et al. Precision Measurement of Neutrino Oscillation Parameters with Kam-
2492 LAND. *Phys. Rev. Lett.*, 100:221803, 2008.
- 2493 [8] A. Aguilar-Arevalo et al. Evidence for neutrino oscillations from the observation of anti-
2494 neutrino(electron) appearance in a anti-neutrino(muon) beam. *Phys. Rev.*, D64:112007,
2495 2001.
- 2496 [9] G. Cheng. Precision search for muon antineutrino disappearance oscillations using a
2497 dual baseline technique. 2013.

- 2498 [10] R. Acciarri et al. Design and Construction of the MicroBooNE Detector. *Submitted*
 2499 *to: JINST*, 2016.
- 2500 [11] A. A. Aguilar-Arevalo et al. The Neutrino Flux prediction at MiniBooNE. *Phys. Rev.*,
 2501 D79:072002, 2009.
- 2502 [12] S. Agostinelli et al. GEANT4: A Simulation toolkit. *Nucl. Instrum. Meth.*, A506:250–
 2503 303, 2003.
- 2504 [13] M. G. Catanesi et al. Measurements of the production cross-section of positive pions
 2505 in the collision of 8.9 GeV/c protons on beryllium. *Eur. Phys. J.*, C52:29–53, 2007.
- 2506 [14] I. Chemakin et al. Centrality dependence of pi- production and stopping in p - A
 2507 collisions at 18-GeV/c. *Submitted to: Phys. Rev. Lett*, 1999.
- 2508 [15] C. Mariani, G. Cheng, J. M. Conrad, and M. H. Shaevitz. Improved Parameterization
 2509 of K^+ Production in p-Be Collisions at Low Energy Using Feynman Scaling. *Phys.*
 2510 *Rev.*, D84:114021, 2011.
- 2511 [16] G. Cheng et al. Measurement of K^+ production cross section by 8 GeV protons using
 2512 high energy neutrino interactions in the SciBooNE detector. *Phys. Rev.*, D84:012009,
 2513 2011.
- 2514 [17] A. A. Aguilar-Arevalo et al. The MiniBooNE Detector. *Nucl. Instrum. Meth.*, A599:28–
 2515 46, 2009.
- 2516 [18] G. Karagiorgi. Searches for new physics at miniboone: Sterile neutrinos and mixing
 2517 freedom. 2010.
- 2518 [19] A. A. Aguilar-Arevalo et al. First Measurement of the Muon Neutrino Charged Current
 2519 Quasielastic Double Differential Cross Section. *Phys. Rev.*, D81:092005, 2010.
- 2520 [20] A. A. Aguilar-Arevalo et al. A Search for electron neutrino appearance at the $\Delta m^2 \sim$
 2521 1eV^2 scale. *Phys. Rev. Lett.*, 98:231801, 2007.
- 2522 [21] A. A. Aguilar-Arevalo et al. Unexplained Excess of Electron-Like Events From a 1-GeV
 2523 Neutrino Beam. *Phys. Rev. Lett.*, 102:101802, 2009.

- 2524 [22] Thomas Schwetz. The LSND puzzle in the light of MiniBooNE results. In *Proceedings,*
2525 *43rd Rencontres de Moriond on Electroweak Interactions and Unified Theories: La*
2526 *Thuile, Italy, March 1-8, 2008.* 2008.
- 2527 [23] H. Chen et al. A Proposal for a New Experiment Using the Booster and NuMI Neutrino
2528 Beamlines: MicroBooNE.
- 2529 [24] The microboone technical design report. 2012.
- 2530 [25] Costas Andreopoulos, Christopher Barry, Steve Dytman, Hugh Gallagher, Tomasz
2531 Golan, Robert Hatcher, Gabriel Perdue, and Julia Yarba. The GENIE Neutrino Monte
2532 Carlo Generator: Physics and User Manual. 2015.
- 2533 [26] D. Casper. The Nuance neutrino physics simulation, and the future. *Nucl. Phys. Proc.*
2534 *Suppl.*, 112:161–170, 2002. [,161(2002)].
- 2535 [27] D. Heck, G. Schatz, T. Thouw, J. Knapp, and J. N. Capdevielle. CORSIKA: A Monte
2536 Carlo code to simulate extensive air showers. 1998.
- 2537 [28] Wouter Verkerke and David P. Kirkby. The RooFit toolkit for data modeling. *eConf*,
2538 C0303241:MOLT007, 2003. [,186(2003)].
- 2539 [29] A. A. Aguilar-Arevalo et al. Unexplained Excess of Electron-Like Events From a 1-GeV
2540 Neutrino Beam (Data Release).
- 2541 [30] M. Antonello et al. A Proposal for a Three Detector Short-Baseline Neutrino Oscillation
2542 Program in the Fermilab Booster Neutrino Beam. 2015.
- 2543 [31] A. Ankowski et al. Energy reconstruction of electromagnetic showers from pi0 decays
2544 with the ICARUS T600 Liquid Argon TPC. *Acta Phys. Polon.*, B41:103–125, 2010.
- 2545 [32] J. R. Sanford and C. L. Wang. *BNL Internal Note No, 11299*, 1967.
- 2546 [33] J. S. Marshall and M. A. Thomson. The Pandora Software Development Kit for Pattern
2547 Recognition. *Eur. Phys. J.*, C75(9):439, 2015.
- 2548 [34] R. Acciarri *et al.* Study of Space Charge Effects in MicroBooNE.

- 2549 [35] N. V. Mokhov D. E. Groom and S. Striganov. Muon Stopping Power and Range Tables:
 2550 10 MeV - 100 TeV, Table 5.
- 2551 [36] Muons in liquid argon (ar) table 289.
- 2552 [37] A. A. Aguilar-Arevalo *et al.* Improved Search for $\bar{\nu}_\mu \rightarrow \bar{\nu}_e$ Oscillations in the Mini-
 2553 BooNE Experiment. *Phys. Rev. Lett.* **110**, 161801 (2013).
- 2554 [38] C. Adams *et al.* LAr1-ND: Testing Neutrino Anomalies with Multiple LArTPC De-
 2555 tectors at Fermilab.
- 2556 [39] F. Arneodo *et al.* The ICARUS experiment: A Second generation proton decay exper-
 2557 iment and neutrino observatory at the Gran Sasso Laboratory.
- 2558 [40] R. Acciarri *et al.* Long-Baseline Neutrino Facility (LBNF) and Deep Underground
 2559 Neutrino Experiment (DUNE) : Volume 1: The LBNF and DUNE Projects.
- 2560 [41] R. Acciarri *et al.* Design and Construction of the MicroBooNE Detector.
- 2561 [42] A. A. Aguilar-Arevalo *et al.* The Neutrino Flux prediction at MiniBooNE. *Phys. Rev.*
 2562 *D* **79**, 072002, 2009.
- 2563 [43] V. L. Highland. Some Practical Remarks on Multiple Scattering. *Nucl. Instrum.*
 2564 *Methods* **129**, 1975.
- 2565 [44] G. R. Lynch and O. I. Dahl. *Nucl. Instrum. Methods Section B (Beam Interactions*
 2566 *with Materials and Atoms)* **B58**, **6**, 1991.
- 2567 [45] K. Kodama *et al.* Observation of tau neutrino interactions. *Phys. Lett. B* **504**, 218,
 2568 2001.
- 2569 [46] N. Agafonova *et al.* Momentum measurement by the Multiple Coulomb Scattering
 2570 method in the OPERA lead emulsion target. *New J. Phys.* **14**, 013026, 2012.
- 2571 [47] G. Giacomelli. Neutrino physics and astrophysics with the MACRO experiment at the
 2572 Gran Sasso lab. *Braz. J. Phys.* **33**, 211, 2003.

- 2573 [48] A. Ankowski *et al.* Measurement of through-going particle momentum by means of
2574 multiple scattering with the ICARUS T600 TPC. *Eur. Phys. J. C* **48**, 667, 2006.
- 2575 [49] M. Antonello *et al.* Muon momentum measurement in ICARUS-T600 LAr-TPC via
2576 multiple scattering in few-GeV range.
- 2577 [50] S. Agostinelli et al. *Nucl. Instrum. Methods Phys. Res.* **A506250-303**, 2003.
- 2578 [51] F. Cavanna *et al.* LArIAT: Liquid Argon In A Testbeam.
- 2579 [52] J. S. Marshall and M. A. Thomson. The Pandora Software Development Kit for Pattern
2580 Recognition. *Eur. Phys. J. C* **75**, no. 9, 439, 2015.
- 2581 [53] S.R. Klein H. Bichsel, D. E. Groom. Passage of Particles Through Matter pdg chapter
2582 27, figure 27.1.
- 2583 [54] Stopping Powers and Ranges for Protons and Alpha Particles. *ICRU Report No. 49*,
2584 1993.
- 2585 [55] *et al.* D. Heck, J. Knapp. CORSIKA: A Monte Carlo Code to Simulate Extensive Air
2586 Showers. *Forschungszentrum Karlsruhe Report FZKA 6019*, 1998.